An Experimental Investigation to Assess the Feasibility of Imaging Medical Radioisotopes with the ProSPECTus Compton Camera

Thesis submitted in accordance with the requirements of the University of Liverpool for the degree of Doctor in Philosophy

by

Amina Patel

Oliver Lodge Laboratory

September 2016

Acknowledgments

I would like to take this opportunity to thank everyone who has supported me throughout my PhD, I will do my best to express myself without using any emoticons.

A great big thank you goes to my supervisor Dr Laura Harkness-Brennan for giving me the encouragement, guidance and support needed to do and complete this work. I would also like to thank Dr Helen Boston and Dr Andy Boston for their supervision and for giving me the opportunity of working on the ProSPECTus project. I am also grateful for the help I received from Professor Paul Nolan with my timing measurements and his suggestions for the final draft of my thesis. A special thank you goes to Dr Dan Judson for all the help in the lab, reading my chapters and for letting me use his office white-board a lot. I have enjoyed working as part of the Nuclear medical imaging group and in particular would like to thank Sam, Jamie, Jon, Anthony, Tom, Jon, Carl, Kevin and Craig for all their help and support throughout my project.

I have enjoyed working and living in Liverpool so would like to thank the people who have made it a great last four years:

- **Will**: Thank you for being brave enough to sit next to me in the office whilst I wrote this thesis. I have valued all your support, patience, kindness and encouragement over the last few years. Thank you also for the random snippets of life advice "Sometimes take the stairs not just the lift", for helping me eat my snacks and the many many many trips for coffee. I look forward to us finding the coffee shop that does the best 'flat white'.

- **Faye**: My office best friend, I can't thank you enough for all your support, friendship and hair advice. I have enjoyed all our gossip sessions, and evening plans consisting of eating waffles and ice-cream. Thank you for always lending me your student card, when I lost mine, which happened too many times.

- **Saleha**: My 'temporary' room-mate. I enjoyed all the times you turned up at my flat after 10 pm and made me go places I really didn't want to go, the spontaneous nights out were always the best. Thanks for always being up for shopping sprees, takeaways, shisha and random movie marathons, they helped me keep my sanity throughout.

Also thank you to my friends and family who have always been there, especially to Tahira, Muneerah, Karen, Reyhana, Helen, Nairi and Ashlea. Thank you for all the late night phone calls and check ups, and the visits to Liverpool for fun weekends.

Last but obviously not least, thank you to my mum, dad, Imran and grandparents for all their encouragement throughout my studies.

Abstract

An experimental investigation into the feasibility of imaging multiple medical radioisotopes with the ProSPECTus Compton camera is presented. The aim of the project is to develop a Compton imaging system configured with segmented solid state detectors, for the purpose of alleviating the limitations of conventional Single Photon Emission Computed Tomography (SPECT) systems. The ProSPECTus system consists of a Si(Li) and HPGe planar detector housed in a magnetic field compatible custom made cryostat. The investigation presented in this thesis has been undertaken with a prototype ProSPECTus system, which consists of Si(Li) and HPGe planar detectors housed in separate cryostats. Analysis of the results attained from investigations into the optimum coincidence window, noise thresholds and image reconstruction techniques as part of this thesis are to be used to inform future developments and measurements.

The work presented focuses on an investigation of simultaneous data acquisition with the medical radioisotopes ^{99m}Tc and ^{123}I, which emit gamma-rays with energies of 141 keV and 159 keV, respectively. The experimental methodology of defining parameters for timing and noise thresholds is described along with system performance in terms of image quality and efficiency. A custom designed phantom is used to build source complexity and to provide qualitative and quantitative assessment of the imaging capabilities of ProSPECTus using analytical and iterative reconstruction algorithms. It has been determined that a spatial resolution of 3 mm is achievable, using iterative reconstruction of data acquired from a ^{139}Ce point source of energy 166 keV. Quantitative analysis has revealed that an Edge Response is a good measure of determining the resolvability of extended source distributions.

It has been proved that the spectroscopic response enables ProSPECTus to image ^{99m}Tc and ^{123}I simultaneously. This would otherwise require complex peak deconvolution techniques in clinical SPECT systems. An improvement in efficiency of up to a factor of 2.5 over conventional SPECT systems is demonstrated, with suggestions for further improvements, indicating a factor of 23 is achievable with the next generation system. This would potentially reduce patient dose or increase patient throughput. Suggestions are presented for the iterative reconstruction algorithm to facilitate enhanced imaging with the next generation ProSPECTus system.

Contents

1 Introduction **1**

1.1 Nuclear Medicine 1

1.1.1 Single Photon Emission Computed Tomography 2

1.2 The ProSPECTus Project 3

1.3 Thesis Outline 4

2 The Fundamentals of Gamma Ray Spectroscopy **6**

2.1 Interaction of Gamma rays with Matter 6

2.1.1 Compton Scattering 7

2.1.2 Photoelectric Absorption 10

2.1.3 Pair Production 12

2.2 Interaction of Charge Carriers 12

2.2.1 Collisional Losses 13

2.3 Principles of Gamma ray Detectors 14

2.3.1 Scintillator Detectors 14

2.3.2 Semiconductors 16

2.3.3 Detector Performance 32

3 Principles of Gamma Ray Imaging **34**

3.1 Imaging In Nuclear Medicine 34

3.2 Principles of Single Photon Emission Computed Tomography . 35

3.2.1 The Fundamental Components of a Gamma Camera . 38

3.2.2 Limitations of Conventional SPECT Systems 46

3.3 Principles of Compton Imaging 46

3.3.1 Operation of a Compton camera 47

3.4 The Next Generation ProSPECTus Compton Camera 48
3.4.1 Advantages of the Compton camera configuration for SPECT systems 50
3.5 Inherent Detector Properties that Influence Image Quality . . 51
3.5.1 Energy Resolution 51
3.5.2 Doppler Broadening 52
3.5.3 Position Resolution 52
3.5.4 Performance of a Compton Camera System 53

4 Optimisation of Experimental Set up and Parameters 56
4.1 The ProSPECTus System 57
4.1.1 Scatter Detector 58
4.1.2 Absorber 1 Detector 60
4.1.3 Absorber 2 Detector 62
4.2 Experimental Set Up for Imaging 63
4.2.1 Detector Geometric Details 63
4.2.2 Data Acquisition System 64
4.2.3 Energy Calibration 72
4.2.4 Data Collection and Processing 72
4.2.5 Noise Thresholds 74
4.2.6 System Timing Response 77
4.2.7 ProSPECTus Timing Resolution 84
4.2.8 Investigation of the Coincidence Window in the CAEN Digitiser Cards 86
4.2.9 Image Reconstruction 88

5 Imaging Results and Analysis 93
5.0.10 ^{139}Ce Point Source Analysis 94
5.0.11 ^{99m}Tc and ^{123}I 16.4 mm Diameter Vials 104
5.0.12 ^{99m}Tc, ^{123}I and ^{139}Ce 16.4 mm Diameter Vials 126
5.0.13 Phantom 133

6 Conclusions and Future Work 150
6.0.14 Conclusion 150

6.0.15 Future Work 153

Appendices **155**

A Detector Performance **156**

A.1 Energy Calibration 156

A.2 Energy Resolution 156

A.2.1 Timing Response 160

List of Figures

2.1 Graph displaying the probability of a gamma ray undergoing Compton scattering, photoelectric absorption and pair production as a function of gamma-ray energy ($E_{\gamma I} = hf$) and atomic number Z. The boundaries are shown for Ge (red line) and Si (blue line). The black lines represent the Z and E values where two neighboring effects are equally probable. Image reproduced from [9]. 8

2.2 Schematic illustration of the Compton scattering process. . . 8

2.3 Graphical representation of the Klein Nishina formula which predicts the scattering angle for gamma rays of particular energies. The diagram is in polar co-ordinates and depicts the gamma rays incident from the left that are Compton scattered into a solid angle θ. 10

2.4 Schematic illustration of the photoelectric absorption process. 11

2.5 Approximate variation of the photoelectric cross section with Z^n, for various values of $E_{\gamma I}$. Image reproduced from [11]. . . 11

2.6 Schematic illustration of a gamma ray interacting via the pair production process. 13

2.7 Schematic drawing of the main components of a scintillator detector. 15

2.8 Schematic drawing of a Face Centred Cubic (FCC) lattice structure. Si and Ge have this crystal configuration. 17

2.9 Examples of the Miller indices notation, which are used to describe planes in crystal lattice. 18

2.10 Schematic diagram of the band structure in a conductor, insulator and semiconductor 19
2.11 Energy band structures of indirect semiconductors: a) Ge b) Si and a direct semiconductor c) GaAs. The shaded regions represent the minimum of the conduction and energy bands aswell as the energy band gaps. Reproduced from [18]. 20
2.12 Plots reproduced from [19] of (a) Si hole drift velocity and (b) Si electron drift velocity. Plots are as function of Electric field for three different temperatures. It is shown that the drift velocity is saturated at $\sim 10^7$cm/s. 22
2.13 Schematic diagram of the band structure in n- and p-type semiconductors. 24
2.14 Schematic diagram of a p-n junction, demonstrating the build up of space charge at the boundary between the p- and n-type material, where the charges of the fixed dopant ions are shown in the depleion layer. 25
2.15 Schematic representation of a Ge planar detector. 26
2.16 Schematic drawing of the Si(Li) and HPGe planar detectors, detailing the reverse bias voltage and the relative charge carrier collection, at the AC and DC electrical contact strips. . . 28
2.17 Schematic of (a) a planar detector with a continuous electrode on the x-y surface and multiple electrodes on the right surface at z=t (b) Weighting potentials occurs on pixel 1 and 0 when an interaction occurs at point C in (a). Reproduced from [9]. . 30
2.18 A simplified schematic diagram of a resistive feedback charge sensitive preamplifier. 31
2.19 Charge sensitive preamplifier pulse acquired from a silicon detector, irradiated by a 511 keV incident gamma ray from a ^{22}Na point source. 31

3.1 An image of the Infina Hawkeye dual headed SPECT system located in the Medical Teaching and Research Laboratory (MTRL) STFC Daresbury. 36

3.2 Medical functional image of a parathyroid study [25], generated by the Ge Infinia Hawkeye dual headed SPECT system when used in Leeds General Hospital. 37
3.3 Schematic diagram of the main components of a gamma camera. 39
3.4 A magnified view of a typical parallel-hole collimator. Reproduced from [1]. 40
3.5 Schematic illustrations of the collimator types used in SPECT: (a) parallel-hole, (b) diverging, (c) converging and (d) pin-hole collimators. The shaded region represents the field of view [2]. 41
3.6 Schematic diagram of a Compton imaging system comprising of two planar detectors. Illustrated is two single-single events and their corresponding conics, the overlap of which indicates the location of the gamma-ray source. 48
3.7 Photograph of the ProSPECTus aluminum cryostat. Shown in gold are the individual preamplifier signal connection points of each strip for both detectors. 49
3.8 Photographs of (a) four vials with the sizes used in this thesis i.e diameters of 10 mm, 11 mm, 12.4 mm and 16.4 mm, (b) the holder and (c) a schematic drawing of the phantom holder. 55

4.1 Photograph showing the detector cryostats placed within the custom made frame. 57
4.2 Photographs of the ProSPECTus detectors in their cryostats and connected to their respective cooling systems (a) Si(Li) detector and CryoPulse cooling system. (b) Absorber 1 HPGe detector and LN_2 dewar. (c) Absorber 2 HPGe detector and CryoPulse cooling system. 59
4.3 Schematic drawing of the active volumes of the (a) scatter (Si(Li)) detector and (b) absorber 1 and 2 (HPGe) detector dimensions. (Not drawn to scale). 61

4.4 Schematic drawing of the detector set up of the ProSPECTus system with the scatter and absorber 1 detectors. Shown is the cryostat and detector separation. The geometry is the same when absorber 2 is used except there is a cryostat separation of 16 mm and hence a detector to detector separation of 52 mm. (Not drawn to scale) 63
4.5 Schematic drawing of an estimate maximum Compton scattering angle θ_{max} allowed for single-single interactions with the ProSPECTus system geometry (with absorber 1). Assuming detectors are centrally aligned. Diagram is not drawn to scale. 64
4.6 Schematic representation of a preamplifier pulse exceeding a user defined trigger threshold point and thus being stored (represented by blue window) with a user defined number of samples before and after the threshold crossing point. 65
4.7 Schematic of the digital signal processing electronics used for data acquisition. 66
4.8 Screenshot of the software used to set parameters in the CAEN V1495 cards. Highlighted in blue are the main settings i.e. trigger width (multiply value by 25 to get desired coincidence window in ns), Output all masked channels (stores events from all strips) and detector coincidence (stipulates which sides of the detectors to accept trigger events). 68
4.9 Schematic representation of MWD algorithm processing of preamplifier signals. 69
4.10 Energy resolution measured at a gamma-ray energy of 166 keV for (a) the scatter detector and (b) the absorber 1 detector. (c) Absorber 2 detectors resolution for an incident gamma ray of 122 keV. All measurements made using digital electronics and the MWD parameters shown in Table 4.1 71
4.11 Screenshot of the MIDAS software user interface that runs the MTsort program developed at the University of Liverpool. A variety of useful spectra can be created, accessed and viewed using MTsort and the MIDAS software 73

4.12 Fold [1,1,1,1] gamma-ray energy addback spectrum of the AC side of the scatter and absorber 1 detectors, produced using a ^{139}Ce source. 74
4.13 A GAMOS simulated energy distribution of fully absorbed coincident single-single events, in the ProSPECTus for 166 keV incident gamma ray energy. The simulations were run with the same ProSPECTus geometry used with absorber 1 i.e. 46 mm detector separation and point source placed 65 mm from scatter cryostat. 76
4.14 Plot showing the calculated energy deposited in the scatter detector for incident 166 keV gamma rays as a function of scattering angle between 5 and 180 degrees. 76
4.15 Energy spectrum collected with strip AC04 of the Si(Li) detector using a ^{241}Am source. Noise is observed up to 4 keV. . 78
4.16 Schematic representation of the analogue electronics used for the intrinsic HPGe/Si(Li) TAC measurements. 79
4.17 ^{22}Na gamma ray energy spectrum collected with Si(Li) strip AC06. The spectrum is clearly dominated by Compton events, in the energy range < 340 keV. 81
4.18 Intrinsic Analogue HPGe and NaI(Tl) TAC peak from strip AC09, generated from coincident events from ^{22}Na a (511 keV) source. The FWHM of this peak is 18 ns. 81
4.19 Schematic representation of the analogue electronics and CAEN digitisers used for the intrinsic HPGe/Si(Li) coincidence peak timing measurements. 83
4.20 Schematic diagram showing how the timing resolution for the CAEN digitsers were measured. 84
4.21 Rate of Compton imaging events for (a) 511 keV gamma rays and (b) 166 keV gamma rays, for a range of coincidence window times from 50 to 400 ns. The errors are not displayed on the graph as they have been calculated using Poisson statistics to be less than 5 %. 87

4.22 (a) Rate of coincidence events for 166 keV gamma rays using optimised settings. (b) Differentiated values from plot of (a). All true coincidence events take place within a window between 25 and 125 ns, therefore a timing window of 150 ns was chosen. 88
4.23 Schematic diagrams of how the analytical image reconstruction code, creates conics on an imaging plane using trigonometric calculations. 90

5.1 Analytical reconstruction of a ^{139}Ce point source generated by coincidence data acquired with absorber 1 ProSPECTus configuration. The image has been reconstructed at Z-slice 160 mm with a compression factor of 1. 95
5.2 Graphs of the maximum number of cone intersections in a single voxel normalised to the total number of cone intersections in its image slice as a function of Z-slice (mm). This corresponds to a ^{139} Ce source placed 65 mm from the scatter cryostat of ProSPECTus configured with absorber 1, generated from (a) Experimental data and (b) GAMOS simulated data. 97
5.3 Intensity profiles of the ^{139}Ce point source measurement acquired with the ProSPECTus absorber 1 configuration. (a) X-intensity profile and (b) Y-intensity profile, through point of maximum intensity. 99
5.4 Iterative reconstruction images of a ^{139}Ce point source, produced after (a) 1 (b) 10 (c) 21 and (d) 22 iterations. All images are reconstructed at a Z-slice of 160 mm and are reconstructed with a compression factor of 1. 101
5.5 (a) 1st reconstruction with Lorentzian peak fit with quadratic background fit to data and (b) 10th reconstruction with Gaussian fit to data. 102

5.6 Plot of FWHM as a function of iteration number for a ^{139}Ce point source. Iteration 0 is from the analytical reconstruction algorithm and is included in this plot for completeness. All images for these results were reconstructed with a compression factor of 1 at a Z-slice of 160 mm. 103
5.7 DC Fold[1,1,1,1] addback spectrum collected from a ^{139}Ce point source placed 40 mm from the detector cryostat. This measurement was used to determine the efficiency of the ProSPECTus system. 105
5.8 Calculated activity of (a) The total volume of the radiation sources calibrated from time 0 at the Royal Liverpool University Hospital (b) The individual 16.4 mm vial and 10 mm diameter vial for ^{99m}Tc and ^{123}I from the time of the first coincidence data measurement. 107
5.9 Photograph of the 16.4 mm diameter vials filled with ^{99m}Tc and ^{123}I placed 6 cm apart (centre to centre), during data acquisition. 108
5.10 ^{99m}Tc energy spectra acquired with the CAEN cards set in 'singles' modes for (a) strip AC07 of the scatter detector and (b) strip AC07 of the absorber 2 detector. 110
5.11 ^{123}I energy spectra acquired with the CAEN cards set in 'singles' modes for (a) strip AC07 of the scatter detector and (b) strip AC07 of the absorber 2 detector. 111
5.12 Experimentally acquired energy spectrum showing the energy deposited from the fully absorbed Fold [1,1,1,1] events in the scatter detector and absorber 2 detector for incident gamma rays from ^{99m}Tc and ^{123}I. 112
5.13 GAMOS simulated fully absorbed coincidence Fold[1,1,1,1] energy deposits expected in the scatter detector and absorber 2 detector for incident gamma rays of ^{99m}Tc and ^{123}I. 113

5.14 Gamma-ray energy spectrum collected during data acquisition of the the two 16.4 mm diameter vials containing ^{99m}Tc and ^{123}I. The energy resolution calculated at 141 keV and 159 keV was 2.82 keV and 2.80 keV, respectively. The 185 keV peak arises due to coincidences between the 159 keV gamma ray and 27 keV x-rays of ^{123}I. 115
5.15 Energy spectrum acquired with Na(Tl) detector for incident gamma rays energies of 141 keV and 159 keV from ^{99m}Tc and ^{123}I respectively. 116
5.16 (a) An image of the 16.4 mm diameter ^{99m}Tc and ^{123}I vials placed parallel to scatter the cryostat, produced by analytical reconstruction and (b) the X Intensity profile through point of maximum intensity in the corresponding image. A compression factor of 2 was used in image reconstruction therefore each pixel represents 2 mm in phase space. 118
5.17 Inverse sensitivity matrix, used to normalise the sensitivity in the ProSPECTus field of view as a function of position at a fixed Z position. The centre of this matrix was repositioned to X= 411 pixel in order to compensate for the detector offset. 119
5.18 (a) Image of ^{99m}Tc and ^{123}I reconstructed with the analytical reconstruction algorithm and with field of view sensitivity normalisation. (b) X-intensity profile through point of maximum intensity in image (a). 120
5.19 Graph displaying the percentage of the intensity in the ^{99m}Tc vial to that of the ^{123}I vial as a function of iteration number. . 121
5.20 Iterative reconstruction images of the parallel ^{99m}Tc and ^{123}I vial at the (a) 2nd iteration (c) 6th iteration and (f) 12th iteration. The corresponding X-intensity profiles are given in figures (b), (d) and (e) respectively. 122
5.21 (a) 3rd iteration reconstruction of ^{99m}Tc and ^{123}I vials with 6 cm centre to centre separation, compression factor of 2 used in image reconstruction (b) Intensity profile through point of maximum intensity in the X direction. 123

5.22 3rd iteration reconstruction of (a)^{99m}Tc vial using an energy gate of 135 keV to 144 keV and with a compression factor of 2. (b) X-intensity profile through point of maximum intensity (X=117) (c) Y-intensity profile through point of maximum intensity (Y=133). 124
5.23 3rd iteration reconstruction of (a)^{123}I vial using a energy gate of 154 keV to 161 keV and with a compression factor of 2. (b) X-intensity profile through point of maximum intensity (X=148) (c) Y-intensity profile through point of maximum intensity (Y=132). 125
5.24 (a) 3rd iteration image of superimposed ^{99m}Tc vial and ^{123}I vials (b) Intensity profile of superimposed image through point of maximum intensity in the X direction. 127
5.25 (a) Photograph of the phantom holder with labels showing the position of the 16.4 mm diameter vials filled with ^{99m}Tc, ^{123}I and ^{139}Ce and (b) centre of phantom , aligned with centre of scatter detector for data acquisition in polystyrene phantom holder. 128
5.26 Fold [1,1,1,1] energy add-back spectrum collected during data acquisition. The FWHM is 2.71 keV, 2.63 keV and 2.70 keV for ^{99m}Tc,^{123}I and ^{139}Ce respectively. Average digital threshold in absorber 2 set at 90 keV and in the scatter detector 8 keV. 129
5.27 Iterative reconstruction of three 16.4 mm diameter vials placed in phantom holder. Rods filled with aqueous solutions of ^{99m}Tc ,^{139}Ce and ^{123}I . (a) 3rd iteration reconstruction experimental image (b) 6th iteration reconstruction experimental image (c) Superimposed experimental image, using 4th iteration individual vial images in matrix. 131
5.28 Experimental 4th iteration image of three 16.4 mm ^{139}Ce filled vials. Data acquired with phantom holder 65 mm from scatter cryostat, with centre of middle vial, aligned with the centre of the scatter cryostat. 132

5.29 4th iterative reconstruction images of (a) ^{139}Ce (b) ^{123}I (c) ^{99m}Tc. All images are reconstructed individually through energy gates, that are defined in Table 5.2 135
5.30 Superimposed images for (a) 1st iteration (b) 2nd iteration and (c) 3rd iteration reconstructed vials. 140
5.31 Labeled photograph of phantom, detailing which vials contained ^{99m}Tc and which contained ^{123}I. 140
5.32 Phantom containing all vials either filled with ^{99m}Tc and ^{123}I. The 10th iteration image is shown with a compression factor of 2 and a Z-slice position of 166 mm. 141
5.33 X-intensity profiles for iteration numbers (1, 3 and 7) through a ^{99m}Tc 16.4 mm diameter vial of experimental data the ideal expected profile (red) through a vial when neglecting physics effects. 142
5.34 ER profile for iteration 5 of the 16.4 mm ^{99m}Tc vial placed at position 1 in phantom. The vial size is measured from the difference in X(pixels) from 10% to 90% peak height. 142
5.35 Schematic diagram of how the subset of vials in terms of size are separated in the phantom holder. The ER function is used to determine when the iterative reconstruction algorithm produces an image where the diameter of the vial is reconstructed to the correct size. 143
5.36 X-intensity profile (blue), through the 5th iteration image of two superimposed 16.4 mm diameter sized vials. Each pixel represents 2 mm in phase space. The red profiles represent the ideal intensity distribution of the vials. 143
5.37 Edge-Response values (mm) as a function of iteration number for vial sizes of diameter (a) 16.4 mm (b) 12.4 mm (c) 11 mm and (d) 10 mm. 145

5.38 ER profiles for the (a) 16.4 mm vial at iteration 5 (b) 12.4 mm vial at iteration 9 (c) 11 mm vial and (d) 10 mm vials at iteration 10. These profiles are at the iteration number which give an ER that is representative of the corresponding vial diameter. Each pixel represents 2 mm in phase space. 146
5.39 Superimposed images for vial size subsets of the phantom, at the iteration number that shows resolvability, as predicted by the ER results (a) 16.4 mm diameter vials at the 5th iteration reconstruction, (b) 12.4 mm diameter vials at the 8th iteration reconstruction, (c) 11 mm diameter vials at the 10th iteration reconstruction, and (d) 10 mm diameter vials at the 10th iteration reconstruction. All images reconstructed with a compression factor of 2. 148
5.40 Superimposed image of all the phantom vial subsets, reconstructed at their respective iteration number according to the ER results. 149

List of Tables

2.1 Key propeties of the NaI(TL) and BGO scintillator detectors, [15] [9]. 16
2.2 The key properties of silicon and germanium. 17

3.1 Attributes and uses of the most commonly used radionuclides in Single Photo Emission Computed Tomography [23] [27]. . 38
3.2 The properties of the different types of parallel hole collimator available for use with a 400 mm diameter gamma camera. Details are provided about the typical septa thickness (t), hole diameter (d), Number of holes (N), efficiency (g), maximum energy (E_{max}) and spatial resolution (R_{coll}). Details reproduced from [1] [32]. 43

4.1 Table showing user defined MWD parameters for scatter, absorber 1 and absorber 2 detectors. Parameters are for both AC and DC sides of the detector, unless otherwise stated. . . 69
4.2 Average energy resolution for the AC and DC sides of the scatter, absorber 1 and absorber 2 detectors, acquired with Caen digitizer cards. The energy resolutions provided are for incident gamma rays of 166 keV energy and for the absorber 2 detector at 122 keV. All errors shown are calculated from the standard deviation of the data used to calculate the averages. 71
4.3 Table displaying the average timing resolution of both the Si(Li) and HPGe detectors. The average timing response is shown for the AC and DC sides of both detectors as well as the overall average timing response. 82

4.4 Consistency check using Equation 4.1 to check if the average timing resolutions are consistent when being measured with the analogue electronics and with using the digitiser cards. . . 85
4.5 Table displaying the timing resolution of the ProSPECTus system, of the selected strips, chosen to demonstrate the timing response at the geometrical extremities of the system. Each value is considered to have an associated error of 1 ns. 86

5.1 Efficiency results for the different event types discussed, also quoted is the improvement over conventional SPECT systems. 104
5.2 Energy gates used for the ^{99m}Tc, ^{123}I and ^{139}Ce photopeaks in image reconstruction. 127

6.1 Table displaying the average timing resolution of both the Si(Li) and HPGe detectors. The average timing response is shown for the AC and DC sides of both detectors as well as the overall average timing response. 151

A.1 Calibration coefficients for each individual strip of the scatter detector. 157
A.2 Calibration coefficients for Absorber 1 detector 158
A.3 Calibration coefficients for Absorber 2 detector 159
A.4 The energy resolution for each strip of the scatter detector at 60 keV and 122 keV. Results acquired with analogue electronics. 161
A.5 The energy resolution of each strip of the scatter detector at gamma-ray energies of 60 keV, 122 keV and 166 keV. Results determined after digital processing. 162
A.6 The energy resolution for each strip of the absorber 1 detector at 60 keV and 122 keV. Results acquired with analogue electronics. 163
A.7 The energy resolution of each strip of the scatter detector at gamma-ray energies of 60 keV, 122 keV and 166 keV. Results determined after digital processing. 164

A.8 The energy resolution for each strip of the absorber 2 detector at 122 keV. Results acquired with analogue electronics. 165
A.9 The energy resolution of each strip of the absorber 2 detector at 122 keV. Results determined after digital processing. 166
A.10 Timing resolution of each channel from the scatter detector. The timing response determined from the analogue electronics and digital electronics investigations is provided. 167
A.11 Timing resolution of each channel from the Absorber detector. The timing response determined from the analogue electronics and digital electronics investigations is provided. 168

Chapter 1

Introduction

Medical imaging is an expanding field tasked with not only improving diagnostic capabilities but also delivering assistance in the planning, tracking and treatment of malignant diseases. The technological advancements that are occurring in medical imaging have a foundation based on physics principles. Advances in nuclear physics, detector physics and accelerator physics are continually combined in order to improve the quality, cost-effectiveness, efficiency, accuracy and safety of current and new imaging modalities. This thesis is an investigation into the feasibility and performance of the ProSPECTus Compton camera system for its intended application in nuclear medicine [1] [2].

1.1 Nuclear Medicine

Nuclear medicine studies provide clinical information through observation of the uptake and distribution of a radiopharmaceutical that is administered to a patient, in order to accumulate in a region of interest. The images generated in nuclear medicine studies are classified as functional images, as they provide details on the physiological processes occurring in the body such as blood flow, organ function and metabolic processes. Nuclear medical imaging systems can be divided into two main classes: Single Photon Emission Computed Tomography (SPECT) and Positron Emission Tomography

(PET). Outside the field of nuclear medicine, imaging modalities primarily provide anatomical information such as bone structure, tissue structure and organ location. X-ray, Computed Tomography (CT) [3] and Magnetic Resonance Imaging (MRI) [4] systems are widely used in clinical environments to produce anatomical images. Both functional and anatomical images contain useful information, therefore it is advantageous to acquire both simultaneously. This has led to the to the development of co-registry between imaging modalities for example SPECT-CT/PET-CT scanners [5] and PET-MRI/SPECT-MRI scanners [6] [7].

1.1.1 Single Photon Emission Computed Tomography

The work in this thesis is based on the development of a system to overcome the limitations of SPECT systems, through changing the radiation detection and image reconstruction methodology. SPECT provides in vivo measurement for clinical assessments and has been used in healthcare since the late 1960's in a range of clinical applications, from brain imaging to bone density studies. It is the preferred imaging technique for myocardial perfusion studies and is essential for imaging new cerebral blood flow agents. SPECT systems are based on a gamma camera rotating around a patient, which detects gamma rays that are emitted from the radiopharmaceutical within the patient. The most commonly used radiopharmaceuticals used in SPECT are labelled with ^{99m}Tc (141 keV) and ^{123}I (159 keV). Functional images are produced by inputting the measured distribution of radiation as a function of angle to mathematical reconstruction algorithms.

The components of the gamma camera induce limitations in SPECT imaging. The main limiting factor of the gamma camera is the collimator, which is directly attached to a scintillator detector array in order to select incoming gamma-rays according to their direction of incidence. The collimator leads to a restricted field of view, poor sensitivity and a trade off between the sensitivity and spatial resolution of the image, which has detrimental implications on patient dose and throughput. The poor energy resolution of the scintillator crystal, 10-12% at 141 keV, leads to large uncertainties in the

discrimination of gamma-rays that have scattered in the patient and/or collimator, which can induce artefacts in the image. The poor energy resolution also limits the ability to perform multi-isotope simultaneous imaging, which would otherwise be useful to monitor multiple biological processes within one scan. In particular, simultaneous acquisition of data from ^{99m}Tc and ^{123}I relies on complex peak deconvolution techniques, which results in large uncertainties [8]. Therefore it is likely that multiple SPECT scans would be undertaken sequentially to complete a study of the patient. To overcome the limitations of conventional SPECT systems an interdisciplinary group have worked towards the design of an alternate system based on a Compton camera. This system has been developed at University of Liverpool in partnership with the STFC Daresbury laboratory and the Royal Liverpool University hospital.

1.2 The ProSPECTus Project

The ProSPECTus system is a novel SPECT system that employs semiconductor detectors in Compton camera mode. Collimation is achieved electronically with the use of two highly segmented detectors, so that no mechanical collimator is required, thereby improving the sensitivity and field-of-view. The principle of Compton imaging is that a gamma ray interacts at least once in each detector and deposits its full energy. Information on the energy deposited and positions of gamma-ray interaction within each detector is then used with a kinematic reconstruction algorithm based on the Compton scatter formula to locate the source position of the incoming radiation. The significantly improved energy resolution that semiconductors offer compared to scintillator crystals will enable the simultaneous acquisition of data from multiple medical isotopes without the need for complex deconvolution algorithms that are otherwise required with SPECT systems. The feasibility of multi-isotope imaging is highlighted in this thesis. In future work, the ProSPECTus project also aims to deliver co-registry with MRI systems.

1.3 Thesis Outline

A prototype ProSPECTus system was used in this thesis to achieve the following objectives:

- Optimise and define operational settings for the ProSPECTus system, for imaging SPECT radioisotopes.
- Investigate the feasibility of simultaneous multi-isotope imaging with ^{99m}Tc (141 keV) and ^{123}I (159 keV).
- Quantify the imaging performance of the ProSPECTus system.
- Identify any potential limitations of the ProSPECTus system.

The work presented in this thesis and the steps taken in order to realise the above objectives were:

1. Detailed investigations into the intrinsic timing properties of the ProSPECTus detectors in order to determine the optimum coincidence window.
2. Implementation and assessment of noise thresholds in the data acquisition system.
3. Design of a custom made phantom, to perform experimental assessments of imaging performance.
4. Acquisition of data sets with varying complex distributions for the gamma-ray sources of ^{99m}Tc (141 keV), ^{123}I (159 keV) and ^{139}Ce (165 keV).

Chapter 2 outlines the fundamental aspects of gamma ray interactions with matter and detector technology that applies to the scope of this thesis. Chapter 3 provides an overview of the gamma ray imaging techniques of SPECT and Compton cameras and the design of the custom made phantom used for data acquisition. Chapter 4 describes the experimental setup of the prototype ProSPECTus system and the optimisation undertaken with

^{139}Ce, with a focus on the coincidence timing settings and noise thresholds. Presented in Chapter 5 is the analysis of data acquired with the prototype ProSPECTus system, which includes the feasibility studies for simultaneous multi-isotope data of ^{99m}Tc (141 keV) and ^{123}I (159 keV) and imaging complex source distributions. Chapter 6 provides an overview of the conclusions and recommendations that have been drawn from the work in this thesis.

Chapter 2

The Fundamentals of Gamma Ray Spectroscopy

2.1 Interaction of Gamma rays with Matter

Gamma rays have no charge, therefore upon interaction with matter they will not immediately cause ionization or excitation. Instead, it is the transfer of part or all of their energy to electrons in the detection material that causes these effects and enable the gamma rays to be detected in a radiation sensor through the generated response. Gamma rays interact with atomic matter via scattering or absorption events. Within the energy range of 10 keV and 2 MeV the three dominant mechanisms are Compton scattering, photoelectric absorption and pair production. However, in the work of this thesis, which focuses on energies of less than 200 keV, Compton scattering and photoelectric absorption are the gamma ray interaction processes of interest.

The atomic number of the detector material and the energy of the gamma ray influences which of the three interaction processes preferentially occurs. Compton scattering is the dominant interaction mechanism for gamma rays with energies between ∼150 keV to ∼6 MeV, whereas photoelectric absorption is most likely to occur for low energy gamma rays. For example, gamma rays that have an energy of less than 150 keV are most likely to undergo photoelectric absorption in germanium, a detection medium used in this thesis.

Gamma rays that have an energy in excess of 1022 keV are able to interact via pair production, but this does not become dominant until significantly higher in energy. The total linear attenuation coefficient μ_0 is a measure of the number of photons in a collimated gamma ray beam that interact, this is described by:

$$\mu_0 = \sigma + \tau + \kappa \tag{2.1}$$

where σ , τ and κ are the probabilities per unit length of a Compton scatter, photoelectric and pair production interaction occurring, respectively. The probability of a photon traversing a material without interacting is found by the product of the probabilities of survival for each interaction. For example, the probability of a gamma ray traveling through a material and not undergoing a photoelectric process is e^{τ}. Therefore the intensity (I) of collimated beam of gamma rays with initial intensity (I_0) after traversing a material of thickness (χ) can be determined via:

$$I = I_0.e^{-\mu_0 \chi} \tag{2.2}$$

Figure 2.1 shows the relative probabilities of σ, τ and κ as a function of Z for the detection material and incident gamma-ray energy, $E_{\gamma I} = hf$ (where h is planks constant and f is the frequency). The boundaries are shown for germanium (Ge) (red line) and silicon (Si) (blue line), which are the materials used for the detectors in this project. For the gamma-ray energies used in SPECT of ~ 0.1 MeV, it is shown that a Compton scatter event is more likely to occur instead of a photoelectric event in Si. This is an important concept when designing a Compton camera, the principles of which is described in Chapter 3.

2.1.1 Compton Scattering

The Compton scatter process is essential in understanding the operation of a Compton camera, as described in Section 3.3.1. A Compton scatter occurs when an incident gamma ray interacts with a weakly bound atomic electron in

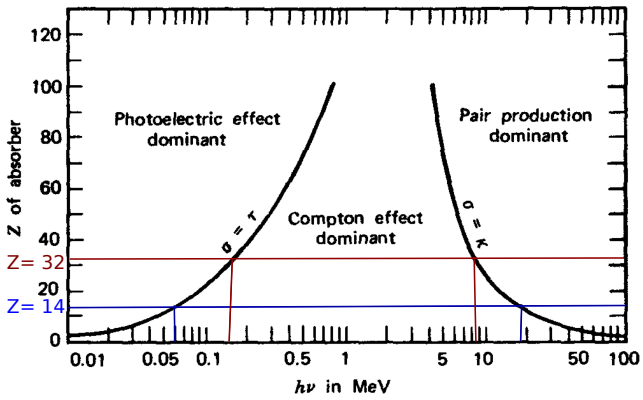

Figure 2.1: Graph displaying the probability of a gamma ray undergoing Compton scattering, photoelectric absorption and pair production as a function of gamma-ray energy ($E_{\gamma I} = hf$) and atomic number Z. The boundaries are shown for Ge (red line) and Si (blue line). The black lines represent the Z and E values where two neighboring effects are equally probable. Image reproduced from [9].

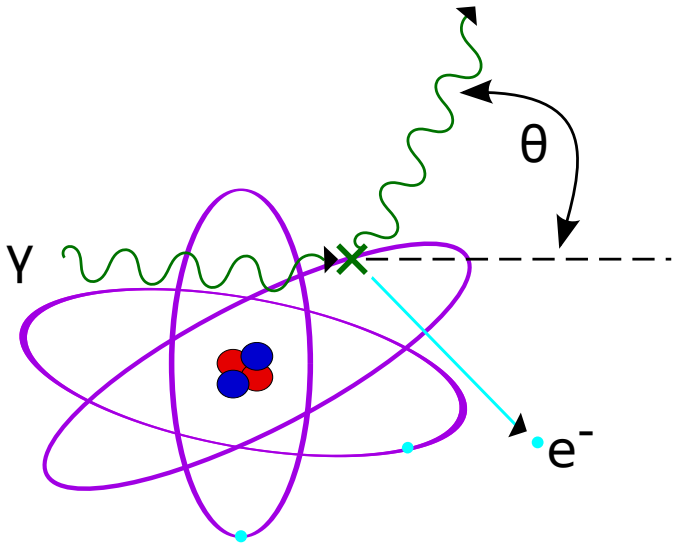

Figure 2.2: Schematic illustration of the Compton scattering process.

the detection material and is deviated by an angle θ from its original path, as shown in Figure 2.2. The atomic electron receives a proportion of the kinetic energy of the gamma ray and can subsequently escape from the atom. This electron is denoted the recoil electron. It is assumed that the atomic electron

is at rest when the interaction occurs, as this implies the binding energy of the electron is significantly less than the energy of the incident gamma ray. When the two energies are similar, the cross section for the photoelectric effect is considerably larger than that for Compton Scattering, causing the Compton Scatter effect to be negligible. The incident E_{γ_I} and scattered E_{γ_S} gamma ray energies are related to the scattering angle θ, by the Compton scatter formula:

$$E_{\gamma_S} = \frac{E_{\gamma_I}}{1 + \frac{E_{\gamma_I}}{m_e c^2}(1 - \cos\theta)} \tag{2.3}$$

This formula can be derived by treating the interaction between the gamma ray and the electron as a two body collision and applying both the conservation of energy and momentum laws. The absolute probability of a Compton scatter occurring increases linearly as Z of the detection material increases, i.e the number of electrons available for interactions increases. The expected angular distribution of the Compton scattered gamma rays can be calculated using the Klein-Nishina [10] equation, which gives the probability of an incident gamma ray of energy E_{γ_I} scattering through an angle θ into a solid angle $\frac{d\sigma}{d\Omega}$:

$$\frac{d\sigma}{d\Omega} = Z r_e^2 \left(\frac{1}{1 + \alpha(1 - cos\theta)}\right)^2 \left(\frac{1 + cos^2\theta}{2}\right) \left(1 + \frac{\alpha^2(1 - cos\theta)^2}{(1 + cos^2\theta)[1 + \alpha(1 - cos\theta)]}\right) \tag{2.4}$$

where

$$\alpha = \frac{E_{\gamma_I}}{m_e c^2} \tag{2.5}$$

and r_e is the classical electron radius. Figure 2.3 is a graphical representation of the Klein-Nishina distribution. It is shown that an increase in E_{γ_I} leads to an increase in the amount of gamma rays being forward scattered. Highlighted in purple is the distribution corresponding to 141 keV gamma rays, incident from the left scattered into an angle θ. The distribution for 141 keV is particularly interesting for this project as it is the most commonly investigated gamma-ray energy in SPECT.

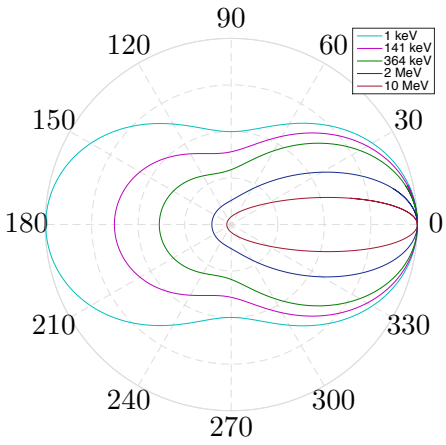

Figure 2.3: Graphical representation of the Klein Nishina formula which predicts the scattering angle for gamma rays of particular energies. The diagram is in polar co-ordinates and depicts the gamma rays incident from the left that are Compton scattered into a solid angle θ.

2.1.2 Photoelectric Absorption

Photoelectric absorption is the process in which a gamma ray is completely absorbed through interacting with an atomic electron cloud and subsequently replaced by an energetic photoelectron, as shown in Figure 2.4. Provided there is sufficient energy, the incoming gamma ray interacts with a bound atomic electron, which is normally ($\sim$80% likelihood [11]) residing in the K-shell. Due to conservation of momentum, the photoelectric process cannot happen between an incident gamma ray and a free electron. The electron must be atomically bound since it is the recoil of the entire atom after interaction, that ensures the conservation of momentum. The electron is then freed from the atom and has the kinetic energy E_e of the incident gamma ray with the deduction of the binding energy E_b, which is required to liberate the electron from its shell:

$$E_e = E_{\gamma_I} - E_b. \tag{2.6}$$

The removal of the electron leaves a vacancy in the corresponding atomic

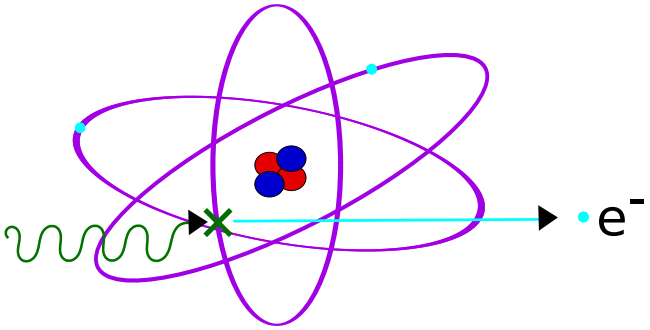

Figure 2.4: Schematic illustration of the photoelectric absorption process.

shell. To compensate for this, a higher orbital electron fills this vacancy and a characteristic X-ray is emitted. The probability of a photoelectric event occurring is represented by the atomic cross section σ_{PA} (cm^2/ atom). A detection material with a high Z number and a low E_{γ_I} gives an increased value of σ_{PA}, where the relationship is expressed as:

$$\sigma_{PA} = K.\left(\frac{Z^n}{E_{\gamma_I}^{3.5}}\right) \tag{2.7}$$

where K is a constant. The value of n has been found to vary between 4 to 4.6 as E_{γ_I} increases, from 0.1 MeV to 3 MeV [11], as shown in Figure 2.5.

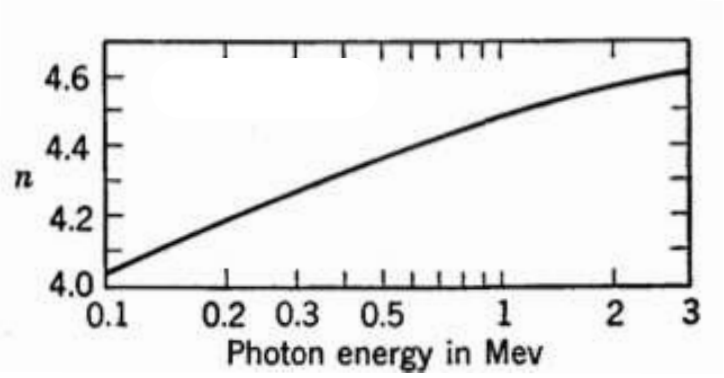

Figure 2.5: Approximate variation of the photoelectric cross section with Z^n, for various values of E_{γ_I}. Image reproduced from [11].

2.1.3 Pair Production

The pair production process is possible for gamma rays that have an energy in excess of 1.02 MeV, i.e. twice the rest mass energy of an electron. The interaction always takes place inside the Coulomb field of the nucleus, and the incident gamma ray is said to disappear and be replaced by an electron-positron pair, as depicted in Figure 2.6. These particles share as kinetic energy, the energy of the incident gamma ray that was excess to the 1.02 MeV required to produce the electron positron pair, as described in:

$$E_{\gamma_I} = (T_- + m_e c^2) + (T_+ + m_e c^2) \tag{2.8}$$

where T_- and T_+ are the kinetic energies of the electron and positron, respectively [11]. The positron typically only travels a few mm in most common detector materials before annihilating with a different electron and producing two 511 keV gamma rays that are shown to be separated by 180^0 in Figure 2.6. The colinearity is in coherence with the conservation of momentum laws, which assumes the particles are at rest at the time of annihilation. However, this is not necessarily always the case which can sometimes lead to acollinearity between the photons.

2.2 Interaction of Charge Carriers

Charge carriers refer to the unbound electrons and holes (vacancy in atomic shells) that are created when a gamma ray interacts with a detection medium, via one of the processes described above. There are two types of interactions that the electrons can experience; collisional losses $\left(\frac{dE}{dx}\right)c$ and $\left(\frac{dE}{dx}\right)r$ radiative emissions (Bremsstrahlung). The summation of both processes gives the total linear stopping power for electrons:

$$\frac{dE}{dx} = \left(\frac{dE}{dx}\right)c + \left(\frac{dE}{dx}\right)r \tag{2.9}$$

Collisional losses are predominant compared to radiative losses, where the ratio of the processes can be approximated as:

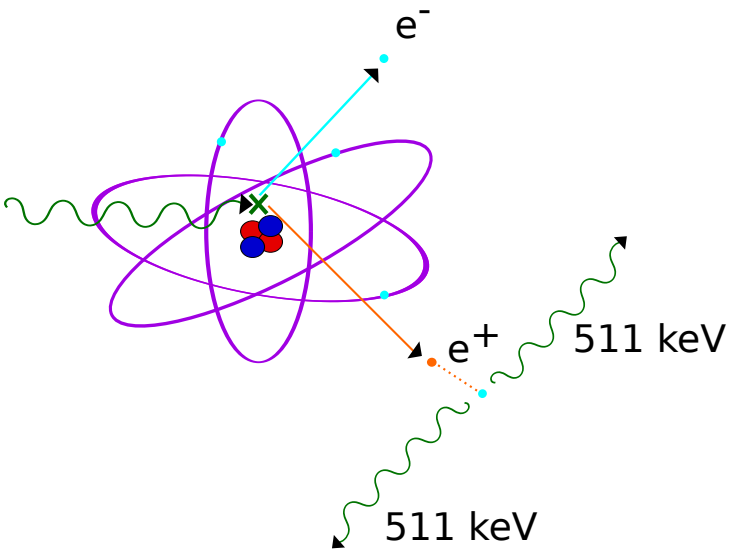

Figure 2.6: Schematic illustration of a gamma ray interacting via the pair production process.

$$\frac{EZ}{700} \cong \frac{(dE/dx)r}{(dE/dx)c} \tag{2.10}$$

Since the radiative losses only become prominent when the electron energy is > 3 MeV or the absorber material has a large atomic number, the radiative losses are negligible in the work of this thesis.

2.2.1 Collisional Losses

When electrons lose energy through ionization and excitation this is referred to as collisional losses. The Bethe Bloch formula quantifies the specific energy loss as :

$$-\Big(\frac{dE}{dx}\Big)c = \frac{2\pi e^4 NZ}{m_o v^2}\Big(\ln\frac{m_o v^2 E}{2I^2 k}\Big) \tag{2.11}$$

where $k \equiv 1-\beta^2$ and $\beta \equiv \frac{v}{c}$. This is for a electron that has velocity v and is incident on an absorbing material with atomic number Z and number density N. I defines the average excitation and ionization that occurs through elastic and inelastic scattering collisions with both nuclei and bound atomic

electrons.

2.3 Principles of Gamma ray Detectors

The interaction mechanisms described previously enable detector systems to generate proportional responses to the energy deposited and/or the number of gamma rays detected. This section describes the operational principles of the gamma ray detector types used in the work for this thesis.

2.3.1 Scintillator Detectors

Scintillator detectors have been in use for radiation detection since the 1940's [12]. Conventional nuclear medical imaging systems use a scintillator crystal as the detection medium, as described in Section 3.2.1. Scintillator detectors have also been used in this project for timing resolution and energy resolution measurements in Sections 4.2.6 and 5.0.11 respectively. Therefore, the operation of a scintillator detector and the characteristics of certain scintillator materials are briefly described in the subsequent sections.

Principles of operation

Figure 2.7 is a schematic drawing of the main components in a scintillator detector. The principle of operation is that an incoming gamma ray enters the scintillator crystal and causes fluorescence, i.e the emission of visible light within 10^{-8} seconds of the gamma ray absorption. The light is then transmitted to the Photomultiplier Tube (PMT) through the light guide. The first component in the PMT is the photocathode, which creates a stream of electrons from the incoming light via the photoelectric effect. The number of electrons is amplified through applying a voltage that accelerates the initial electrons onto a series of dynodes. At each dynode, secondary electrons are created, which causes an electron cascade through the PMT until the electrons are collected at the anode. The anode generates a current that can be processed and analysed. Due to the magnetic incompatibility of PMTs, that arises because of the magnetic field interfering with the electron trajectory

to the dynodes, there are modern alternatives used in nuclear medicine, such as Avalanche Photodiodes (APDs) [13] and Silicon Photomultipliers (SiPMs) [14].

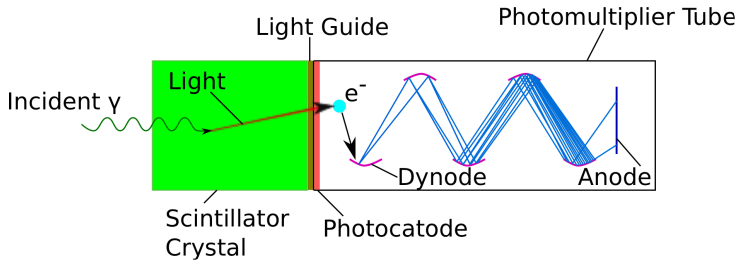

Figure 2.7: Schematic drawing of the main components of a scintillator detector.

Scintillator materials

An ideal scintillator material should possess the following characteristics [15] [9]:

- A short decay constant.
- Transparent to its own fluorescence for good light collection.
- High scintillation efficiency, i.e conversion of the kinetic energy of charged particles into light.
- The conversion should be linear, i.e light yield proportional to energy deposited over a wide range.
- The refractive index should be similar to that of glass i.e ∼1.5, so that optimum coupling is achieved between the crystal and the PMT.
- Production should be available in sizes that are suitable for radiation detection.
- The emission should be within a spectral range that is consistent with the spectral response of existing photomultipliers.

There are currently 6 types of scintillator detector materials in use these are: inorganic crystals, organic crystals, organic liquids, glasses, gases and plastics. For the work in this project an inorganic crystal Thallium activated sodium iodide Na(Tl) is used, which is the most commonly used scintillator material and is also the detection medium found in conventional SPECT (Single Photon Emission Computed Tomography) systems. The properties of the Na(Tl) scintillator material is found in Table 2.1, along with the properties of Bismuth germanate (BGO) for comparison, which is used in Positron Emission Tomography (PET) systems.

Material	**Density (g/cm^3)**	**Refractive Index**	**Decay Constant (μs)**	**Wavelength (nm)**
NaI(Tl)	3.67	1.775	0.23	413
BGO	7.13	2.15	0.30	480

Table 2.1: Key propeties of the NaI(TL) and BGO scintillator detectors, [15] [9].

2.3.2 Semiconductors

Semiconductors have been used as a radiation detection medium since the 1960's. They offer many advantages over scintillator detectors particularly in energy resolution, compact size and the variance in thickness depending on the application. Table 2.2 displays the key properties of Si and Ge, the detection materials used for the work in this thesis. The subsequent sections explain the principles behind using semiconductors as a radiation detectors, where appropriate these are explained in relation to Si and Ge.

Property	Silicon	Germanium
Atomic number	14	32
Density (300 K) (g/cm^3)	2.33	5.32
Band gap energy (0K)	1.165 eV	0.746 eV
Band gap energy (300 K)	1.115 eV	0.665 eV
Dielectric constant	11.9	16.32
Energy per electron -hole pair (77 K)	3.76 eV	2.96 eV
Electron mobility (cm^2/V-s) (300 K)	1450	3900
Hole mobility (300 K) (cm^2/V-s)	505	1800

Table 2.2: The key properties of silicon and germanium.

Crystal and Band Structure

The energy bands for electrons in a crystalline structure are determined by the periodic lattice structure of the material. Si and Ge are both diamond lattice type crystals. The crystal structures are based on the face-centered cubic Bravais lattice as displayed in Figure 2.8 [16]. Miller indices provide a standard method to define a plane within the crystal lattice. Figure 2.9 displays the notation and description of the miller indices. This is useful, as certain semiconductor properties are inherent to the crystal plane used.

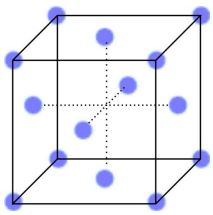

Figure 2.8: Schematic drawing of a Face Centred Cubic (FCC) lattice structure. Si and Ge have this crystal configuration.

For simplicity, the band structure can be described in terms of the valence band, conduction band and the energy gap between them. The valence band consists of outer shell electrons that are bound to lattice sites, whereas the conduction band consists of unbound electrons. The band structure and

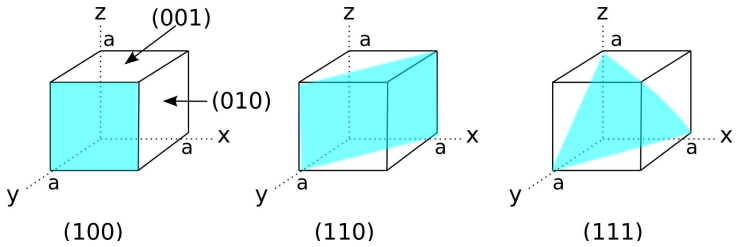

Figure 2.9: Examples of the Miller indices notation, which are used to describe planes in crystal lattice.

energy gap determines if a material is classified as a conductor, insulator or semiconductor. The structure of these are as follows:

- Conductor: The conduction and valence bands overlap or the conduction band is not filled. Only a small amount of kinetic energy is needed for valence electrons to be promoted to the conduction band because there is no band gap.

- Insulator: Has a minimum band gap of 5 eV. Thermal excitations are not sufficient to promote valence electrons to the conduction band.

- Semiconductor: Has a small band gap $\sim$ 1 eV. Thermal excitations are sufficient to allow valence electrons to move to the conduction band.

Figure 2.10 is a simplistic representation of the band structure of a conductor, insulator and semiconductor. The energy band gap diagram for a semiconductor is given by the energy (E)-momentum (ρ) relationships. Figure 2.11 displays the conduction and valence bands for Ge, Si and gallium arsenide (GaAs) for two crystal orientations. It can be seen that near the minimum of the conduction band and hence maximum of the valence band the E-ρ curves are parabolic. For the example of silicon the maximum in the valence band occurs at ρ =0 whereas the minimum of the conduction bands occurs along the [100] direction at $\rho = \rho_c$ [17]. This means that for an electron to make a transition from the maximum of the conduction band it requires both an energy change ($\geq$ E_g) and a momentum change ($\geq$ ρ_c). Materials that require the additional momentum change along with the energy change to liberate an electron are called indirect semiconductors, Si and

Ge are examples. If a momentum change is not needed for eg in GaAs, it is classed as a direct semiconductor. The band structure for GaAs is also included in Figure 2.11 for completeness.

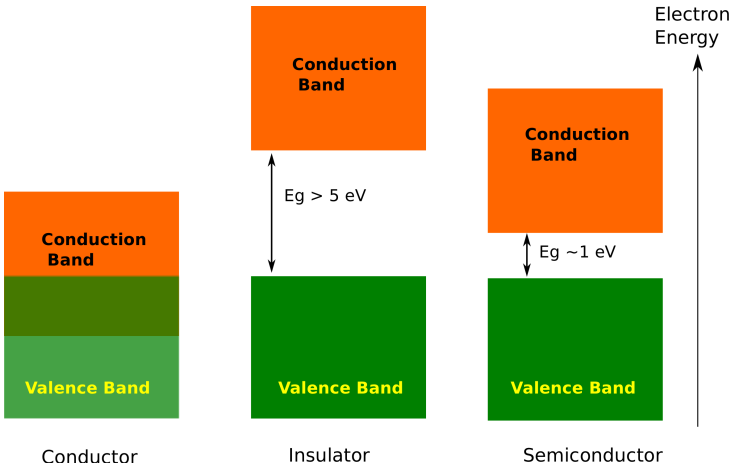

Figure 2.10: Schematic diagram of the band structure in a conductor, insulator and semiconductor

Charge Carrier Generation

When a valence electron is promoted to a conduction band in a semiconductor, a hole is created. A neighbouring valence electron can fill this hole, thus leaving a hole in its original position. This repeated phenomenon of hole creation and filling, appears as a moving hole (charge carrier). The hole acts as a positive charge and its movement generates a electric current. The electron-hole pairs are therefore the charge carriers in semiconductor materials. The interaction of a gamma ray leads to the generation of many electron-hole pairs. The number of electron-hole pairs created N_{eh} is dependent on the incident gamma ray energy E_{γ_I} and the ionisation energy E_{pair} of the material, as shown in Equation 2.12.

$$N_{eh} = \frac{E_{\gamma_I}}{E_{pair}} \tag{2.12}$$

The electrons that are liberated in the material cause ionisation and excitations as they travel in the detector material before coming to rest. This

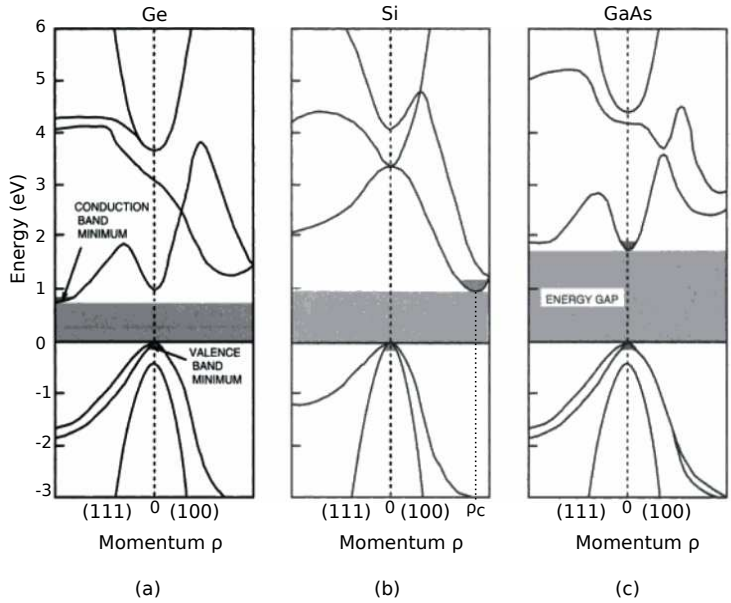

Figure 2.11: Energy band structures of indirect semiconductors: a) Ge b) Si and a direct semiconductor c) GaAs. The shaded regions represent the minimum of the conduction and energy bands aswell as the energy band gaps. Reproduced from [18].

happens over a relatively small volume of the detector described as a charge cloud.

Charge Carrier Mobility

Electrons are subject to thermal motion which is essentially a continuous motion of random scatters on encounter with lattice atoms and impurity atoms [17]. If an electric field $\vec{E}$ (Vcm^{-1}) is applied, each electron will be under a force of $-q\vec{E}$ and will therefore be accelerated, opposite and parallel to the electric field direction, in-between collisions. The electrons and holes now acquire a drift velocity of υ_e and υ_h respectively, which can be expressed as:

$$\upsilon_e = \mu_e \vec{E} \tag{2.13}$$

$$\upsilon_h = \mu_h \vec{E} \tag{2.14}$$

where μ_e and μ_h are the electron and hole mobilities respectively (cm^2/V-s). The mobility constants are dependent on the semiconductor properties and are related to the mean free time (average distance between collisions) and the effective mass of the electron. Due to the effects on crystal vibration, temperature also influences the electron and hole mobility constants, such that as the temperature increases μ_e decreases. Therefore the drift velocity is a function of $\vec{E}$ and temperature (T). For example, in Si at standard temperatures the mobility μ for electrons and holes is constant for $\vec{E}$ <10^3 V/cm, therefore the relationship between velocity and $\vec{E}$ is linear. When $\vec{E}$ is between 10^3- 10^4 V/cm, μ changes approximately as $\vec{E}^{-12}$, above 10^4 V/cm, μ varies as $1/\vec{E}$. This leads to the velocity saturating whilst approaching a constant value of $\sim 10^7$cm/s. At this point the velocity is independent of further increases in electric field. The saturation is due to the electrons and holes losing a proportional fraction of the gained kinetic energy through collisions with lattice atoms [15]. For semiconductor radiation detectors it is preferable to operate the saturation drift velocity so that the velocity of the charge carriers is known and recombination of charge carries is less likely. Figure 2.12 (reproduced from [19]) shows the electron and hole drift velocities as a function of electric field for silicon at three different temperatures.

Doping

Intrinsic semiconductors are classed as those that are made from pure material. Extrinsic semiconductors contain impurities either by natural formation or through intentional dopant addition during the fabrication process in order to alter the conductivity of semiconductors. Doped semiconductors are either classed as n-type or p-type depending on the donor impurity. An example of an n-type semiconductor is phosphorus doped silicon, in which a pentavalent phosphorus atom substitutes the place of a silicon atom within the crystal lattice. The phosphorus atom forms four covalent bonds, the extra electron forms a weak bond, that can be promoted into the conduction band with a small amount of energy, typically 0.01 eV. These donor electrons (N_D) occupy energy levels known as donor levels within the band gap near

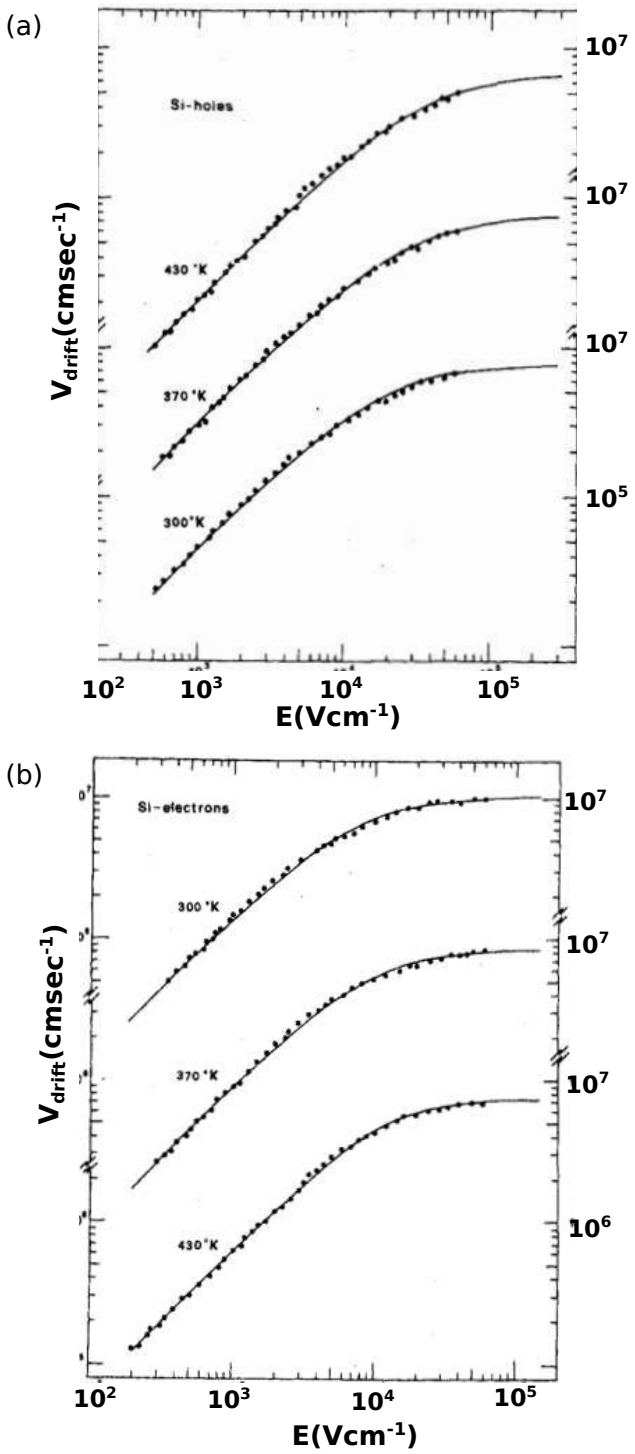

Figure 2.12: Plots reproduced from [19] of (a) Si hole drift velocity and (b) Si electron drift velocity. Plots are as function of Electric field for three different temperatures. It is shown that the drift velocity is saturated at $\sim 10^7$cm/s.

the conduction band, as depicted in Figure 2.13. The conduction band will therefore be dominated by donor electrons such that the electron density (n) is:

$$n \cong N_D. \tag{2.15}$$

An example of a p-type semiconductor is boron doped silicon. In this situation due to a partially filled covalent bond, a hole is created similar to the one left behind when a electron is promoted to the conduction band. However this hole has different characteristics, such that if an electron recombines with this hole, it is not as strongly bound as the rest of the valence electrons. This creates electron sites within the forbidden energy gap near the valence band as depicted in Figure 2.13. Thermal excitations that occur in the crystal are sufficient to ensure that electrons occupy the acceptor sites near the valence band. Due to the small energy gap between the acceptor level and the valence band, the electrons are promoted to the acceptor level and holes are created in the valence band. It is approximated that for every acceptor impurity atom added, an extra hole occurs in the valence band. Therefore, if N_A exceeds the intrinsic concentration of holes, the hole density (p) is represented as:

$$p \cong N_A. \tag{2.16}$$

P-N Junction

A p-n junction is created at an interface of a n- and p-type semiconductor material that is in contact under thermal equilibrium. The p-n junction is the component which allows semiconductors to be used as radiation detectors. Sophisticated techniques are used to create p-n junctions such as diffusing p-type impurities onto a homogeneous bar of n-type material, so that a p-type semiconductor is created at that region. The n-type side of the junction is dominated by electrons with only a few holes with the opposite being true for the p-type material. At the boundary between the materials, the large carrier gradient results in carrier diffusion of holes from the p-side towards the n-type material. This causes a negative space charge to form on the p-

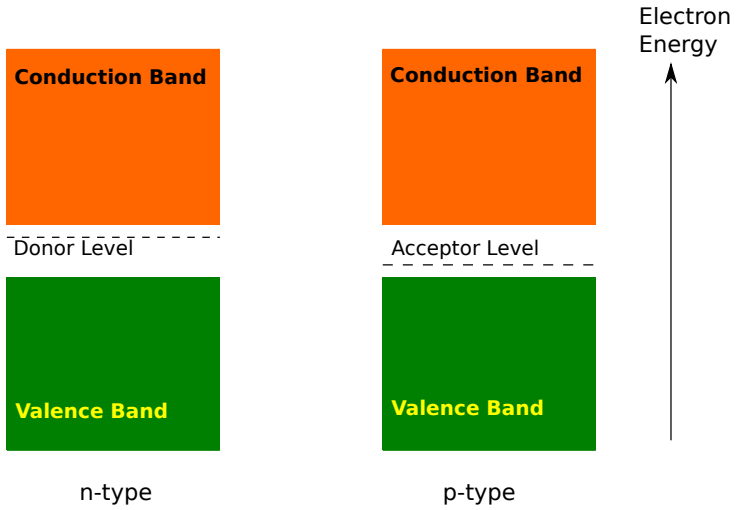

Figure 2.13: Schematic diagram of the band structure in n- and p-type semiconductors.

side of the junction as negative acceptor ions (N_A^-) are left uncompensated. Simultaneously, the diffusion of the electrons from the n-side subsequently cause a positive space charge near the p-side due to the uncompensated positive donor ions (N_D^+). This region of space charge that is created is known as the depletion layer. Figure 2.14 is a schematic illustration of a p-n junction showing the depletion layer. At thermal equilibrium, the electrostatic potential difference between the p- and n-side is called the built in potential difference (V_{bi}) and is given by [17]:

$$V_{bi} = \frac{kT}{q} ln\left(\frac{N_A N_D}{n_i^2}\right) \tag{2.17}$$

where k is the Boltzmann constant, T is temperature (Kelvin), q is the charge of an electron and n_i is the intrinsic charge carrier density. The built in potential difference gives rise to an electric field across the junction. Within the depletion region, an electric field is induced which is directed from the positive charge to the negative charge such that the electric field opposes the diffusion of holes and electrons.

The depletion layer forms the premise of semiconductors being used as radiation detectors. A gamma-ray interaction in this region creates electron

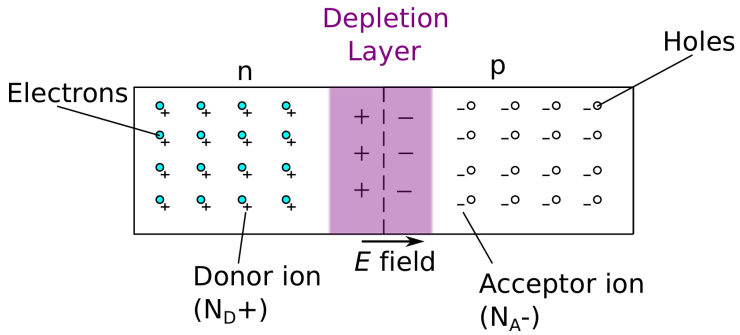

Figure 2.14: Schematic diagram of a p-n junction, demonstrating the build up of space charge at the boundary between the p- and n-type material, where the charges of the fixed dopant ions are shown in the depleion layer.

hole pairs that will be swept out of the depletion layer by the electric field. Electrical contacts can be placed on either side of the junction to collect the charge carriers and to generate a current proportional to the ionisation that has taken place. The small intrinsic electric field means the ions created can easily be trapped or recombined, which would lead to poor signal strength. One way to increase the electric field and depletion layer is to apply a reverse bias.

Reverse Biasing of the P-N Junction

The consequence of applying a reverse bias to the p-n junction is to increase the depletion layer thickness and charge collection efficiency. The reverse bias is applied via a negative voltage to the p-side or a positive bias to the n-side. This causes the holes in the p-type region to be attracted towards the p-type electrical contact and also the electrons in the n-type region to be displaced towards the n-type electrical contact. Under a reverse bias (V_B) the width of the depletion layer (W_D) for a one sided abrupt junction can be calculated from [17]:

$$W_D = \sqrt{\frac{2\varepsilon_s(V_{bi} - V_B)}{qN_B}} \tag{2.18}$$

where ε_s is the semiconductor dielectric constant, q is the charge of an electron, and N_B is the dopant concentration of the more lightly doped region

[17]. Increasing the reverse bias, increases the depletion layer thickness further. However there is a critical breakdown voltage where the junction will start conducting a large current due to the resistance of the semiconductor.

ProSPECTus Detector Geometry

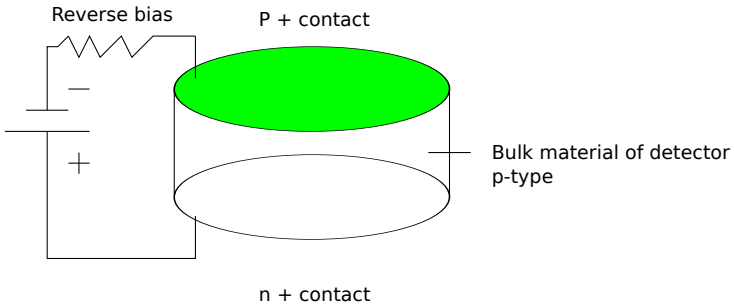

Figure 2.15: Schematic representation of a Ge planar detector.

The Ge and Si detectors used in this project are all of a planar geometry. Ge detectors are also available in a coaxial configuration, this type of geometry is explained in [9]. On a planar detector, electrical contacts are used to collect charge carriers and generate signals. In Ge, these electric contacts are assigned to the flat sides of a Ge disk as shown in Figure 2.15. The Ge detectors used in this project have a bulk material made out of p-type material. The contact on one face of the bulk is of n-type material and is formed by either lithium evaporation or by direct ion implantation. On the opposing face a p-type contact is used, which is produced by boron implantation. In order to deplete the whole detector a reverse bias is used, so that a positive voltage is applied to the n+ contact with respect to the p+ surface. The depletion layer originates from the p-n junction interface and extends into the bulk of the detector as the voltage is increased, until the full bulk is depleted. The reverse bias is increased past this point to ensure:

- The electric field throughout the detector is increased by a uniform amount.
- The minimum electric field is sufficient for saturated drift velocities of

the charge carriers. This reduces the collection time, charge recombination and trapping probabilities.

When using Si and Ge as bulk detector materials with standard semiconductor impurities, a depletion depth of approximately 2-3 mm is achievable. For gamma ray spectroscopy and the work in this project, detectors with greater thicknesses are required. Reducing the impurity concentration is one way of enlarging the depletion depth. The impurity level of a semiconductor material can be reduced by either refining techniques or through lithium ion drifting. Refining techniques for Ge have been developed that can fabricate Ge with impurity concentrations of $\sim 10^{10}$ atoms/cm^3 [20]. This allows bulk Ge material to be made with depths of several centimeters. Ge materials created with this method are known as High Purity germanium detectors (HPGe). The Si detector used in this work has been fabricated using lithium drifting processes [21] to achieve a suitably thick detector, Lithium drifted silicon is denoted as Si(Li).

In order to achieve two dimensional position information of the interactions in the detector, the detectors can be segmented with several electrical contacts on either side. The detectors used in this thesis have segmented contact strips, these are oriented orthogonal to each other, at each face. Section 3.5.3 explains how these strips are used to provide position information, in a Compton camera set up. Figure 2.16 is a schematic drawing of how the detector faces are labeled as either AC or DC, this refers to the type of capacitive coupling that occurs between the contact strips and the preamplifier. AC coupling is used for the strips that the high voltage is applied to, this ensures that the preamplifier is isolated from direct leakage current. The polarity of the applied voltage dictates which charge carrier is collected at each face, Figure 2.16 represents the configuration for the detectors used in this project. Section 4.1 explains the specific detector geometries and dimensions used in this project.

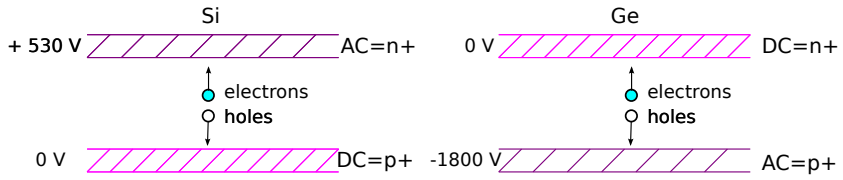

Figure 2.16: Schematic drawing of the Si(Li) and HPGe planar detectors, detailing the reverse bias voltage and the relative charge carrier collection, at the AC and DC electrical contact strips.

Signal Generation

The interaction of a gamma ray in a semiconductor material creates electron-holes pairs as described in Section 2.3.2. The electrons and holes are free charge q that move under the influence of the electric field in the detector bulk material. The trajectory of charge q induces a charge Q on the electrodes. The signal generated on the electrode starts to form as soon as the charge carriers begin to move towards their collecting electrode, continuing until once all charge carriers are collected at the electrode. The Shockley-Ramo Theorem [22] can be used to determine the amount of induced charge on the electrode due to the movement of the charge carriers. According to the theorem, the current generated at a particular electrode is given by

$$i = q\vec{v}.\vec{E}_0(\mathbf{x}) \tag{2.19}$$

where $\vec{v}$ is the velocity of the charge carrier and $\vec{E}_0$ denotes the weighting field. The total induced charge on the electrode can also be expressed in terms of the weighting potential $\Delta\phi_0$. The sum of the charge on the carrier multiplied by the difference in the weighting potential from the beginning to the end of the carrier path is shown in Equation 2.20.

$$Q = -\phi_0(\mathbf{x}) \tag{2.20}$$

The Laplace equation for the geometry of the detector must be solved in order to deduce the weighting potential as a function of charge carrier position. Certain conditions must also be assumed:

- The collecting electrode is set at unit potential.

- All other electrodes are at ground potential.
- No other charge is present i.e. trapped charges.

The weighting potential is different to the electric potential and is used as a convenience that enables a simplistic approach in determining the induced charge on the electrode by using the difference between the weighting potential at the start and end of the carrier path. The weighting field is defined as the gradient of the weighting potential.

The detectors used in this project are electronically segmented to provide position of interaction information as described in Section 3.5.3. Application of the Shockley-Ramo theorem can be utilised to improve the precision of position information beyond the limits defined by this segmentation. Figure 2.17a reproduced from [9] is a planar detector with a multiple electrode surface defined as pixels on the right and a continuous cathode on the x-y surface at the left. If an interaction occurs at point C the electrons created will have a trajectory that follows the electric field lines that are along the detector depth or Z=0 to Z= T and are subsequently collected at pixel 2. However signals are also induced on pixel 1, these signals are called image charges. Images charges are defined as the charge that is induced on the neighbouring strips, due to the movement of charge carriers .The weighting potential for pixel 1 is zero at the start of the charge carrier path and at the end, therefore no net charge is produced on pixel 1 when the electrons are collected at pixel 2. However as shown in Figure 2.17B) The electrons pass through a region where the weighting potential rises to a maximum before falling to zero. The size of this induced current is sensitive to the position of interaction. Therefore studying the signals from all electrodes near the collecting electrode can provide improved position information in the lateral dimension i.e X and Y.

Preamplifiers

A preamplifier is the first element used to process the charge signal produced by the detector and is used to amplify this signal, in order to make it suitable for further processing. The preamplifier should be located as close to

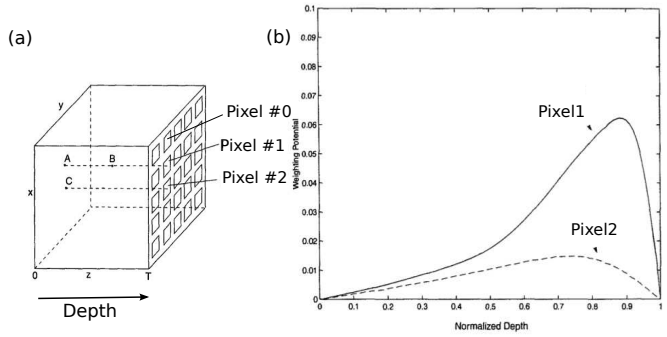

Figure 2.17: Schematic of (a) a planar detector with a continuous electrode on the x-y surface and multiple electrodes on the right surface at z=t (b) Weighting potentials occurs on pixel 1 and 0 when an interaction occurs at point C in (a). Reproduced from [9].

the detector as possible in order to maintain a good signal to noise ratio. Semiconductor detectors require the use of fast charge sensitive type preamplifiers, in order to preserve the proportionality of the output voltage pulse to the charge Q created by the incident radiation (see Section 2.3.2). Figure 2.18 is a schematic illustration of the main components in a resistive feedback charge sensitive amplifier. The charge from the detector is extracted by the capacitor (C_i). The charge pulse is integrated onto the capacitor (C_f) and discharged via a feedback resistor (R_f). This gives rise to the preamplifier's output voltage pulse (V_{out}) exhibiting an exponential decay time and fast rise time. The rise time is dependent on the charge collection time and the decay tail of the signal is determined by the time constant R_fC_f. As long as the time constant is longer than the duration of the collection time, the output voltage pulse has a magnitude that is proportional to the energy deposited within the detector. Figure 2.19 is an example of a preamplifier signal acquired from an silicon detector with 511 keV incident gamma rays from a ^{22}Na point source.

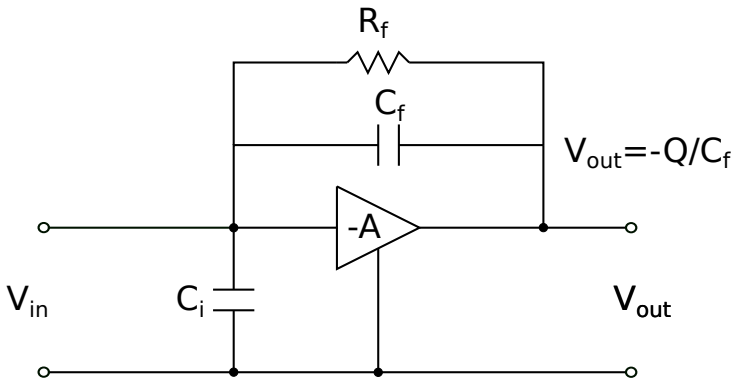

Figure 2.18: A simplified schematic diagram of a resistive feedback charge sensitive preamplifier.

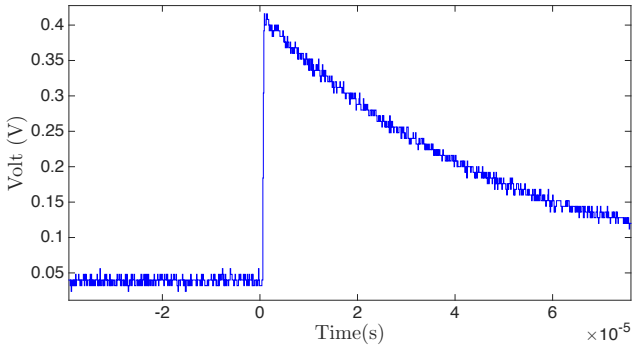

Figure 2.19: Charge sensitive preamplifier pulse acquired from a silicon detector, irradiated by a 511 keV incident gamma ray from a ^{22}Na point source.

2.3.3 Detector Performance

Energy Resolution

The precision with which a system can determine the energy deposited within a detector is known as the energy resolution. This is typically quantified through calculation of FWHM for photopeaks as a function of energy. There are three main components that cause fluctuations in the detector response and lead to an uncertainty in the amount of energy deposited. These are statistical noise, i.e the fluctuation of the number of charge carriers created per interaction, electronic noise, i.e noise that occurs due to electrical elements in the signal processing chain, and signal losses i.e incomplete charge collection and detector leakage current. The contribution to the FWHM of each of these factors add in quadrature to give the intrinsic energy resolution of a detector:

$$(FWHM)^2_{intrinsic} = (FWHM)^2_{statistical} + (FWHM)^2_{electronic} + (FWHM)^2_{signal\ losses} \tag{2.21}$$

The statistical noise can be related to the number of charge carriers created, via the following formula:

$$(FWHM)^2_{statistical} = \frac{(2.35)^2 F}{N_{pair}}, \tag{2.22}$$

where N_{pair} is the number of charge carriers produced per interaction and F is the Fano factor. The Fano factor is a quantification of the deviation of the number of charged particles from pure Poisson statistics, defined as:

$$F = \frac{Observed\ variance\ in\ N_{pair}}{Poisson\ predicted\ variance\ of\ N_{pair}} \tag{2.23}$$

The statistical noise provides the fundamental limit in the energy resolution, as no matter how much the other components are improved, the statistical fluctuations will always be present and cannot be decreased.

Efficiency

Efficiency is a measure of the effective detection of incoming gamma rays by a radiation sensor. Counting efficiency of a detector can be described in terms of either the intrinsic efficiency (ϵ_{int}) or absolute efficiency(ϵ_{abs}). The absolute efficiency can be calculated from:

$$\epsilon_{abs} = \frac{\text{number of signals recorded}}{\text{number of radiation quanta emitted}}, \tag{2.24}$$

The detector properties and the source to detector geometry during data acquisition, contributes to the absolute efficiency. These effects are removed through quoting the intrinsic efficiency, which is defined as:

$$\epsilon_{int} = \frac{\text{number of signals recorded}}{\text{number of radiation quanta incident on detector}}. \tag{2.25}$$

Knowledge of the efficiency of a particular detector is therefore essential in order to calculate the number of incident gamma rays from a measure of the number of signals created by the detector.

Chapter 3

Principles of Gamma Ray Imaging

3.1 Imaging In Nuclear Medicine

Medical imaging is an important tool used by healthcare professionals for diagnostics, treatment planning and the tracking of diseases. Medical images can be classified by the type of information they present, i.e anatomical or physiological. Anatomical images show the structure and location of bones and organs within a patient and the modalities used to produce these types of images include X-ray, Computed Tomography (CT) [3] and Magnetic Resonance Imaging (MRI) [4]. Images that characterise physiological processes (metabolic processes, blood flow and organ function) are called functional images. Positron Emission Tomography (PET), Single Photon Emission Computed Tomography (SPECT) and Functional MRI (FMRI) systems are used in clinical practice to produce such images.

The detector system developed in this thesis has been designed for use in nuclear medicine, which involves the use of biological compounds labeled with radionuclides, known as radio-pharmaceuticals. These compounds can be used for diagnostic and therapeutic purposes, although only diagnostic functional imaging will be considered in this thesis. The two main diagnostic techniques used in nuclear medicine are SPECT and PET, which rely on

gamma and β^+ emitting radionuclides, respectively. The methodology of a nuclear medicine imaging study is as follows:

1. Delivery of a gamma ray or positron emitting radio-pharmaceutical to a patient, which accumulates in a region of interest.

2. Gamma rays emitted from within the patient are detected by external radiation detectors.

3. Data is reconstructed to produce a radiation distribution image.

The work in this thesis is based on a project which aims to overcome the limitations of SPECT systems and therefore the principles of SPECT imaging is described in the next section. For a detailed description of PET imaging the reader is referred to [1].

3.2 Principles of Single Photon Emission Computed Tomography

SPECT systems employ single or multiple rotating gamma cameras to detect gamma rays incident from within the patient. A planar (2D) image can be produced by acquiring data of the radionuclide distribution at one angle. This provides little depth information but is useful for instances where there is not much radio-pharmaceutical uptake, for example, in whole body bone studies, thyroid studies and ventilation/perfusion studies [23]. It is more typical for SPECT to use tomographic imaging, in which the detectors acquire 2D planar images from several projections (angular views) around the object of interest, enabling cross sectional images of the distribution to be reconstructed. The data can then be viewed as a 3D distribution, representing the radioactive volume within the patient. Tomographic imaging offers the advantage of offering more precise activity quantification compared with 2D planar imaging techniques, at defined locations within the image. This allows tracer kinetic studies to be performed which allow quantitative

Figure 3.1: An image of the Infina Hawkeye dual headed SPECT system located in the Medical Teaching and Research Laboratory (MTRL) STFC Daresbury.

measurements of physiological processes, biochemical rates or specific biological events [24] [1]. A sufficient amount of tomographic imaging data can be acquired over an arc of 180°, however acquiring data over a full 360° offers advantages in resolution, uniformity and in more accurately determining gamma ray attenuation [1]. Dual or multiple headed systems offer faster data acquisition times than single gamma camera systems. A dual headed system with the detectors mounted at 90° to each other can image over 180° in half the time of a single headed detector system [24]. An example of a dual head system is shown in Figure 3.1. The image shows an Infinia Hawkeye Dual headed SPECT system, which is located in the Medical Teaching and Research Laboratory (MTRL) at STFC Daresbury Laboratory. This system was previously used in a clinical setting at Leeds General Hospital and Figure 3.2 shows an anonymised image produced by the system for a parathyroid study [25]. The geometrical setup of a SPECT system is determined by the clinical study. SPECT is commonly used to image modern cerebral blood flow agents and is often the chosen imaging modality for myocardial perfusion imaging [2] and cardiac studies, which has led to the development of specifically designed compact cardiac SPECT systems [26] [1].

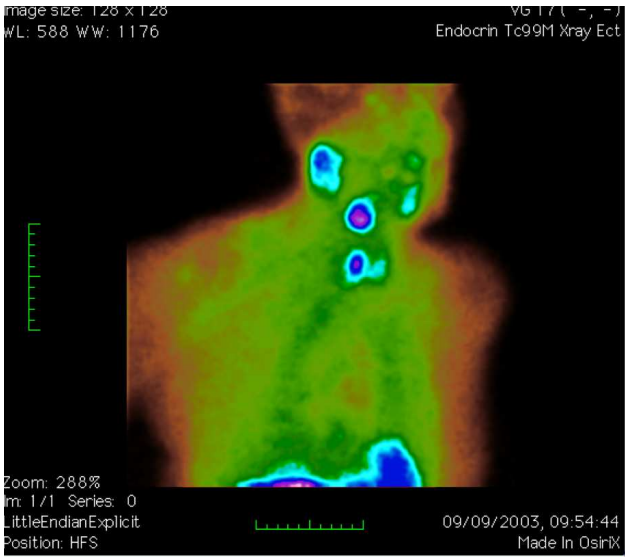

Figure 3.2: Medical functional image of a parathyroid study [25], generated by the Ge Infinia Hawkeye dual headed SPECT system when used in Leeds General Hospital.

Radionuclides used for SPECT Imaging

SPECT uses radionuclides that emit either single gamma rays or multiple gamma rays that have no angular correlation. These radionuclides are bound to specifically chosen biological compounds that will accumulate in a region of interest inside the patient. Radionuclides for nuclear medicine are chosen for their appropriate half lives and energy of the emitted gamma rays. The half life of the radionuclide needs to be long enough to accumulate in the patient and conduct the diagnostic study but not too long that the patient is exposed to unnecessary radiation after completion of the scan. The gamma-rays need to have sufficient energy enough to pass through the patient without attenuation but be low enough to be efficiently stopped in the detection medium.

Table 3.1 displays the most commonly used radionuclides in SPECT, with their corresponding gamma ray energies, half lives and common diagnostic applications. Of these radionuclides, ^{99m}Tc is the most commonly used in nuclear medicine and is used in 80% of the 25 million radio-biological medical imaging scans that occur each year [28]. In particular, almost all cardiol-

Radionuclide	Half life (hours)	Energy (keV)	Uses in SPECT imaging
^{123}I	13.2	159	Kidney function,
^{131}I	193	364	Thyroid imaging for diagnostics
^{67}Ga	78.2	0.93, 184, 300	Infection, lymphoma detection
^{111}In	67.2	173, 247	Infection
^{67}Cu	62.4	185, 92	Tumor imaging, Prostrate probing
^{99m}Tc	6.01	141	Cancer, liver function, blood flow

Table 3.1: Attributes and uses of the most commonly used radionuclides in Single Photo Emission Computed Tomography [23] [27].

ogy studies in nuclear medicine use ^{99m}Tc, which is a significant part of all diagnostic investigations [29]. ^{99m}Tc is widely employed for several reasons:

- The single gamma ray emission of 141 keV has adequate tissue penetration (50% absorption in 4.6 cm of tissue) [30].
- The 141 keV gamma ray energy is low enough to be collimated by lead, tungsten or other heavy metal collimators.
- The half-life of 6.01 hours is ideal for an imaging study.
- The cost effectiveness and ability to locally extract ^{99m}Tc through a ^{99}Mo/^{99m}Tc generator system within the hospital.
- The complex chemistry of ^{99m}Tc allows the radioisotope to be incorporated into a large range of ligands that stabilise the radionuclides at different oxidation states [31].
- Hundreds of radio-pharmaceuticals labeled with ^{99m}Tc have been developed.

3.2.1 The Fundamental Components of a Gamma Camera

Commercially available SPECT systems rely on the use of a gamma camera [1] to produce planar and 3D images. The main components of a gamma camera are shown in Figure 3.3, these are: a collimator, scintillator crystal and PMT's. The components are usually housed in a single unit referred to

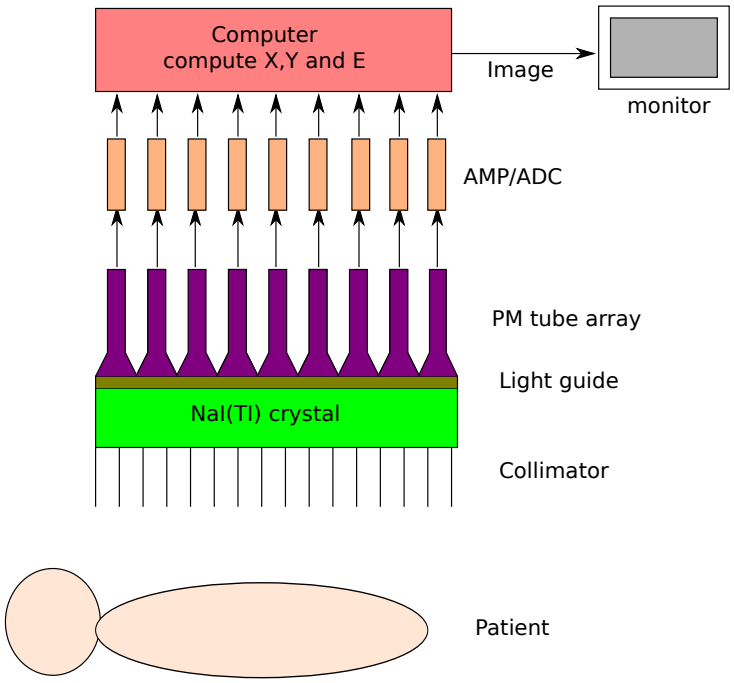

Figure 3.3: Schematic diagram of the main components of a gamma camera.

as the detector head. The detector head is mounted on a stand that can be moved via electrical switches horizontally, vertically or in a rotational motion. The head usually rotates in 3° to 10° increments around the patient when acquiring tomographic data [24].

Collimator

Gamma rays are emitted isotropically from the radiation distribution within the patient. Therefore, in order to define the relationship between the position of interaction in a detector and that from which they were emitted, an absorptive collimator is attached to the face of the scintillator detector array. An ideal collimator only permits gamma rays traveling along certain directions to reach the detector, as they are otherwise attenuated in the collimator septa, the material between the holes. The most commonly used in SPECT is a parallel-hole collimator [2], an example of which is shown in Figure 3.4 [1]. The collimator is essentially a heavy metal plate that is typically made out of tungsten or lead with an array of holes whose axes are perpendicular

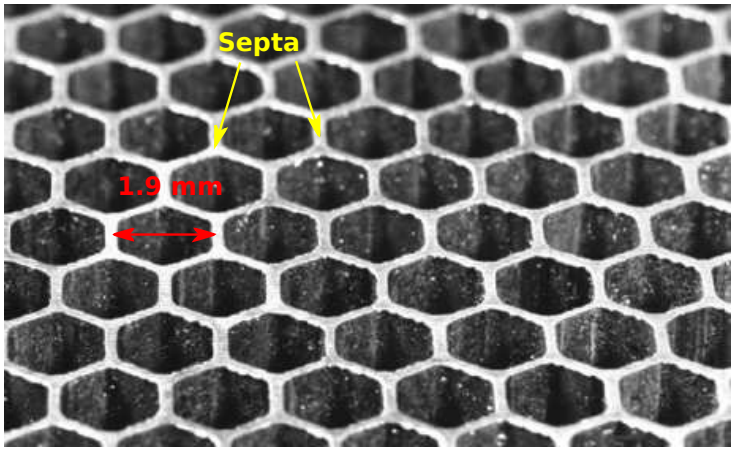

Figure 3.4: A magnified view of a typical parallel-hole collimator. Reproduced from [1].

to the face of the detector and parallel to each other. The maximum width of the individual hexagonal holes in this example collimator are $\sim$ 1.9 mm.

Parallel-hole collimators transmit gamma rays that are perpendicular to the crystal, therefore they project the image directly onto the detector without magnification or reduction. There are several other types of collimator, one method of classification is on the type of focusing the collimator provides. The other types of focusing collimators are: diverging collimator (used to image larger organs such as the liver and lungs with a wider field of view), pinhole collimator (used to image small organs such as the thyroid and heart) and converging collimator (used to image small organs with large area detectors). Figure 3.5 shows schematic illustrations of the different field of views for these types of collimators.

Collimators are the limiting component of the gamma camera as they greatly influence the sensitivity of the system. The collimator efficiency is so low that approximately only 1 in 10,000 gamma rays are typically transmitted to the scintillator, the majority being attenuated by the septa. Collimator efficiency is defined as the number of gamma rays that are able to pass through the collimator and reach the detector in order to contribute to the gamma ray image, i.e. the transmission. The efficiency can be optimised by varying the collimator hole diameter (d), hole number (N) and septa

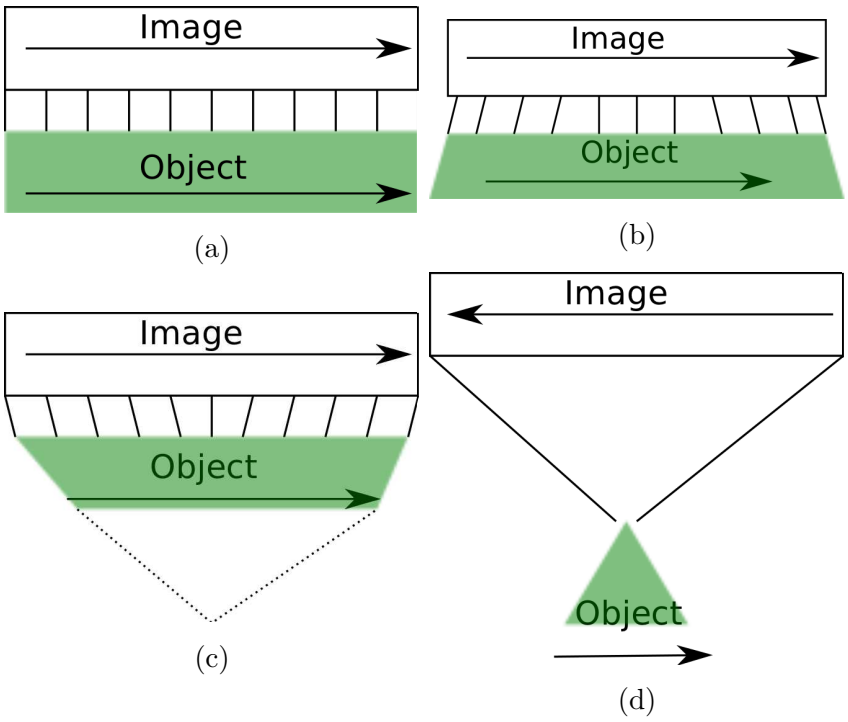

Figure 3.5: Schematic illustrations of the collimator types used in SPECT: (a) parallel-hole, (b) diverging, (c) converging and (d) pin-hole collimators. The shaded region represents the field of view [2].

thickness (t). The collimator efficiency (E_{coll}) can be calculated using the equation [1]:

$$E_{coll} \approx K^2 \left(\frac{d}{I_{eff}}\right)^2 \left[\frac{d^2}{(d+t)^2}\right], \tag{3.1}$$

where the constant K is determined by the hole shape and I_{eff} is the effective length of the collimator hole, which is defined as $l - 2\mu^{-1}$ where l is the hole length and μ^{-1} is the linear attenuation coefficient of the collimator material [1].

The collimator resolution (R_{coll}) i.e. the sharpness of the image projected onto the detector, is often worse than the resolution of the detector and associated electronics as it also depends on d, N and t. The collimator efficiency and spatial resolution can be related by the approximation:

$$E_{coll} \propto (R_{coll})^2. \tag{3.2}$$

Therefore, an improvement in efficiency leads to a degradation in image resolution and vice versa. To compensate for this inherent design compromise, many types of collimators exist such as those in Figure 3.5 and the design of each is chosen depending on the radionuclude used in the particular clinical study. The four main types of parallel-hole collimators are [1]:

- Low Energy All Purpose (LEAP) / Low Energy General Purpose (LEGP) collimator.
- Low Energy High Resolution (LEHR) collimator.
- Low Energy High Sensitivity (LEHS) collimator.
- Medium and High Energy (ME and HE) collimators.

Table 3.2 shows the typical characteristic properties of these collimator types, determined for a gamma-ray source with maximum energy (E_{max}), placed at a distance of 10 cm from the collimator. In clinical practice, the collimator is chosen depending on the energy of the radionuclide used, details of which were discussed in the previous section. ^{99m}Tc and ^{123}I radioisotopes are normally used with low energy collimators but can also be used with ME collimators, however this leads to a degradation in efficiency due to the increased thickness of the septa. The ME and HE collimators are typically selected for measuring the radiation distributions from ^{111}In and ^{131}I, respectively. Clinical departments are normally equipped with a variety of collimators and the most appropriate is chosen by the medical physics team for a particular study [32].

Scintillator Crystal

An essential component of the gamma camera is the scintillator crystal used to detect the gamma-rays that have been transmitted through the collimator. Thallium doped Sodium Iodide (NaI(Tl)) is the most commonly used

Collimator	E_{max} (keV)	d (mm)	t (mm)	N	g (%)	R_{coll} (mm)
Low Energy, High Resolution	150	1.8	0.3	30000	1.84 x 10^{-4}	7.4
Low Energy, General Purpose	150	2.5	0.3	18000	2.68 x 10^{-4}	9.1
Low Energy, High Sensitivity	150	3.4	0.3	9000	5.74 x 10^{-4}	13.2
Medium Energy, High Sensitivity	400	3.4	1.4	6000	1.72 x 10^{-4}	13.4

Table 3.2: The properties of the different types of parallel hole collimator available for use with a 400 mm diameter gamma camera. Details are provided about the typical septa thickness (t), hole diameter (d), Number of holes (N), efficiency (g), maximum energy (E_{max}) and spatial resolution (R_{coll}). Details reproduced from [1] [32].

scintillator crystal in SPECT gamma cameras. The operation of a scintillator detector and key properties of (NaI(Tl)) were previously described in Section 2.3.1. Most modern cameras have a rectangular shaped detector with dimensions 45 x 60 cm, which gives a practical field of view of 40 x 55 cm [24]. The thickness of the scintillator crystal influences the efficiency of detecting gamma-rays that traverse the collimator. The attenuation length for 141 keV gamma rays in Na(Tl) is 4 mm, therefore the crystal thickness in SPECT systems, range from 9 mm to 12 mm [33]. For 141 keV gamma rays there is a difference of 20% in photopeak detection efficiency for a change of Na(Tl) crystal thickness from 6.4 mm to 12.7 mm [1], which improves the quality of the image. However, an increase in crystal thickness results in a degradation of the intrinsic resolution (FWHM, mm).

NaI(Tl) detectors suffer from poor energy resolution of ∼10-12 % at 141 keV, which prevents simultaneous data acquisition with ^{99m}Tc and ^{123}I isotopes. Simultaneous measurements are desired in order to conduct different investigations but with the same geometrical environment and physiological condition with the benefit of improving patient throughput and comfort [8]. In particular dual tracer studies with ^{99m}Tc and ^{123}I are desired in parathyroid imaging, in order to diagnose a parathyroid adenoma, that when conducted with a single ^{99m}Tc tracer can lead to 20-25 % patients being undiagnosed [34]. At the start of a clinical study, an energy window is specified,

which requires two values: a window median value and a window range specified as a percentage. For a median energy of 141 keV and a 20% (28 keV) window, this results in a range of accepted energies of 126-154 keV. The close energies of ^{123}I and ^{99m}Tc results in an effect known as cross talk, which is when scattered and primary photons from one radionuclide impede the other radionuclide's primary photopeak energy window. Complex peak deconvolution techniques can be employed to resolve close lying energy gamma ray peaks, which rely on the implementation of multiple varying energy windows and cross talk reductions [8]. The energy resolution of a Na(Tl) scintillator crystal also means it is challenging to discriminate gamma rays that have Compton scattered within the patient or collimator. Typically ∼20-50% of all gamma rays detected by the gamma camera have undergone Compton scattering. This gives rise to the mispositioning of gamma rays in the planar image, which manifests in the SPECT image as increased background and hence reduced contrast. Therefore, scatter correction methods are essential in quantitative SPECT studies, which have led to the dominant use of SPECT/CT systems due to the attenuation maps provided by CT. In addition, there have been developments in using high resolution solid state detector systems rather than the scintillator based gamma camera. These systems usually consist of multiple small detectors such as Cadmium zinc telluride (CZT) with pinhole collimator configuration and are normally tailored for specific applications such as cardiac imaging [35] because of cost implications. These systems also benefit from improved energy resolution to that of Na(Tl) and improved sensitivity due to a large number of detectors for a small field of view [36] .

Photo Multiplier Tubes

A PMT array is used to produce electrical signals proportional to the scintillation photons produced from the NaI(Tl) crystal, as described in section 2.3.1. The output signals of the PMTs are used to define the X, Y coordinates of the gamma ray interaction position in the detector via a X-Y positioning circuit. The positioning circuit provides the X-Y co-ordinate of individual

scintillation events through a weighted average of the PMT signals, as they are generated. A greater number of PMTs leads to an increased accuracy of the X, Y coordinate determination and hence the spatial resolution. In modern gamma cameras manufacturers utilise 59 PMTs [24].

The operational interference caused by magnetic fields to PMT's prevents co-registry with MRI scanners. This arises as the electron paths are influenced by the magnetic fields and manefests in the output as poor spectral quality. However, it is desirable to operate SPECT and MRI simultaneously as it would produce images with both functional and anatomical details but with a lower radiation dose than SPECT/CT. To overcome the limitation arising from traditional PMTs, advancements have been made using SiPMs, avalanche photodiodes and Silcon Drift Detectors (SSDs) in SPECT systems in order to enable the simultaneous acquisition of MRI and SPECT images [37] [38]. Alternatively, solid-state semiconductor detectors can be used that directly convert the gamma-ray energy to electrical signals, without the use of a PMT.

Data Storage and Image Reconstruction

The signals generated from the PMT's have a small amplitude, therefore these are amplified first by preamplifiers and then linear amplifiers. The amplified pulses are typically stored in a matrix of either 64 x 64 or 128 x 128, for each angular position that the gamma camera collected data at. Images can be generated from the stored data for transverse (short axis), saggittal (vertical long axis) and coronal views (horizontal long axis). The data at each projection angle provides 2D planar images. The projections can be used to provide tomographic images with depth information. The images are commonly reconstructed using algorithms such as the Filter Backprojection method which is described in [39]. Filter Back Projection (FBP) methods can lead to artifacts in the image which can lead to false positives in Myocardial perfusion imaging [40], therefore iterative reconstruction algorithms can be used, which reduce these artifacts. Iterative algorithms are more computationally intensive than FBP algorithms but have the advantage of

providing quantitatively more accurate reconstructions [1].

3.2.2 Limitations of Conventional SPECT Systems

The use of a gamma camera and the components described in the previous section induces certain limitations, these can be summarised as:

- A compromise between efficiency and image resolution.
- Limited efficiency and field of view.
- Poor energy resolution.
- Magnetic incompatibility.

To overcome the limitations of conventional SPECT system a Compton camera can be used as a replacement for the gamma camera.

3.3 Principles of Compton Imaging

Compton imaging is an established technique that has been used since the 1960's, it's application at the time residing in astronomy. The electronic collimation used in Compton cameras and the ability to receive multi-directional emission from radioactive substance, leads to large gains in sensitivity, which has led to the development of Compton camera techniques in sectors such homeland security [41] and environmental studies [42]. It was in the 1970's that the technique was first recommended to be used in nuclear medicine [43]. The prototype was based on an array of Schottky silicon barrier arrays but this was not realised due to limitations concerning electronics and computer resources. However, currently within nuclear medicine, Compton cameras have been designed and investigated to be used for both SPECT and PET imaging, in order to achieve optimum spatial resolution and enable MRI co-registry [44] [45].

Compton camera systems can consist of a variety of detector types and configurations, with the purpose of determining the energy and direction of

an incident gamma-ray. A conventional Compton camera consists of two detectors referred to as the scatter and absorber detectors, where the scatter detector is closest to the radiation source and whose function is to provide a platform for Compton scattering to occur. The absorber detector is required to fully absorb the Compton scattered gamma rays incident from the scatter detector. The Compton camera system used in this thesis compromises of two electronically segmented solid-state planar detectors, therefore the operation of this configuration will be explained in the subsequent section. However Compton camera's for the use in nuclear medicine have also been proposed to consist of: silicon scatter detectors coupled to uncollimated absorber scintillator detectors [46], a 4x4 planar array of HPGe crystals with a scintillator for SPECT [47] and pixelated CdTe detectors for a triple gamma coincidence Compton camera to be used with PET [44].

3.3.1 Operation of a Compton camera

The principle of Compton imaging is that an incident gamma ray undergoes Compton scattering in the scatter detector and is then fully absorbed via photoelectric absorption in the absorber detector. In an ideal situation, only one interaction occurs in both detectors. The work in this thesis only uses such interactions and these are denoted as single-single interactions. Other interaction combinations require more complicated event processing and can induce additional uncertainties thus degrading the final image. It is required that the energy deposited and location of each interaction in both detectors can be identified, so that the path of the incident gamma ray and the source location can be determined through event reconstruction. The Compton scattering formula in Equation 2.3 can be rearranged to identify the scattering angle θ of the gamma-ray in the first interaction as follows:

$$\cos\theta = 1 - \frac{E_1}{\frac{m_e c^2}{E_0}(E_0 - E_1)}, \tag{3.3}$$

where $m_e c^2$ represents the rest mass of electron and E_0 is the energy of the incident gamma ray, which is calculated as the sum of the energy deposited in

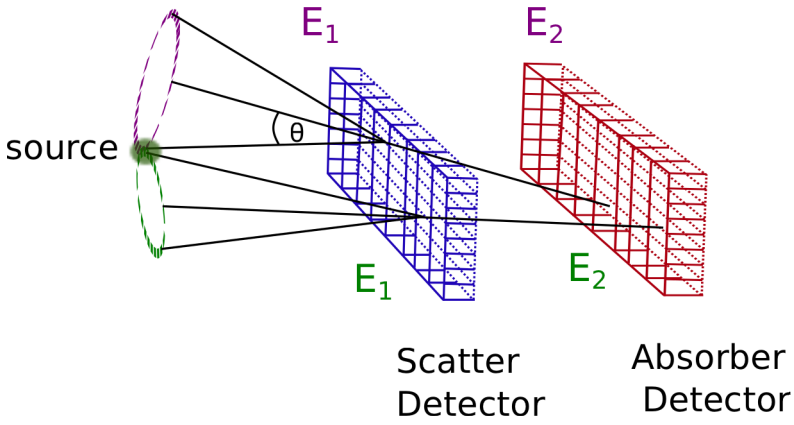

Figure 3.6: Schematic diagram of a Compton imaging system comprising of two planar detectors. Illustrated is two single-single events and their corresponding conics, the overlap of which indicates the location of the gamma-ray source.

the scatter E_1 and the absorber (E_2) detectors, as expressed in the following equation:

$$E_0 = E_1 + E_2. \tag{3.4}$$

In Compton imaging, 2θ is used to define the apex of a cone whose surface represents the possible locations of the gamma ray source. The interaction positions from each detector is used to determine the cone axis via the vector difference. As the number of events increase, the cone surfaces overlap and reveal the source location at the point of maximum intersection. This concept is schematically represented in Figure 3.6, where two single-single events and the associated cones can be seen to overlap at the point where the radiation source is located.

3.4 The Next Generation ProSPECTus Compton Camera

The ProSPECTus Compton camera system has been designed with the recommendations from previous work at the University of Liverpool [48] and

Figure 3.7: Photograph of the ProSPECTus aluminum cryostat. Shown in gold are the individual preamplifier signal connection points of each strip for both detectors.

developed in collaboration with the Royal Liverpool University Hospital and STFC Daresbury laboratory. The system consists of two planar electronically segmented semiconductor detectors housed in a single aluminium cryostat. A photograph of the cryostat in Figure 3.7 shows the individual preamplifier connectors for each strip of both detectors to interface the system to a digital acquisition system. The ProSPECTus cryostat has been designed to be compatible with magnetic fields and the detector separation kept to a minimum in order to achieve maximum efficiency [48]. The detectors have a face to face separation of 10 mm and are centrally aligned within the cryostat.

The scatter detector is a square planar detector with dimensions (64x64x9) mm. The detector segmentation is achieved via orthogonally placed contact strips on the front and back face of the detector. Each strip is 4 mm wide, there is thus 16 strips on each face. The absorber detector is a square planar germanium detector and has dimensions of: (60x60x20) mm. There are 12 orthogonally placed contact strips on each face that are 5 mm wide and this

provides the detector segmentation. Vacuum and cryostat tests are underway at the STFC Daresbury lab, thus the system is currently unavailable for use in measurements. Therefore the work in this thesis is conducted with a demonstrator ProSPECTus system whose details and specifications can be found in Section 4.1.

3.4.1 Advantages of the Compton camera configuration for SPECT systems

The ProSPECTus Compton Camera was designed to overcome the limitations that occur in conventional SPECT systems. A summary of the advantages expected to be achieved with the ProSPECTus system is described below:

- The heavy metal collimators in SPECT imaging are not required in Compton imaging. This leads to an increased efficiency of detected gamma rays and wider field of view. Therefore, the dose initially administered to patients can potentially be reduced or quicker scans could be undertaken leading to a increased throughput of patients.

- The semiconductor detectors used for ProSPECTus are predicted to have an energy resolution between 1-2 keV at 141 keV, which is a significant improvement over scintillator detectors that have a energy resolution of 14-17 keV at 141 keV. The improved energy resolution ProSPECTus can provide will allow multisotope scans of ^{99m}Tc (141 keV) and ^{123}I (159 keV), a feat that is not possible with conventional SPECT systems without complex peak deconvolution algorithms. The work in this thesis is based on demonstrating the multi medical isotope imaging capabilities of the ProSPECTus system.

- The energy spectra attained from the ProSPECtus system is expected to have a low Compton background from scattered gamma rays. Due to the excellent energy resolution of the detectors, the Compton background underneath the photopeak will be very small therefore resulting

in a large peak to background ratio. This will provide images that have a lower noise contributions than that of SPECT systems.

- The detectors used in ProSEPCTus as well as the cryostat they are housed in can be operated in a magnetic field which enables co-registry with MRI scanners. Investigations into the performance of a coaxial HPGe detector in a magnetic field and the effect on the MRI images have been carried out previously by the ProSPECTus collaboration in [49] .

3.5 Inherent Detector Properties that Influence Image Quality

There are inherent physical properties of the detectors used in a Compton imaging system that have an effect on its performance, particularly on image quality. These factors are energy resolution, Doppler broadening and position resolution. The following subsection describes how these factors arise and contribute to image degradation.

3.5.1 Energy Resolution

It is important in Compton imaging to be able to accurately determine the amount of energy deposited by each gamma ray interaction in the detector system. Initially, the energies are summed together to identify if the event lies within a photopeak, corresponding to total absorption of the initial gamma ray energy. If the measurement of energy has large uncertainties, the summed photopeak width is degraded and the ability to distinguish gamma-rays of similar energy becomes impossible as well as resulting in challenges for distinguishing gamma-rays scattered outside the system. Measurement of energies is also essential in localising the source of radiation via Compton kinematics, as described in Section 3.3.1. Any uncertainty in energy will lead to an uncertainty in the calculation of the scattering angle θ and hence the source location.

3.5.2 Doppler Broadening

Doppler broadening arises because it is assumed that during a Compton scatter the gamma ray interacts with a free electron at rest, i.e the electron has zero momentum. This assumption allows Equation 3.3 to be used to define the relationship between the scattered energy and scattered angle. However, in reality the gamma rays interact with moving bound atomic electrons which therefore possess non-zero momentum.

Therefore for a non-zero momentum distribution of the electron there could arise large uncertainties in the calculation of the scattering angle because this phenomena manifests itself in the broadening of the energy peaks in the detector, independently of the intrinsic energy resolution of the detector. One way to limit the effects of Doppler broadening is to use a material with a low atomic number [50]. This also has the advantage of increasing the relative probability of a Compton scatter interaction occurring compared to that of the photoelectric effect. The low atomic number of 14 is one of the reasons that silicon is chosen as the scatter detector material in the ProSPECTus system.

3.5.3 Position Resolution

The intrinsic position resolution of both detectors in the ProSPECTus Compton camera is defined as the segmentation achieved through the electronic contact strips. The orthogonally placed strips create 3D virtual voxels. The dimensions of the voxel is the precision that the location of the interaction in each detector can be defined. For the scatter detector this is (4 x 4 x 9) mm and for the absorber (5 x 5 x 20) mm. As illustrated in Figure 3.6, the position of interaction in each detector defines the cone axis, therefore any uncertainty of the position of the interaction leads to an error in the direction of the cone axis and position of the cone surface representing where the source is located. These uncertainties for each reconstructed event will manifest in the Compton image as degradation in image resolution and increase in noise.

3.5.4 Performance of a Compton Camera System

This thesis evaluates the demonstrator ProSPECTus Compton camera in terms of its energy resolution, timing resolution, Compton imaging efficiency and image quality. How the final two metrics are evaluated are explained in the subsequent sections.

Efficiency

The intrinsic and absolute efficiency of individual detectors can be calculated using the methods described in Section 2.3.3. Calculation of the efficiency for a Compton camera is more complex as it depends on the evaluation of a particular configuration of detectors and can be calculated using events which fall into different categories, depending on the complexity of their interaction sequence. Regardless of the event types, it is always simplest to calculate the efficiency of reconstructible events with respect to the number of gamma-rays $N_{incident}$ incident on the front face of the scatter detector using the following calculation:

$$Efficiency = \frac{N_{reconstructable}}{N_{incident}} \tag{3.5}$$

where $N_{reconstructable}$ is defined for the particular event selection criteria conditions of the experiment. This will be investigated experimentally for different event types in Section 5.0.10.

Image Quality

The quality of diagnostic images produced in nuclear medicine is typically evaluated by measurement of image resolution, contrast and noise. To assess these performance criteria consistently, medical imaging modalities utilise phantoms. These measurements are routinely undertaken for Quality Assurance of SPECT systems. Commercially available phantoms are either too large or small for the field of view of the ProSPECTus prototype system, as they are designed for standard SPECT scanners or small animal imaging systems respectively. To overcome this a team at the University of Liverpool

designed and created a phantom to be specifically used with the ProSPECTus project. The design is based on a clinical Jaszczak SPECT phantom and consists of 12 vials, which are divided into four diameter sizes of: 10 mm, 11 mm, 12.4 mm and 16.4 mm, as shown in Figure 3.8a. Ultimately this is the image resolution range that the ProSPECTus system aims to provide. There are three vials for each diameter size which are all 50 mm in length. The vials have sealed caps so that they can be filled with radioactive aqueous solutions and placed in the holder which is made out of perspex. Figures 3.8b and 3.8c show a photograph and schematic illustration of the perspex holder respectively. In this thesis, vials populating the phantom have been used to quantify the image resolution, noise and the feasibility of multi-isotope imaging with ^{99m}Tc and ^{123}I. These investigations and results can be found in Chapter 5.

(a)

(b)

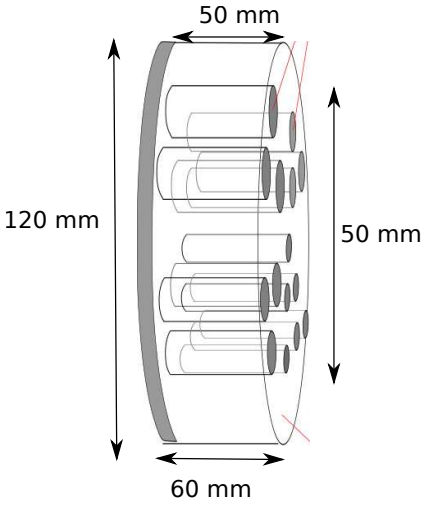

(c)

Figure 3.8: Photographs of (a) four vials with the sizes used in this thesis i.e diameters of 10 mm, 11 mm, 12.4 mm and 16.4 mm, (b) the holder and (c) a schematic drawing of the phantom holder.

Chapter 4

Optimisation of Experimental Set up and Parameters

The most commonly used radioisotope in medical imaging is ^{99m}Tc, which emits gamma rays with an energy of 141 keV [51]. Due to the short half-life of the isotope (6 hours), it is not practical to use in a development environment where repeated measurements are made over several months. Therefore, the radioisotope ^{139}Ce was chosen to optimise and acquire imaging data from ProSPECTus, due to its similar low gamma-ray energy of 166 keV and longer half life of 137 days. Compton imaging at the relatively low gamma ray energies typically used in SPECT is challenging. Therefore, an investigation was undertaken to establish the data acquisition parameters that would achieve the optimum efficiency and imaging performance from ProSPECTus, such as coincidence timing window and noise thresholds. All experimental work was undertaken with a demonstrator ProSPECTus system, using the setup and detectors described below. For the purpose of this thesis, the demonstrator system will be referred to herein as the ProSPECTus system. The specifications of the next generation ProSPECTus system can be found in Section 3.4.

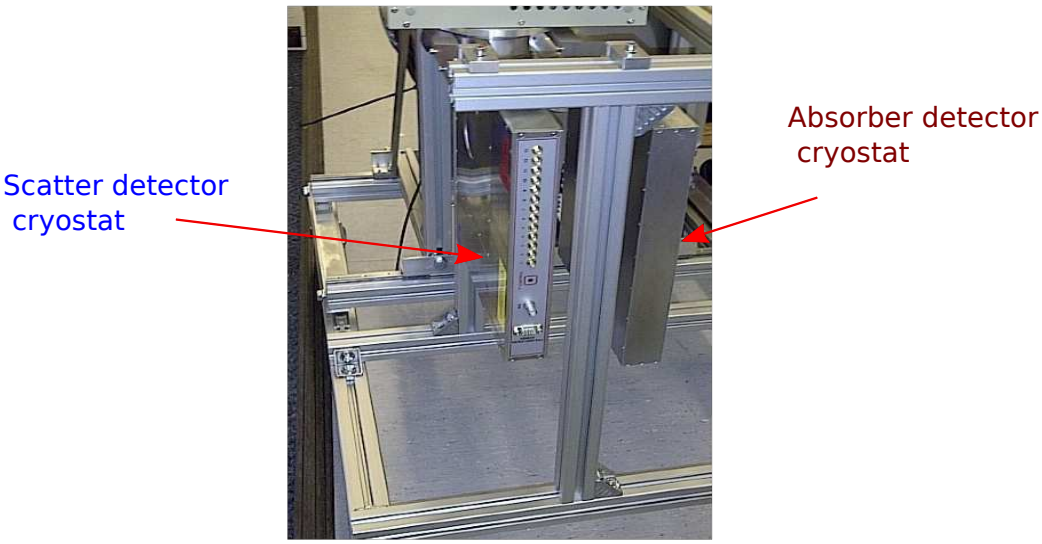

Figure 4.1: Photograph showing the detector cryostats placed within the custom made frame.

4.1 The ProSPECTus System

The ProSPECTus system consists of two segmented planar semiconductor detectors, housed in individual cryostats that are mounted in a custom designed aluminium frame. The frame was designed to allow the separation between the two detectors to be adjusted, thus the user can optimise system performance for efficiency or image resolution. Figure 4.1 shows a photograph of both cryostats within the frame. Two different HPGe absorber detectors were used in the experimental measurements of this thesis, (denoted absorber 1 and absorber 2). Absorber 1 is a ∼12 year old detector that was developed for the SmartPET project [52], which was primarily used for system setup, parameter optimisation and acquisition of preliminary data. However it was found that the noise prevalent in the absorber 1 detector prevented image charges being ascertained, which could be useful for offline processing techniques such as Pulse Shape Analysis (PSA) [53] [54]. Absorber 2 is a new detector with suitably low noise, which arrived at the University of Liverpool in time for the medical isotope measurements in this thesis, therefore this replaced absorber 1 for data acquisition with these isotopes.

4.1.1 Scatter Detector

The scatter detector is a Canberra manufactured, circular faced, planar Si(Li) detector. The Si(Li) is cryogenically cooled to a temperature of -175°C using a CryoPulse CP5 cooler as shown in Figure 4.2a. The Si(Li) detector is housed in an aluminium cryostat with dimensions of (35x35x5) cm, the detector crystal is placed centrally within cryostat depth, which leads to a spacing of 21 mm from the back and the front of the crystal to the cryostat. The depletion voltage of the Si(Li) detector is +150 V and the operating voltage used is +530 V. The positive polarity voltage is applied to the n-type (AC) side of the detector with the p-type (DC) side grounded. Therefore electrons are collected at the AC face and the holes at the DC face. A schematic of the Si(Li) detector is shown in Figure 4.3a. The detector has an active area of 3500 mm^2, with a diameter of 71 mm and thickness of 8 mm. A guard ring that is 5 mm wide surrounds the active area of the detector. There are 13 orthogonal contact strips on both AC and DC faces of the crystal. Each strip is 5 mm wide and separated by 500 μm, which provides a characteristic position resolution of (5x5x8) mm. All 26 contact strips are furnished with charge sensitive preamplifiers that have a gain of 500 mV/MeV and a cold FET configuration, chosen in order to minimise noise. The strips are labeled AC 01 - 13 on the AC face and DC 14 to 26 on the DC face. DC14 is not operable as no output was found when connected to an oscilloscope. Changing the DC14 preamplifier did not restore functionality, which has lead to the conclusion that the problem occurs in the cold side of the feed through. Fixing this would require the detector to be warmed and opened up to atmospheric pressure which could result in further damage to the detector, therefore in this work the detector is operated with 25 working strips. Since DC14 is an edge strip on a circular face, it has a small active area relative to the other contacts so efficiency loss is minimal, DC14 represents less than 4 % of the detector active area.

The energy resolution of each working strip was measured, to verify the detector performance. The preamplifier signals were connected individually to an ORTEC 671 spectroscopy amplifier with a shaping time of 3 μs, the

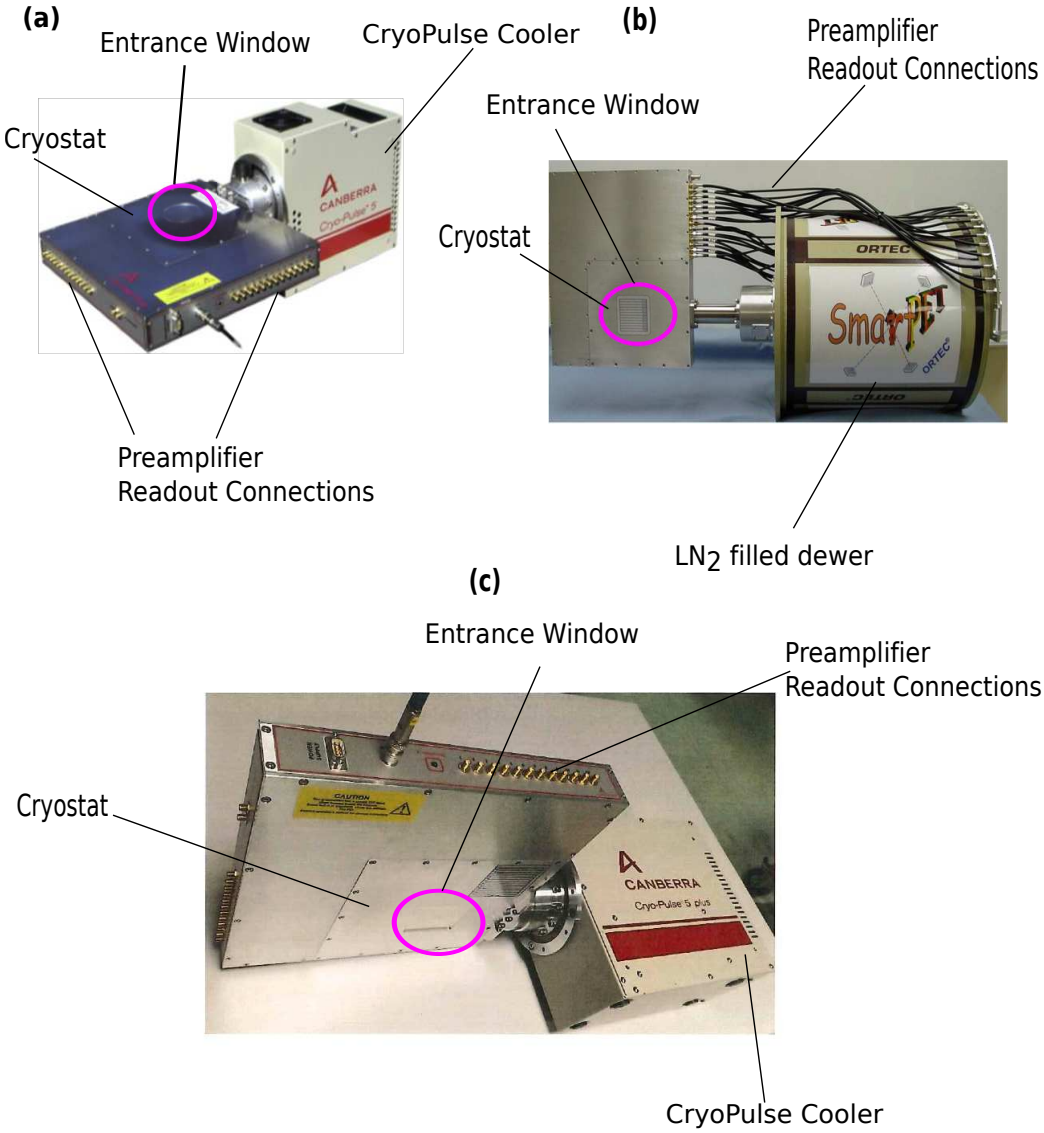

Figure 4.2: Photographs of the ProSPECTus detectors in their cryostats and connected to their respective cooling systems (a) Si(Li) detector and CryoPulse cooling system. (b) Absorber 1 HPGe detector and LN_2 dewar. (c) Absorber 2 HPGe detector and CryoPulse cooling system.

amplified signals were then passed to an ORTEC 927 Multi Channel Analyser and then to a PC. MAESTRO software was used to display and record the energy spectrum for each channel. The software was also used to evaluate the FWHM of the full energy peak and hence determine the energy resolution of each strip. Data were collected using a 415 kBq ^{57}Co source placed 12 cm from the detector. It was found that the average strip energy resolution at 122 keV is 1.15 keV $\pm$ 0.13 keV, with a range of values from 0.97 keV to 1.37 keV. A list of the energy resolutions for each strip, can be found in Appendix A. An in depth characterisation of the Si(Li)) detector has previously been carried out and the results can be found in [55].

4.1.2 Absorber 1 Detector

The absorber 1 detector is an ORTEC manufactured HPGe planar detector. Figure 4.2b is a photograph of the HPGe detector in its aluminium cryostat with a LN_2 dewar (12 liter capacity) connected to the crystal by a cold finger for cooling purposes. The HPGe crystal was cut perpendicular to the <100> plane and is cooled and operated at -196 °C. The depletion voltage of the HPGe crystal is -1300 V and the operating voltage is -1800 V. The negative polarity is applied to the AC (p-type) side with the DC (n-type) side grounded, therefore holes are collected at the AC side and electrons at the DC side. The HPGe crystal has an active volume of (60x60x20) mm, and is placed centrally in its cryostat, resulting in a front and back cryostat separation of 15 mm to each detector face. The active area is surrounded by a 7 mm guard ring. The detector is housed in a cryostat of dimension (35x35x50) cm. The characteristic position resolution is (5x5x20) mm, achieved through 12 orthogonal contact strips with a strip pitch of 5 mm, on the AC (p-type) and DC (n-type) faces of the detector, as is illustrated in Figure 4.3b. The strips coupled to the AC face have a separation of 180 μm whereas the strips coupled to the DC face are separated by 300 μm. The strips on the AC face are labeled AC 1-12 and on the DC face, DC 1-12. All 24 strips are coupled to individual charge sensitive preamplifiers that contain a warm FET and have a gain of 300 mV/MeV. The average energy resolution for all 24 strips

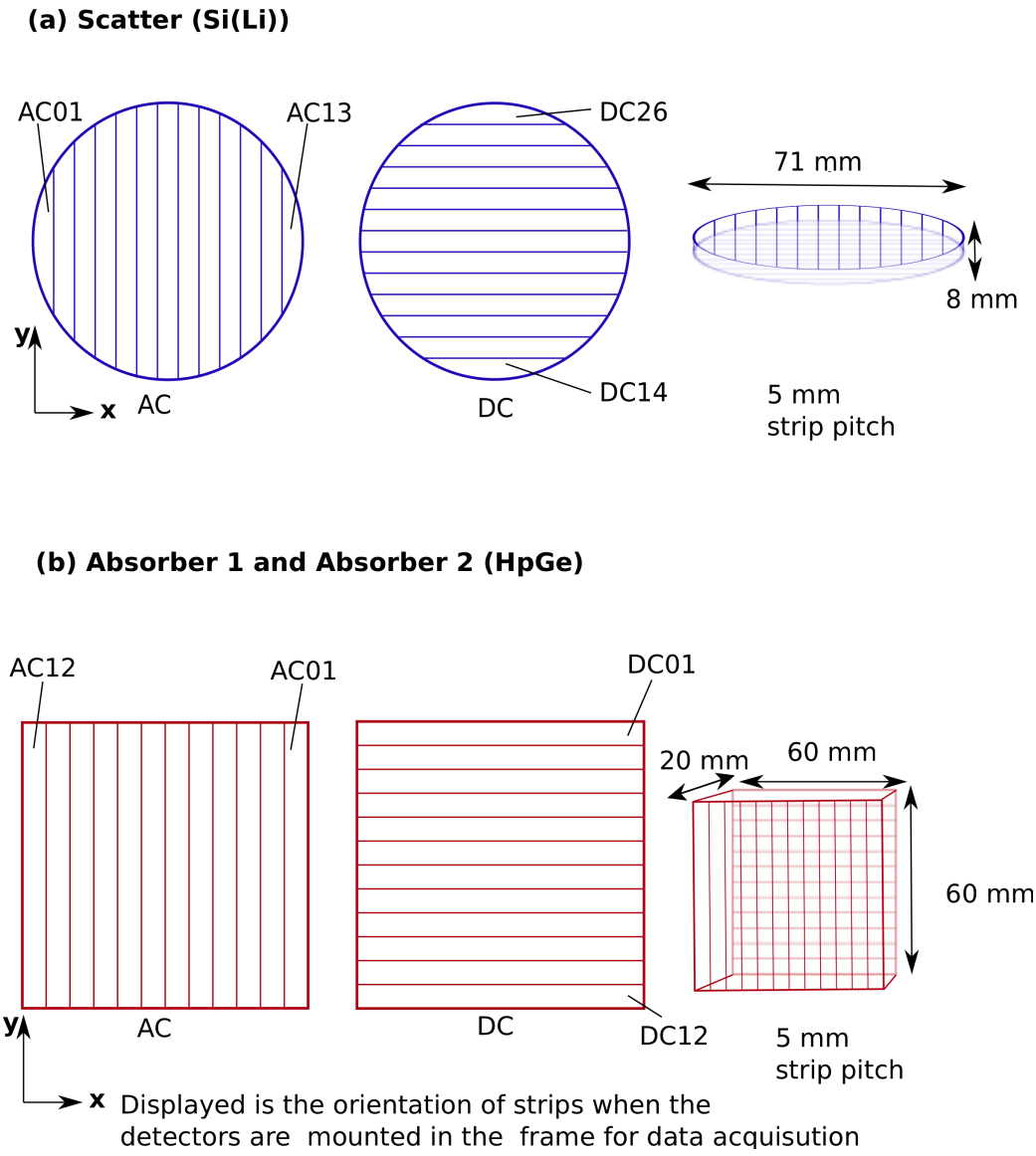

Figure 4.3: Schematic drawing of the active volumes of the (a) scatter (Si(Li)) detector and (b) absorber 1 and 2 (HPGe) detector dimensions. (Not drawn to scale).

was measured using the same methodology as used for the Si(Li) but with a shaping time of 6 μs. The average energy resolution at 122 keV was 2.09 keV, with a range of values from 1.60 keV to 3.5 keV. A full list of the energy resolutions for each strip as listed in Appendix A. The performance of the HPGe detector has previously been fully characterised in [56] as part of the SmartPET project.

4.1.3 Absorber 2 Detector

The absorber 2 detector is a Canberra manufactured HPGe planar detector. The detector is mechanically cooled using a CryoPulse 5 system, so it is operated at a temperature of -185 °C. The detector has the same geometry and dimensions as that of absorber 1. However the information regarding strip separation and thickness has not been disclosed by the manufacturer. Figure 4.2c is a photograph of the detector cryostat and cooling system. The cryostat is made from aluminium and has a aluminium entrance window that is 0.8 mm thick, on each face of the cryostat and has dimensions of (33x33x5) cm. The crystal is assumed to be placed centrally in the cryostat so that there is a gap of 15 mm from the front and back of the detector crystal to the faces of the cryostat. When the cryostat is positioned in the custom made frame, there is an increased separation of 16 mm from the scatter cryostat, this is due to the geometry of the cooling arm. The operational voltage of the detector is the same as that for absorber 1. The same methodology as used for absorber 1 and the scatter detector, was applied to determine an average energy resolution of 1.68 keV $\pm$ 0.4 keV, for 122 keV incident gamma rays. The minimum and maximum energy resolution measured for the absorber 2 detector strips were 1.42 keV and 3.49 keV respectively. The energy resolution response for each strip of the absorber 2 detector can be found in Appendix A.

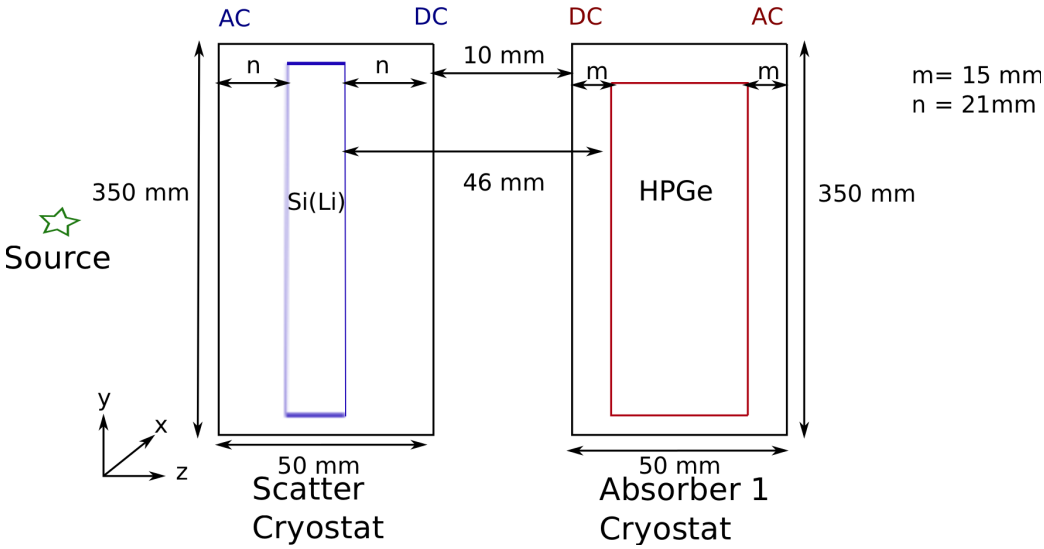

Figure 4.4: Schematic drawing of the detector set up of the ProSPECTus system with the scatter and absorber 1 detectors. Shown is the cryostat and detector separation. The geometry is the same when absorber 2 is used except there is a cryostat separation of 16 mm and hence a detector to detector separation of 52 mm. (Not drawn to scale)

4.2 Experimental Set Up for Imaging

The experimental set up was optimised using absorber 1 whilst waiting for the arrival of absorber 2. Therefore the subsequent sections will be described in terms of absorber 1. Any change of parameters for absorber 2 will also be quoted where appropriate.

4.2.1 Detector Geometric Details

The cryostats were positioned in the custom made frame at the minimum cryostat separation of 10 mm, which results in a face to face crystal separation of 46 mm. A schematic representation of this configuration is shown in Figure 4.4. The purpose of the custom made frame is to ensure that the crystals are aligned to a central axis. With this assumption, an estimate of the range of scattering angles possible for a single single interaction was calculated as shown in Figure 4.5. The value of the maximum scattering angle was found to be $\pm$ 76^0. However, it has since been found that there is an offset in the

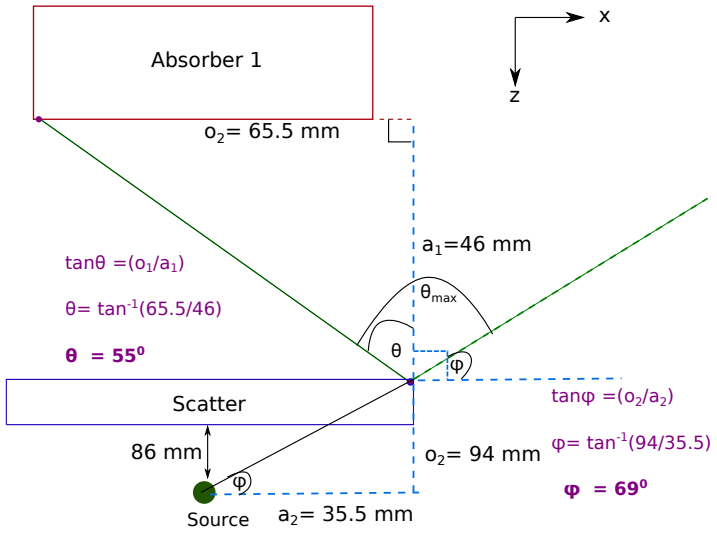

Figure 4.5: Schematic drawing of an estimate maximum Compton scattering angle θ_{max} allowed for single-single interactions with the ProSPECTus system geometry (with absorber 1). Assuming detectors are centrally aligned. Diagram is not drawn to scale.

scatter detector position of 11 mm in the X-direction and 5 mm in the Y-direction. The ProSPECTus setup with absorber 2 has a maximum scattering angle of $\pm$ 73^0, which has been calculated using the same methodology.

4.2.2 Data Acquisition System

Digitiser cards are preferred to analogue electronics for data acquisition as they offer the advantage of storing and processing the preamplifier pulses, enabling the use of post-processing algorithms, such as PSA. The digitisers used with the ProSPECTus system are the CAEN V1724 digitisers [57] [58]. Each CAEN V1724 card has 8 channels and the detector preamplifier signals are sampled at a rate of 100 MHz, corresponding to one sample every 10 ns. For signals that exceed the defined Constant Fraction Discriminator (CFD) energy threshold, 1280 ns of the signal is stored, of which 650 ns of the pulse is before the trigger point, this is sufficient for post processing and analysis. Figure 4.6 shows the concept of how the preamplifier pulses that exceed the

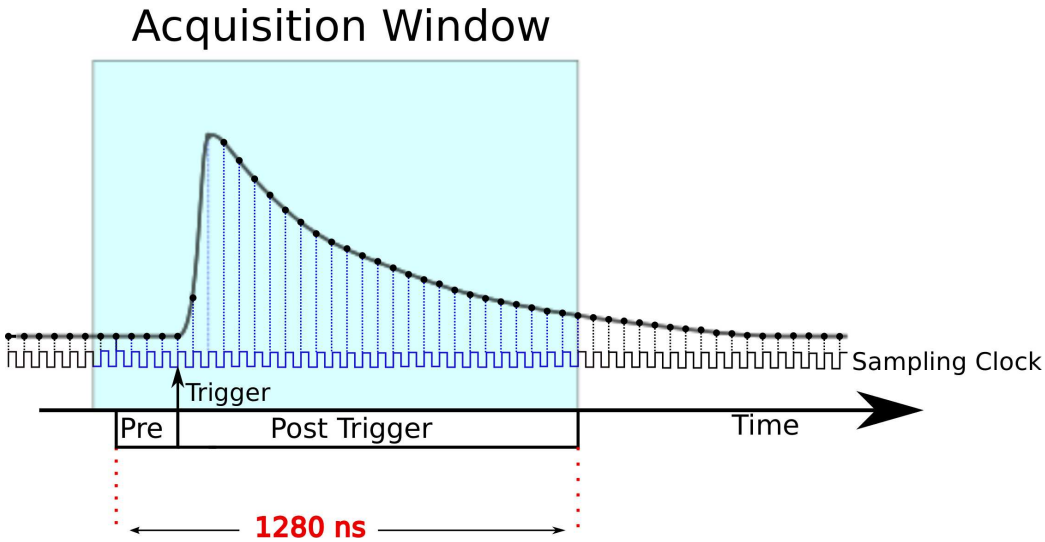

Figure 4.6: Schematic representation of a preamplifier pulse exceeding a user defined trigger threshold point and thus being stored (represented by blue window) with a user defined number of samples before and after the threshold crossing point.

threshold and induce a trigger signal are stored in the 1280 ns acquisition window. The data acquisition system used for ProSPECTus signal processing is shown schematically in Figure 4.7. The preamplifier signal from each strip of both detectors is passed to one of six CAEN V1724 digitiser cards via a Gain and Offset (GO) box. The purpose of the GO box is to amplify the preamplifier signals by a factor of 5 to ensure the full dynamic range (2.5 V) of the CAEN cards is used. The GO box also allows the baseline offsets of each channel to be corrected. The GO box used in the set up had only 47 connectors available for the detector signals, therefore a decision was made to not instrument two of the smallest edge strips of the scatter detector (AC 13 and DC 26) so that the efficiency of the detector system would be reduced as little as possible. Three V1724 digitiser cards are allocated for the 23 Si(Li) signals with 1 spare channel and three cards are used for the 24 HPGe signals. All 6 cards are linked through a universal clock generated by the 1st card, to ensure the time stamps and sampling of all channels in each card are synchronised, this is controlled by the V1495 general purpose logic board. A screen shot of the user interface used to control the cards is shown in Figure

4.8. This interface is used to start data acquisition and access parameters in the digitisers. The cards can be operated in either 'coincidence' or 'singles' (i.e no requirement for coincidence) mode. The coincidence mode requires coincident events in both detectors and is used when collecting Compton imaging data, whereas singles mode can be used to acquire calibration data for each detector or to examine the energy resolution of the detectors.

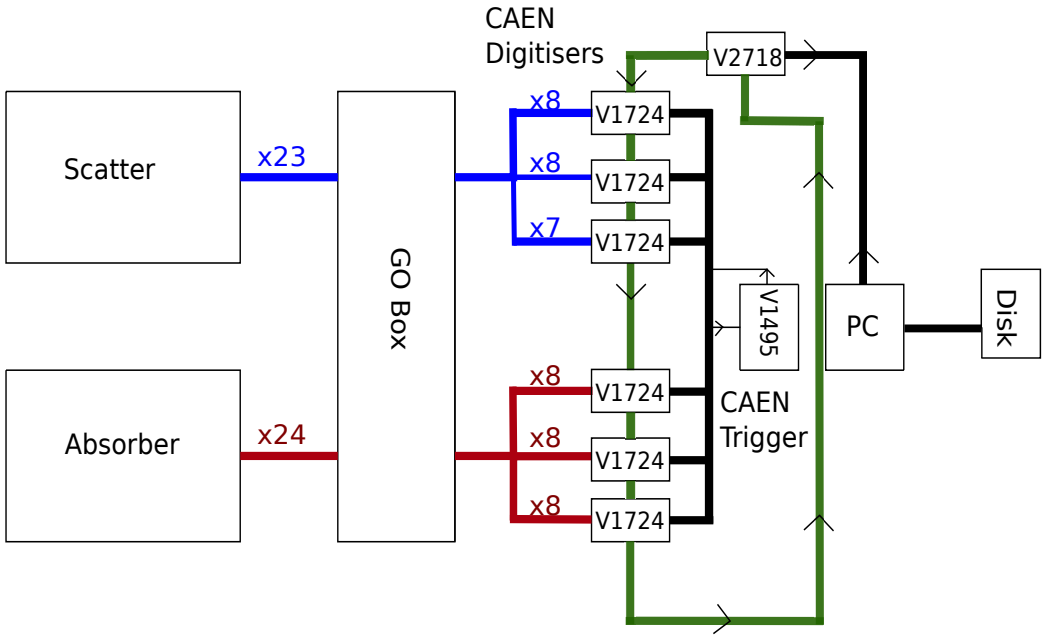

Figure 4.7: Schematic of the digital signal processing electronics used for data acquisition.

When the system is started in coincidence mode, the CAEN V1495 is used to start the acquisition for data collection and reset the universal clock to zero, once the acquisition is started to ensure synchronisation. The trigger signals from the V1724, corresponding to channels that exceed the threshold, are sent to a CAEN V1495 where it is determined if the combination of trigger signals meet all the user defined logic criteria. The coincidence criteria is defined in the software such that:

- At least 1 trigger from the DC side of the Si(Li) and at least 1 trigger signal from the AC side of the HPGe detectors are within the coincidence window. For a fully instrumented detector, if a signal is observed

from one side it should also be recorded on the other. The AC side of the HPGe detector was chosen as the trigger side due to the charge sharing problems on strip DC 11 (in absorber 1).

- The trigger signals occur within a coincidence timing window of 150 ns.

The selection of the coincidence timing window is explained in Section 4.2.6. For events that meet the above requirements, a 'trigger valid' signal is relayed back to the CAEN V1724 cards. This triggers the signals from all V1724 channels to be written out and passed to the PC via the V2718 (VME to PCI Optical Link Bridge) and optical fibre connection, for online processing and storage onto disk for future offline processing. As well as the events that have passed the energy threshold, the events that occur simultaneously (150 ns from first trigger i.e 15 samples) in all strips are written out and stored for future use, for example in PSA algorithms. The data that is stored for each trigger event is the energy deposited, 1280 ns of the pulse trace and event time stamp.

Algorithms programmed into the digitser cards calculate the energy that has been deposited in the detector. The method implemented is a Moving Window Deconvolution (MWD) algorithm / Trapezoidal filter [59] [60], Figure 4.9 shows the basic concept of how the MWD algorithms works. The initial digitised signal is a preamplifier signal with a long decay tail as described in Section 2.3.2. The first stage of the MWD algorithm is to remove the exponential decay and convert the signal into a step function, whilst maintaining the pulse height. The second stage is to differentiate the signal from stage one, to achieve a square pulse. At stage three a moving average window is applied to the step pulse from stage two, in order to smooth and remove noise from the signal, a trapezoidal shape is thus given to the pulse. The energy deposited by the gamma ray in the detector is determined from the peak height, which is measured at the trapezoidal flat top of the signal. The MWD calculation relies on user defined parameters, which can be found in Table 4.1. These settings were chosen as they were found to provide the best energy resolution performance from each of the detectors, using this set

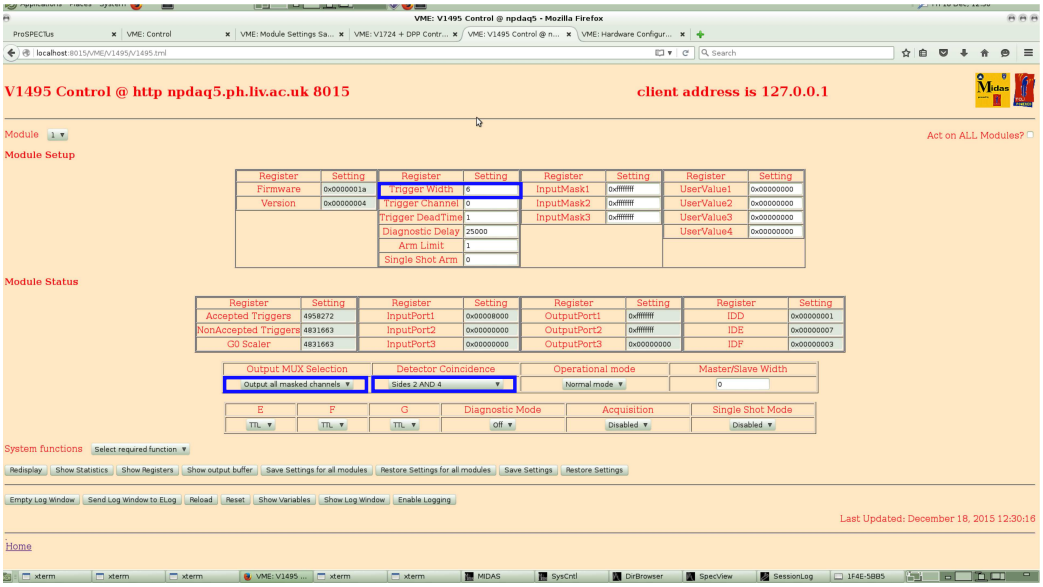

Figure 4.8: Screenshot of the software used to set parameters in the CAEN V1495 cards. Highlighted in blue are the main settings i.e. trigger width (multiply value by 25 to get desired coincidence window in ns), Output all masked channels (stores events from all strips) and detector coincidence (stipulates which sides of the detectors to accept trigger events).

up. The MWD parameters of the scatter and absorber 1 detector were optimised using a 166 keV incident gamma ray from a 0.122 MBq ^{139}Ce source. The source was placed for both scatter and absorber 1 energy investigations so that the gamma rays were incident on the AC side of each, at a distance of 50 mm from the respective cryostats. The optimum parameters for the Si(Li) detector gave an average energy resolution of 2.16 keV, all strips were measured to have an energy resolution within the range of 1.83 keV to 2.42 keV. For the HPGe detector an average energy resolution of 2.54 keV was measured. DC 11 has a relatively poor energy resolution of 5.86 keV due to charge sharing problems, this was previously discovered during the detector characterisation in [56]. If DC11 is excluded the average energy resolution is 2.3 keV, with all subsequent strips achieving an energy resolution within the rang of 2.10 keV and 3.18 keV. The absorber 2 detector energy resolution was investigated on arrival for a different project using a ^{57}Co source with gamma ray energy of 122 keV. The average energy resolution was found to

	Scatter (SiLi)	**Absorber 1 (HPGe)**	**Absorber 2 (HPGe)**
Decay Time	50 μs	50 μs	50 μs
Input Rise Time	250 ns	100 ns (AC side), 250 ns (DC side)	200 ns
Trapezoidal Flat Top	2.5 μs	2.5 μs	5 μs
Trapezoidal Rise Time	5.5 μs	5.5 μs	7 μs

Table 4.1: Table showing user defined MWD parameters for scatter, absorber 1 and absorber 2 detectors. Parameters are for both AC and DC sides of the detector, unless otherwise stated.

be 1.98 keV, with a range of 1.33 keV to 1.72 keV measured for all strips. For all three detectors, the average energy resolution is worse on the AC side as shown in Table 4.2 this is thought to be due to the different electronics on either side (i.e AC and DC coupling) which is explained in [9]. The energy resolution of the edge strips are affected by the weaker electric field at the edge of the crystal [61]. Figure 4.10 show plots of the FWHM of (a) scatter, (b) absorber 1 and (c) absorber 2 detectors.

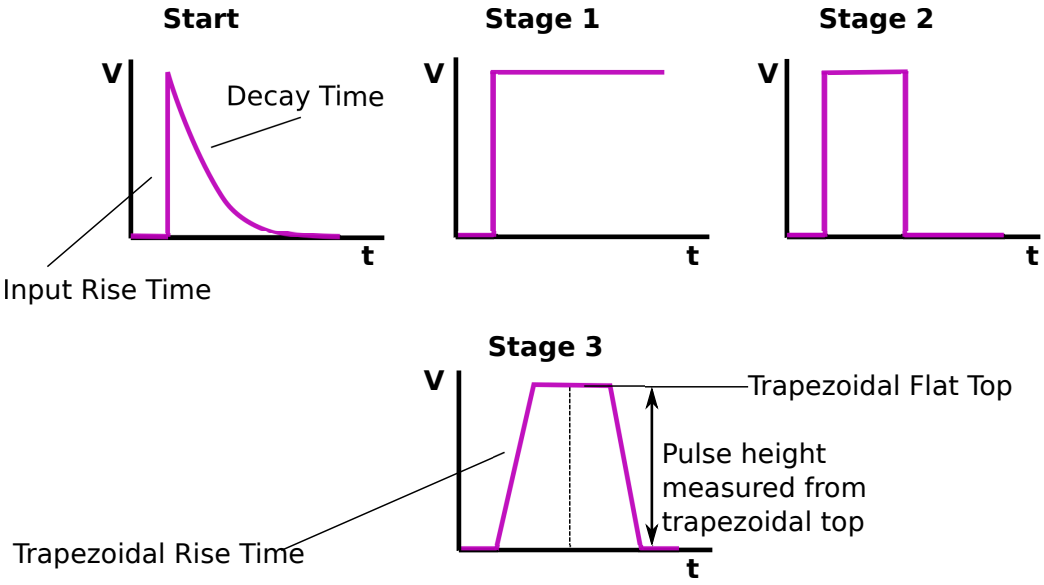

Figure 4.9: Schematic representation of MWD algorithm processing of preamplifier signals.

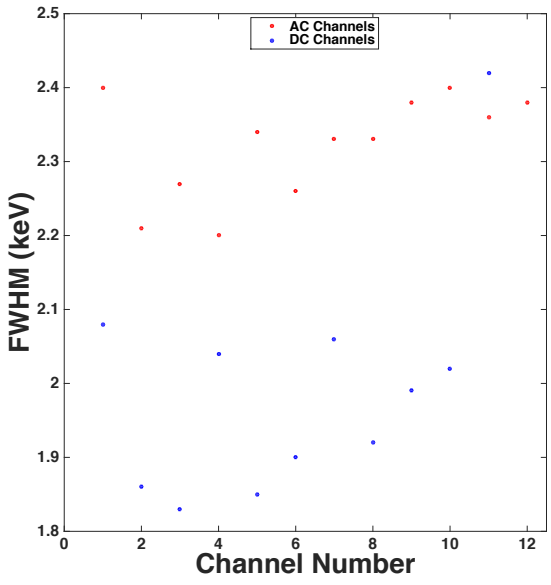
AC Channels
DC Channels
FWHM (keV)
Channel Number
2.5
2.4
2.3
2.2
2.1
2
1.9
1.8
0
2
4
6
8
10
12

(a)

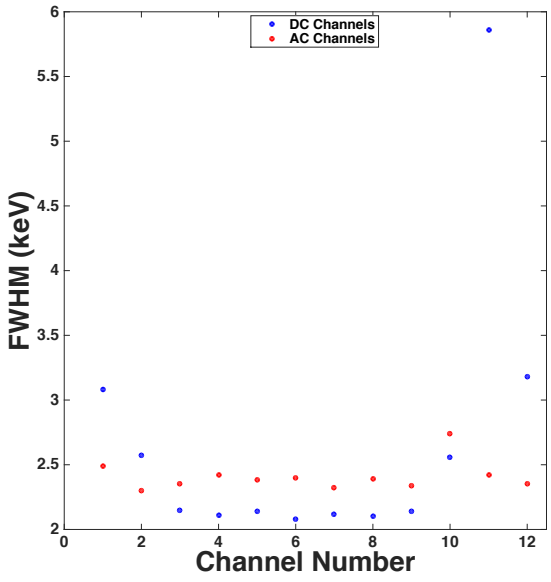
DC Channels
AC Channels
FWHM (keV)
Channel Number
6
5.5
5
4.5
4
3.5
3
2.5
2
0
2
4
6
8
10
12

(b)

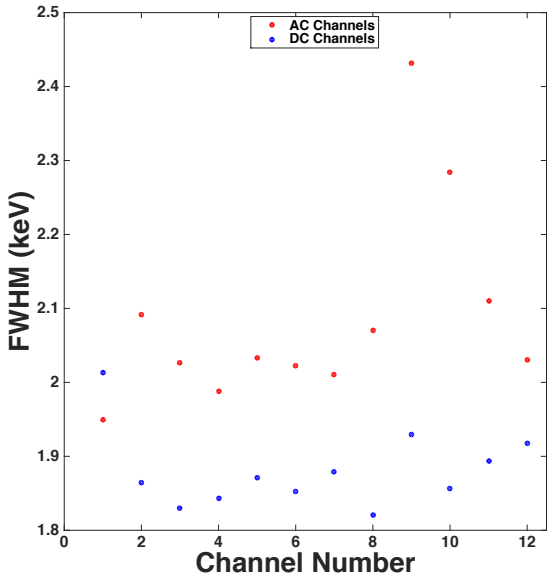

(c)

Figure 4.10: Energy resolution measured at a gamma-ray energy of 166 keV for (a) the scatter detector and (b) the absorber 1 detector. (c) Absorber 2 detectors resolution for an incident gamma ray of 122 keV. All measurements made using digital electronics and the MWD parameters shown in Table 4.1

	AC average energy resolution (keV)	**DC average energy resolution (keV)**
Scatter detector for 166 keV	2.32 ± 0.07	2.00 ± 0.21
Absorber 1 detector for 166 keV	2.41 ± 0.12	2.62 ± 1.08
Absorber 2 detector for 122 keV	2.08 ± 0.14	1.88 ± 0.05

Table 4.2: Average energy resolution for the AC and DC sides of the scatter, absorber 1 and absorber 2 detectors, acquired with Caen digitizer cards. The energy resolutions provided are for incident gamma rays of 166 keV energy and for the absorber 2 detector at 122 keV. All errors shown are calculated from the standard deviation of the data used to calculate the averages.

4.2.3 Energy Calibration

The spectral response of the scatter and both absorber detectors were individually calibrated to known gamma-ray energies. The scatter detector was calibrated up to 166 keV using the 60 keV gamma ray from ^{241}Am and both the 33 keV X-ray and the 166 keV gamma ray from ^{139}Ce. The centroids of these three gamma ray peaks were used to perform a quadratic order calibration. The absorber 1 and detector was calibrated using the same methodology as the scatter detector up to 662 keV, using the gamma rays emitted with energy 60 keV, 166 keV and 662 keV from ^{241}Am, ^{139}Ce and ^{137}Cs respectively. The absorber 2 detector was calibrated on its arrival for a different project using the 80 keV and 364 keV gamma rays from ^{123}Ba and the 122 keV energy gamma rays from a ^{57}Co point source. The absorber 1 and 2 detectors were calibrated over a wider energy range than that of the scatter detector so that gamma-ray imaging for higher energy radioisotopes could be acquired for other projects. The calibrations for all three detectors exhibited good linearity, and the calibration coefficients can be found in Section A.1 of Appendix A.

4.2.4 Data Collection and Processing

Once the necessary Compton imaging data has been collected and saved to disk, it can be further processed through a high level sorting package developed at the University of Liverpool called MTsort [62]. MTsort requires the MIDAS analysis package software as shown in Figure 4.11, which is available from the Daresbury Laboratory Nuclear Physics support web site. MTsort uses a custom programming language and also allows the incorporation of C-algorithms. The program is primarily used in this thesis to select events for the Compton imaging reconstruction algorithms discussed in Section 4.2.9. To select these events, user defined conditions can be implemented, for example ensuring the events are Fold[1,1,1,1] i.e there is one interaction in each detector, which results in charge collection at one strip, on each side of both detectors. Fold [1,1,1,1] events are the events chosen in this thesis to be used with the image reconstruction codes described in Section 4.2.9. The MTsort

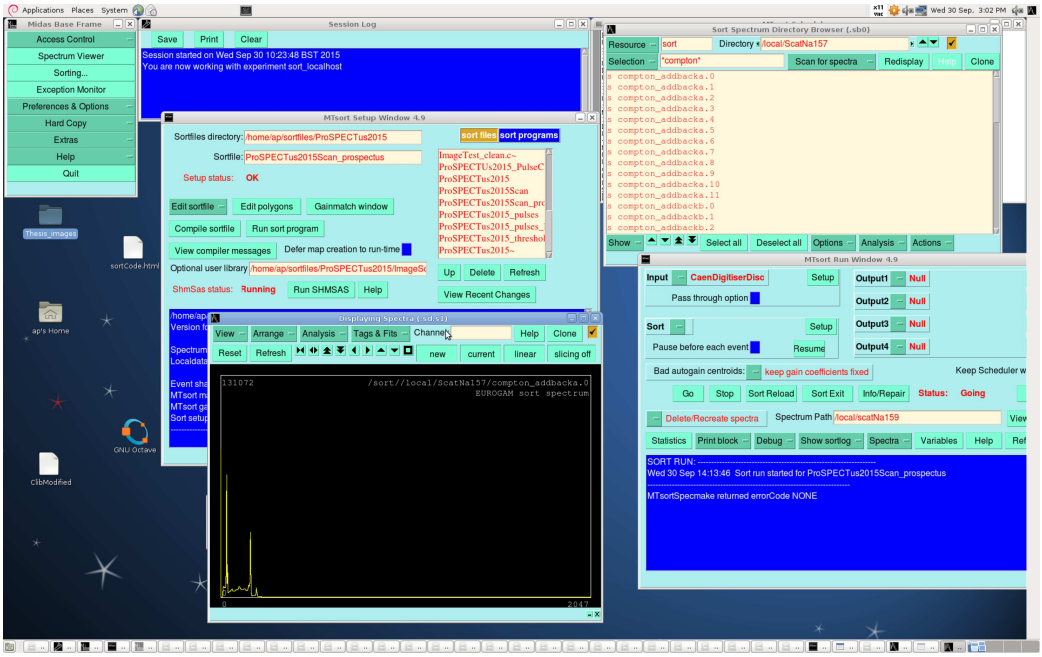

Figure 4.11: Screenshot of the MIDAS software user interface that runs the MTsort program developed at the University of Liverpool. A variety of useful spectra can be created, accessed and viewed using MTsort and the MIDAS software

code used for sorting the data also contains the energy calibration coefficients for both detectors, allowing energy gates to be implemented.

The MTsort software allows spectra and matrices to be created which are of interest to the user, such as the energy recorded by each strip in the detector, which is useful for energy resolution investigations and the energy calibration. The Compton image reconstruction requires an X, Y and Z co-ordinate corresponding to the interaction position in both detectors and the associated energies deposited in those interactions as explained in Section 4.2.9. The signals from either the AC or DC sides of the detectors can be used to obtain the energy values required for the image reconstruction. Figure 4.12 shows the Fold[1,1,1,1] energy add-back spectra from the DC sides of the scatter and absorber 1 detectors. This data was acquired from coincidence measurements of a ^{139}Ce (166 keV) point source, located 65 mm from the scatter cryostat. The AC and DC add-back spectra are essentially

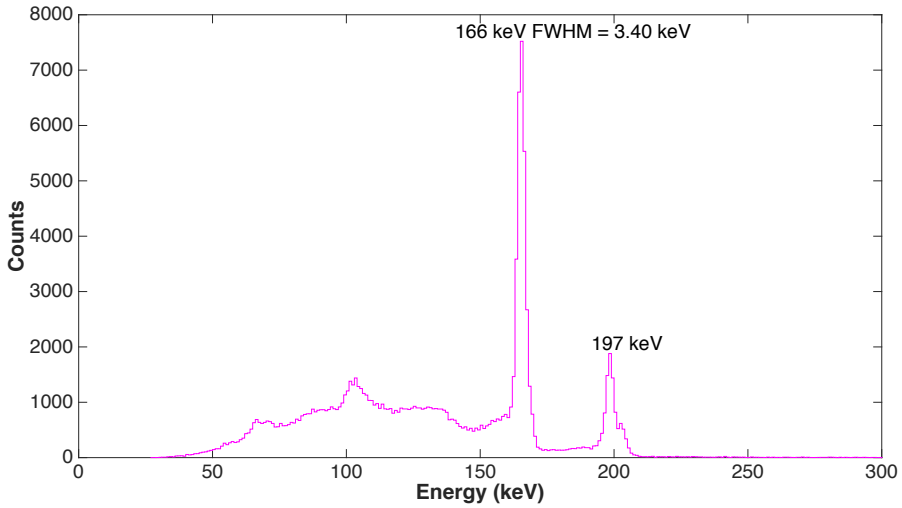

Figure 4.12: Fold [1,1,1,1] gamma-ray energy addback spectrum of the AC side of the scatter and absorber 1 detectors, produced using a ^{139}Ce source.

the combined AC or DC Fold[1,1,1,1] events of the scatter and absorber detector, it is shown in Figure 4.12 that the DC add-back energy spectra has at 166 keV, an energy resolution of 3.40 keV. The DC energy values were chosen for use in the image reconstruction algorithms.

Once the data is processed through the MTsort code, a text file is created that contains the energy deposits and the corresponding strip numbers. The strip numbers can be used by the imaging code to calculate the co-ordinates of interaction position with the precision of the position resolution of the detectors.

4.2.5 Noise Thresholds

Thresholds are set in the V1724 cards for both the scatter and absorber detectors in order to distinguish events arising from useful gamma-ray interactions from events corresponding to noise. The noise arises from two components; electrical noise and from cross talk that is due to capacitive coupling from neighboring strips. The choice of threshold is especially important in the scatter detector as the majority of events that are detected whilst imaging ^{139}Ce are below 40 keV. GAMOS (GEANT4-based Architecture for Medicine

Oriented Simulations) [63] which has previously been validated to match experimental Compton camera data [64] was used to produce Figure 4.13 which shows the energy deposited in the scatter and absorber detectors from single-single fully absorbed events. This distribution is for the ProSPECTus set up with a ^{139}Ce source placed 6.5 cm away from the cryostat of the scatter detector. Almost 91% of events deposited in the scatter detector occur below 36 keV, by contrast 90% of the gamma-ray interactions in the absorber detector are greater than 136 keV. Figure 4.14 is a plot of energy deposited in the scatter detector, as a function of scattering angle, an incident gamma-ray energy of 166 keV was assumed. This calculation is assuming only one Compton scatter interaction occurs. Events that deposit less than 40 keV in the scatter detector are the ones that are useful for Compton imaging as these are the only events for which the gamma rays can be forward scattered onto the absorber detector. As described in Section 4.2.1 the maximum scattering angle for single single interactions in the ProSPECTus system is 76^0. According to Figure 4.14 this corresponds to a maximum energy deposit of $\sim$ 35 keV. Deposits that occur above this in the scatter detector as seen Figure 4.13 can be attributed due to events that first interact in the absorber and then the scatter or multiple interactions in one strip. It is not possible for the detectors to distinguish between backscattered events, however an energy gate on the scatter events can be applied to exclude these events that occur above 35 keV. Doppler broadening can also contribute to the deposits seen above 35 keV. It is important for the system efficiency to maximise the detection of useful events, therefore the threshold in the scatter detector should be set as low as possible above the noise. In the absorber detector as shown in Figure 4.13 the forward scattered events recorded are greater than 130 keV, therefore the absorber can be operated with a higher threshold.

The threshold of each strip in both detectors were individually set through the CAEN digitiser software programmed in singles mode. ^{241}Am point source was used when setting the thresholds. This was for two reasons; the lowest X-ray emission for ^{241}Am is at 11 keV (useful to estimate level of noise) and its characteristic gamma-ray energy is 60 keV, thus when observing the lower end of the energy spectrum, there is no interference from

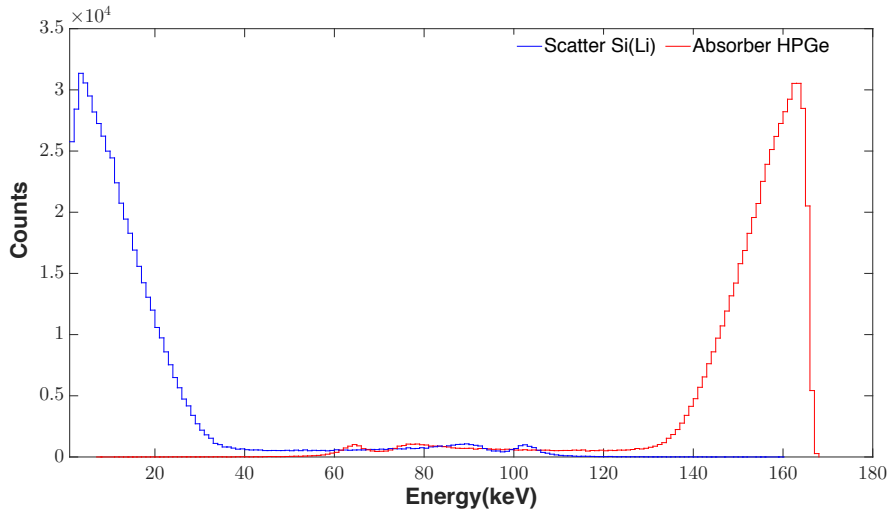

Figure 4.13: A GAMOS simulated energy distribution of fully absorbed coincident single-single events, in the ProSPECTus for 166 keV incident gamma ray energy. The simulations were run with the same ProSPECTus geometry used with absorber 1 i.e. 46 mm detector separation and point source placed 65 mm from scatter cryostat.

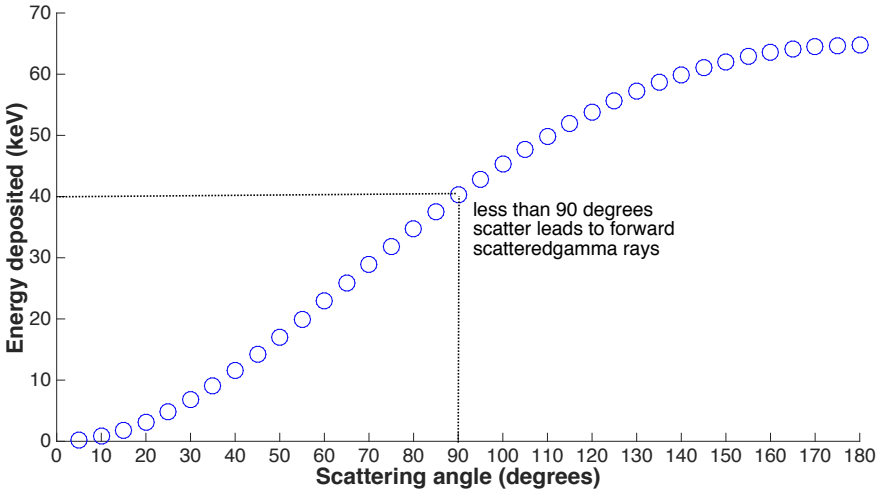

Figure 4.14: Plot showing the calculated energy deposited in the scatter detector for incident 166 keV gamma rays as a function of scattering angle between 5 and 180 degrees.

X-rays and gamma rays which could hide the presence of noise and mask the point of the threshold. Image charges (as explained in Section 2.3.2) can produce triggers if their pulse height passes the threshold, the MWD algorithm can then calculate non zero energy and this leads to extra counts in the energy spectrum, typically at energies less than 5 keV. The 60 keV gamma ray emitted by the ^{241}Am point source is close to the maximum energy deposited by the scattered 166 keV gamma rays from ^{139}Ce, therefore through using ^{241}Am the maximum contribution from the MWD algorithm to low energy noise from image charges can be estimated. Figure 4.15 shows the energy spectrum collected on strip AC04 from the Si(Li) detector. It can be seen that the noise in the spectrum is prevalent up to 4 keV. The average threshold set on the Si(Li) strips is 8 keV, this is because at threshold values between 4 keV and 8 keV a dominance of events corresponding to image charge triggers occurs in the noise region. The average strip threshold for the absorber detector is 15 keV, although the majority of events that are of interest deposit energy greater than $\sim$ 130 keV. This relatively low threshold value is selected in order to enable future sophisticated reconstruction codes to be compatible with the data collected from this set up. For example codes that use fold 2 events in the absorber detector in image reconstruction would require events that deposit energy lower than 100 keV in the absorber detector. For instances when data is taken with high activity sources, in order to prevent the data acquisition system suffering significant dead time the absorber threshold was raised to 90 keV.

The threshold described above are known as digital hardware thresholds, software thresholds can also be further applied in the MTsort code when data processing. The software thresholds were chosen to be the same as the average digital threshold, in order to keep the thresholds as low as possible to maximise efficiency.

4.2.6 System Timing Response

A coincidence timing window is the range of time allowed for the triggers from a multi detector system to be collected and correlated to form an event.

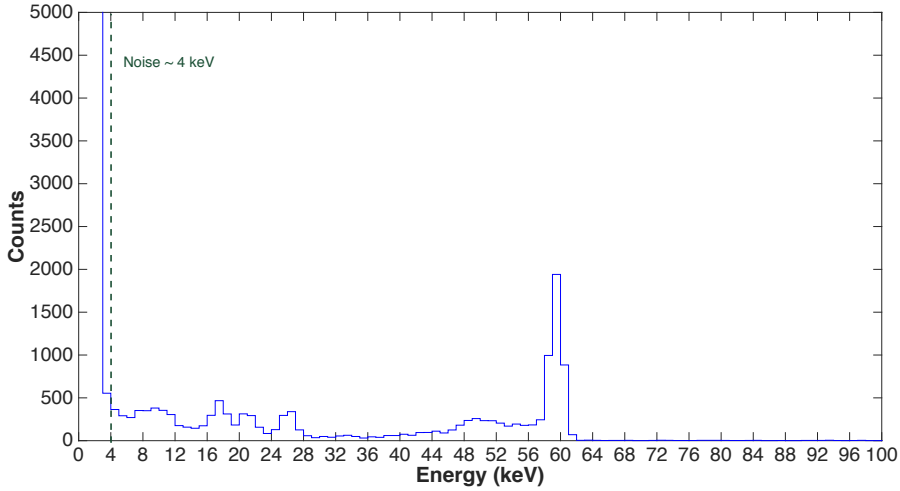

Figure 4.15: Energy spectrum collected with strip AC04 of the Si(Li) detector using a ^{241}Am source. Noise is observed up to 4 keV.

The window is optimised to maximise acquisition of events that are truly in coincidence and minimise random coincidences arising from the detection of background events. For a Compton camera system, a useful event is defined as a gamma ray that has deposited a fraction of its incident energy through a single Compton scatter interaction in the scatter detector before it is fully absorbed in the absorber detector, through the photoelectric process as explained in Section 3.3.1. It is important to maximise the acquisition of these events. If the coincidence window is too narrow, true coincidence events will not be collected and therefore the efficiency of the system can be significantly reduced. A coincidence window that is too wide results in the increase of random events, which manifests in the reconstructed image through background noise and image resolution degradation. In order to determine what the coincidence timing window should be set at for data acquisition with the ProSPECTus system, it is necessary to measure the timing resolution of both the scatter and absorber detectors individually. As well as the timing resolution of the detectors, the effects of the digitiser cards and digital trigger also have to be explored, in order to deduce how much they contribute to the overall timing response of the system. Once these

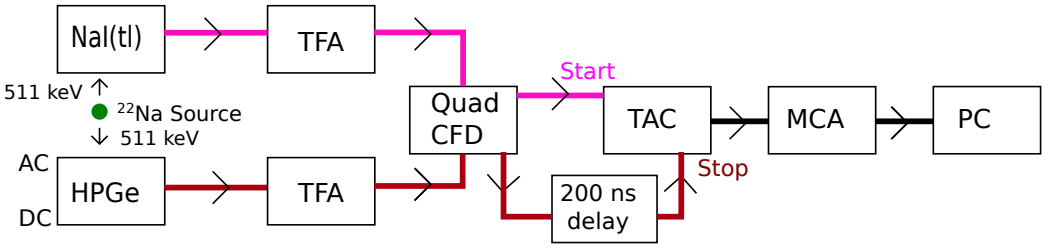

Figure 4.16: Schematic representation of the analogue electronics used for the intrinsic HPGe/Si(Li) TAC measurements.

results are ascertained, the optimum coincidence window can be set for data acquisition.

Intrinsic timing response of detectors

Figure 4.16 is a schematic diagram illustrating the analogue electronics setup used to investigate the intrinsic timing resolution of the absorber 1 and scatter detectors. Both detectors were investigated in coincidence with a NaI(Tl) detector. The fast timing response of the NaI(Tl) detector is approximately 4 ns [65] this allows the timing response of the circuit to be attributed to the ProSPECTus detector under analysis. integral component to this circuit is the Time-to-Amplitude-Converter (TAC). A TAC unit allows the time relationship between coincident events from two detectors to be determined. A TAC unit operates by measuring the time between two pulses and creates a voltage output pulse proportional to the time measured. A ^{22}Na source was used as this emits two co-linear 511 keV gamma rays in coincidence. The source was placed between the NaI(Tl) detector and the ProSPECTus detector such that the gamma rays were incident on the AC face of the ProSPECTus detector under investigation. In order to obtain an average timing response of each detector, all 47 strips from both detectors were individually and sequentially investigated. The preamplifier signal from each strip and the NaI(Tl) detector was amplified using individual Ortec 474 Timing Fast Amplifiers (TFA), set at minimum integration (50 ns) and maximum differentiation (200 ns) to preserve the fast timing signals, the TFA signals were then passed to two inputs of an Ortec 935 quad Constant Fraction Dis-

criminator (CFD). The CFD threshold was set at approximately 500 keV for the NaI(Tl) and HPGe detectors. The thresholds were set by connecting the preamplifier signal of the strip under investigation via a spectroscopy amplifier to an oscilloscope and the corresponding CFD signal to the oscilloscope. The oscilloscope was triggered off the CFD pulses, whilst the CFD threshold was manually adjusted until the 511 keV linear spectroscopy amplifier signals disappeared on the scope, by lowering the threshold to below this point to where the signal reappears, the threshold can be set at approximately 500 keV. The Si(Li) had a threshold set in the same way however it was not possible to set at 500 keV, due to the low probability of full energy deposits. Figure 4.17 shows a ^{22}Na energy spectrum collected on strip AC06 of the Si(Li) detector. The full spectrum has a total number of counts of 1449288 whereas only 1553 are in the 511 keV photopeak. The Compton edge however from approximately 300 - 340 keV has a total number of 111506 counts. Therefore it was decided setting the threshold at the Compton edge would be more efficient.

The logic output pulses from the CFD for both detectors were input to the TAC unit as start and stop signals. The NaI(Tl) detector was chosen as the start signal and the HPGe/Si(Li) via a 200 ns delay as the stop. The output of the TAC was connected to an ORTEC 927 MCA to produce a spectrum displaying the distribution of the TAC pulses using the ORTEC Maestro software (MAE) [66]. This time spectrum was calibrated by incorporating fixed time delays into the circuit. The timing resolution attributed to the detector under investigation is defined as the FWHM of the coincident peak in the timing spectrum.

Figure 4.18 shows one of the TAC spectra collected from strip AC09 of HPGe where the FWHM was measured to be 18 ns. The average analogue intrinsic timing resolution for the HPGe and Si(Li) strips was found to be 21 ns $\pm$ 4 ns and 26 ns $\pm$ 6 ns respectively. These results can be found in Table 4.3. A full set of FWHM result for both detectors can be found in Appendix A. The AC and DC side of the Si(Li) detector have consistent timing resolutions of 21 ns however for the HPGe detector the AC side has an average timing resolution of 21 ns $\pm$ 2 ns whereas for the DC side it is 31

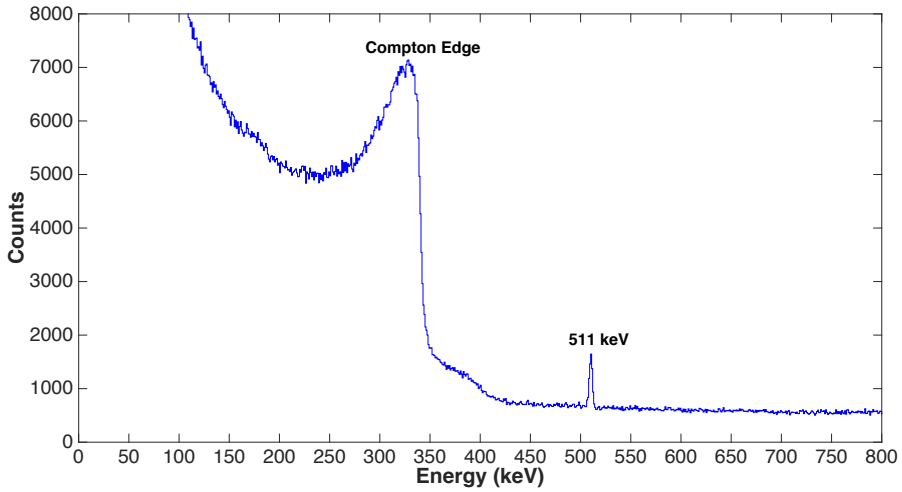

Figure 4.17: ^{22}Na gamma ray energy spectrum collected with Si(Li) strip AC06. The spectrum is clearly dominated by Compton events, in the energy range < 340 keV.

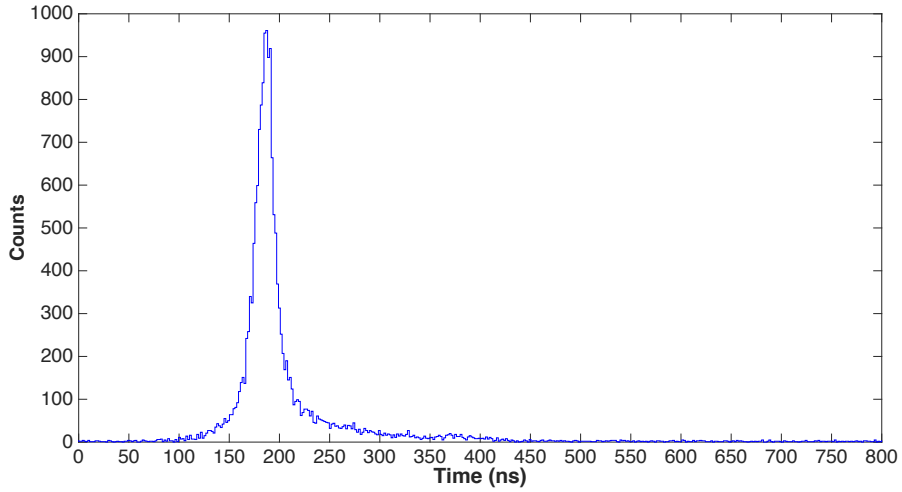

Figure 4.18: Intrinsic Analogue HPGe and NaI(Tl) TAC peak from strip AC09, generated from coincident events from ^{22}Na a (511 keV) source. The FWHM of this peak is 18 ns.

	Analogue		**Digital**		**Digital Gated**	
	Si(Li)	HPGe	Si(Li)	HPGe	Si(Li)	HPGe
Average AC Timing Resolution (ns)	21 ± 2	21 ± 2	25 ± 2	26 ± 2	16 ± 2	20 ± 2
Average DC Timing Resolution (ns)	21 ± 4	31 ± 2	23 ± 1	28 ± 2	16 ± 1	23 ± 3
Overall Average Timing Resolution (ns)	21 ± 4	26 ± 6	23 ± 2	27 ± 3	16 ± 1	22 ± 3

Table 4.3: Table displaying the average timing resolution of both the Si(Li) and HPGe detectors. The average timing response is shown for the AC and DC sides of both detectors as well as the overall average timing response.

ns ± 2 ns. It is assumed that the poorer timing resolution on the DC side is due to the fact that the gamma ray is incident on the AC face meaning an exponential attenuation curve profile through the depth of the detector, therefore the majority of the interactions will occur closest to the AC side than the DC side.

Intrinsic timing response - CAEN V1724 digitiser cards and analogue trigger

To investigate the influence of the CAEN V1724 digitiser cards on the timing resolution of the system, independent of the V1495 trigger card, the internal trigger of V1724 was turned off. The CFD output for each detector was connected to an analogue 775 logic unit, which provided external trigger pulses to the digitiser cards as shown schematically in Figure 4.19. The preamplifier signals from the detector strip under investigation were input to the CAEN V1724 card via a GO box. The timing resolution was again measured using the co-linear 511 keV gamma rays from a ^{22}Na source. A coincidence peak was generated using a C-code incorporated into MTsort rather than through utilising a TAC unit. Figure 4.20 illustrates how the code analysed the signals to produce a prompt coincidence peak. The baseline of each pulse was sampled 20 times. The standard deviation (σ) of the baseline was then found. The leading edge threshold was set at signal height which is the mean + 5σ, this was the point that was found to be consistently above the noise and give the best timing resolution. A linear interpolation was then used

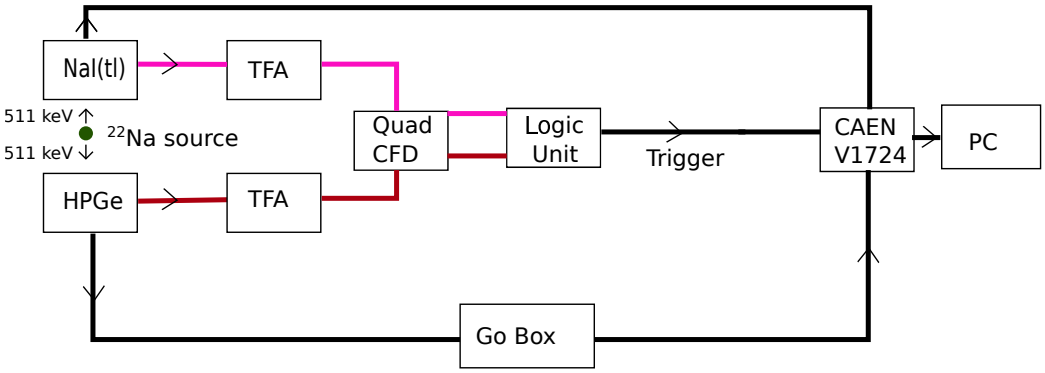

Figure 4.19: Schematic representation of the analogue electronics and CAEN digitisers used for the intrinsic HPGe/Si(Li) coincidence peak timing measurements.

to change the sampling from 10 ns to 2 ns. The time between the triggers arriving from coincidence events from each detector was then deduced from the time between the pulses arriving and exceeding the threshold. One advantage of this methodology is that user defined gates could be implemented i.e. specifying pulses of certain energy to contribute to the coincidence peak. For the HPGe and NaI(Tl) detectors the 511 keV peak was gated and for the Si(Li) detector the Compton edge at 320 keV to 343 keV was gated on. This provides a more accurate coincidence time for the 511 keV incident gamma rays as other coincidence events are suppressed. All channels for both the Si(Li) and HPGe (absorber 1) detectors were tested using this methodology. The average gated timing resolution for the HPGe detector was found to be 22 ns $\pm$ 2.5 ns and for the Si(Li) to be 16 ns $\pm$ 1.3 ns. For the measurements with no energy gate implemented, the average timing resolution for the HPGe detector was found to be 27 ns $\pm$ 2.3 ns and 23 ns $\pm$ 1.5 ns for the Si(Li) detector. These results are displayed in Table 4.3. The errors on the average values are calculated from the standard deviation of the results of all strips. A full list of the individual strip timing measurements can be found in Appendix A.

The digital timing response with no energy gates is the most comparable result to the analogue measurements as the same thresholds are used, i.e set with the analogue CFD. The thresholds were set to the same value in both

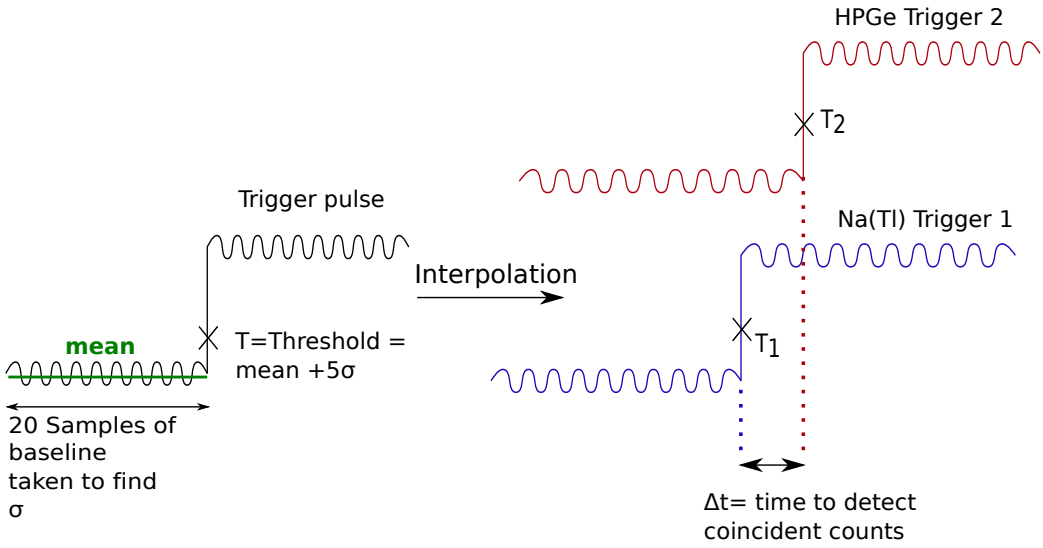

Figure 4.20: Schematic diagram showing how the timing resolution for the CAEN digitsers were measured.

investigations and so the same pulses were allowed to contribute to the timing response. The average timing response for each detector for both methods show good agreement when using a standard consistency check with:

$$|A - B| < 3\sqrt{(\Delta A)^2 + (\Delta B)^2} \tag{4.1}$$

Where A and B is the average timing measurement for the analogue methodology and digital methodology respectively. ΔA and ΔB are the errors associated to these values (calculated by the standard deviation). This check was calculated for both the Si(Li) and HPGe detector and both revealed that the average timing resolution measurements are consistent when using the analogue or digital methodology. The values used in Equation 4.1 and the results are shown in Table 4.4.

4.2.7 ProSPECTus Timing Resolution

The results in Table 4.3 show good agreement between analogue and digital measurements as previously discussed. Therefore, the combined timing resolution of the two detectors of the ProSPECTus system was investigated

	A	**△A**	**B**	**△B**	$\|A-B\|$	$3\sqrt{(\Delta A)^2+(\Delta B)^2}$	**Consistent**
Si(Li) analogue and Si(Li) digital	21	4	23	2	2	13	Yes
HPGe analogue and HPGe digital	26	6	27	3	1	20	Yes

Table 4.4: Consistency check using Equation 4.1 to check if the average timing resolutions are consistent when being measured with the analogue electronics and with using the digitiser cards.

using the digital cards and analogue trigger. The digital approach has the advantage of enabling gating on specific energy regions such as the 511 keV gamma rays in the HPGe detector and the Compton edge events in the Si(Li) detector, allowing a more accurate timing response to be found. The start signal was chosen to be from the Si(Li) detector and the stop signal taken from the HPGe detector. The average intrinsic timing response of the Si(Li) and HPGe detectors is known from the previous investigations and therefore it is predicted that they will have a combined timing response of 36 ns for 511 keV coincidence events and 27 ns for energy gated events. This value is determined through adding in quadrature the average intrinsic timing response of both the non gated and gated average intrinsic timing response values which can be found in Table 4.3. A central strip for each detector was chosen for investigation and also edge strips at opposing edges of each detector, this was in order to reveal the timing response of the detectors at the geometrical extremities.

The results for the timing resolution of the ProSPECTus sytem with the selected strips are found in Table 4.5. The average timing response from these strips is 36 ns for all coincident events and 26 ns for the energy gated events. Both these results concur with the predicted overall timing response of the system from the previous intrinsic investigations.

Detector Strips			
Silicon	**Germanium**	**Time Resolution (ns)**	**Gated Time Resolution (ns)**
DC20	DC06	35	26
DC21	DC05	41	27
AC06	AC06	34	27
AC04	AC03	32	23

Table 4.5: Table displaying the timing resolution of the ProSPECTus system, of the selected strips, chosen to demonstrate the timing response at the geometrical extremities of the system. Each value is considered to have an associated error of 1 ns.

4.2.8 Investigation of the Coincidence Window in the CAEN Digitiser Cards

The coincidence timing window was set at 50 ns for data acquisition based on the above investigations, but it was found that this was inadequate, as a low rate of coincident 511 keV gamma rays were observed within this timing window. The timing of the digital trigger was therefore further investigated, by varying the timing window and collecting Compton imaging data i.e number of events in a photopeak of add-back spectra, from both ^{22}Na (511 keV) and ^{139}Ce (166 keV) individually. ^{139}Ce was introduced into these timing investigations to determine the effect of incident gamma-ray energy on the timing response, particularly at typical medical-imaging energies. ^{139}Ce could not be used in the previous timing investigations as a source that emitted gamma rays in coincidence was required.

Coincident Compton imaging data was collected for coincidence time windows between 50 ns and 400 ns. The coincidence event rate was recorded for both ^{22}Na and ^{139}Ce and plotted in Figure 4.21a and b respectively. It can be seen that there is a delay of around 150 ns for the collection of 511 keV Compton imaging data, up until this point, random coincidences are assumed to be dominating in this region. The optimum timing window is $\sim$ 250 ns, which corresponds to the plateau point, on the graph. For 166 keV as shown in Figure 4.21b the delay for acquiring 166 keV Compton imaging data is between 100 ns and 125 ns, as between these points there is the biggest difference (increase of counts) between successive timing window values. The

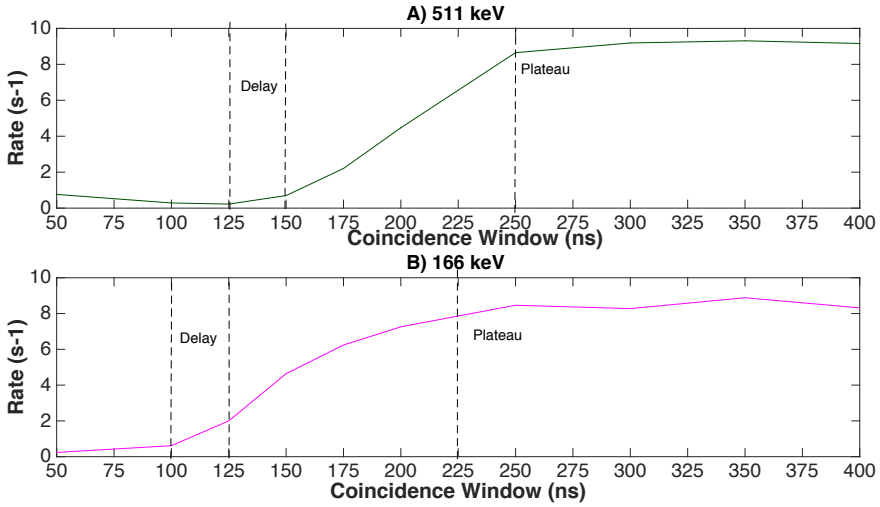

Figure 4.21: Rate of Compton imaging events for (a) 511 keV gamma rays and (b) 166 keV gamma rays, for a range of coincidence window times from 50 to 400 ns. The errors are not displayed on the graph as they have been calculated using Poisson statistics to be less than 5 %.

optimum coincidence window is $\sim$ 225 ns, corresponding to the plateau as shown in Figure 4.21b.

In order to reduce this delay, the coincidence window settings predicted by the previous investigations the CAEN v1724 digitiser parameters were investigated. It was found that through adjusting the 'rise time' values on the cards, a reduction of 50 ns in the delay could be achieved. The rise times were found through checking the output pulses of a channel from both the AC and DC side of both detectors on an oscilloscope with a 166 keV gamma rays incident on the detectors. This rise time parameter in the CAEN software corresponds to the delay that can be added in an analogue CFD, however details of the exact functionality of the CFD algorithms in the CAEN V1724 cards are not disclosed by CAEN. Figure 4.22a shows the coincident event rates for 166 keV at the optimised settings. The collection of coincident data now begins between 25 ns and 50 ns. Figure 4.22 b shows the change of rate between each timing window. It can be seen from this plot all coincident data is collected after approximately 125 ns. A timing window of 150 ns was therefore chosen in order to encompass the maximum amount of Compton

events without the inclusion of a high number of random events.

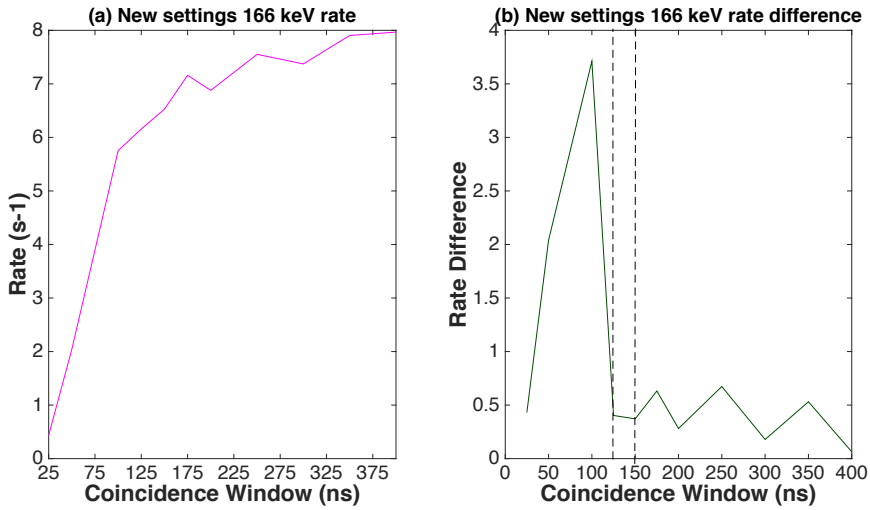

Figure 4.22: (a) Rate of coincidence events for 166 keV gamma rays using optimised settings. (b) Differentiated values from plot of (a). All true coincidence events take place within a window between 25 and 125 ns, therefore a timing window of 150 ns was chosen.

4.2.9 Image Reconstruction

Two image reconstruction algorithms used for the ProSPECTus project have been developed to process events that scatter once in the scatter detector and are then fully absorbed in the absorber detector. The first is an analytical algorithm based on simple back projection and the second is an iterative reconstruction algorithm. Both of these algorithms have been used to reconstruct data in this thesis and their functionality is therefore described briefly.

Analytical

The analytical image reconstruction algorithm developed at the University of Liverpool is based on a simple back projection method, which allows for fast (real-time) processing of the acquired data. The data is pre-selected for imaging through the selection criteria established in Section 4.2.4. As

previously mentioned once the data is processed via the MT-sort algorithm, a text file is created to be used with the image reconstruction codes, this details the energy deposited and the strip number the events are correlated to. The analytical reconstruction code determines The X and Y co-ordinates via the following relationship:

$$\text{Position of interaction} = (N-1) * 5 + 2.5 \tag{4.2}$$

where N is the strip that triggered and 2.5 is the mid length of each strip. Hence the center of the strip in X and Y is deemed as the interaction point. The Z co-ordinate of interaction is normally assumed to be in the center of the detector in depth. However GAMOS simulations were used to investigate the average interaction position in the depth of the absorber and scatter detector for single-single events of a 166 keV incident gamma ray. It was found for the scatter detector that the average interaction position was indeed at 4 mm which corresponds to the central point. However for the Absorber detector it was found that for gamma rays that have undergone one Compton scatter in the scatter detector, the average interaction position is located at 5 mm in depth from the front of the absorber face closest to the source. Therefore for all data reconstructed in this thesis, the point of interaction in depth for the scatter and absorber detectors are at 4 mm and 10 mm respectively.

The algorithm uses these values and trigonometric relationships to define a conic on an imaging plane. The imaging plane location is defined by the user as the distance in Z, from the back of the absorber detector to the source, as shown in Figure 4.23. In this thesis, this distance is referred to as the Z-slice. Figure 4.23 also shows how the conics are defined via trigonometry, on the imaging plane. In the illustration, d is the distance between the scatter interaction in Z and the imaging plane, θ is the Compton scattering angle as defined in Equation 3.3 and r is the radius of the conic. The imaging algorithm is implemented in a C++ code which uses Root [67] for visualisation and fitting.

The output of the algorithm is the Compton image, which is a 2D matrix

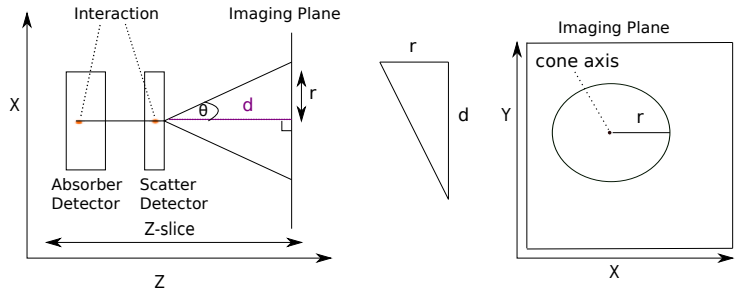

Figure 4.23: Schematic diagrams of how the analytical image reconstruction code, creates conics on an imaging plane using trigonometric calculations.

that displays intensity as a function of X-Y position in the chosen Z-Slice. In addition to the Compton image, intensity profiles through the X and Y plane at the point where maximum intensity occurs are also output from the algorithm. These intensity profiles are fitted with a Lorentzian peak on a quadratic background, which is chosen as this best fits the distribution profile of a point source. Measurement of the FWHM of the fitted data is used as a measure of the image resolution.

The goodness of the fit to the data and the quality of the image produced can be optimised by the user through certain parameters that are defined initially by the user before the algorithm reconstructs and fits the data. The user parameters of the algorithm are:

- **Energy gate** with a lower and upper limit. A gate can be applied on the energy deposited in the scatter and absorber detectors and/or the total energy in the system.

- **Compression factor** to define resolution of imaging space. Converts from mm to pixels, a large compression factor is useful for low statistics data.

- **Pixel range** to be fitted in intensity profile. The accuracy of the fit is improved by varying the range of pixels used to calculate the fit of the 1-D intensity distribution.

- **Number of points per degree**. Increases the number of calculations

per angular degree, improving resolution but slowing the reconstruction.

- **Number of events** to process. In general the greater the number of inputted Compton imaging events the better the fit and image quality.

A detailed description of the analytical image reconstruction algorithm can be found in [68].

Iterative

The iterative reconstruction algorithm developed at the University of Liverpool, is based on the Maximum Likelihood Expectation Maximization (MLEM) algorithm. The iterative reconstruction code creates the conics in the same way as the analytical code and is also implemented in C++ and uses Root. The principle of the iterative reconstruction algorithm is as follows:

1. Arbitrary starting state: randomly chose a point on cone surface.
2. Select 1st event.
3. Randomly move point to new location.
4. If new event density is greater, leave in new location, if not put back where it was.
5. Repeat for all events.
6. 1st iteration completed.

Unlike the analytical reconstruction algorithm, the iterative code used in this thesis, does not provide image visualiation or intensity profiles. Instead the code creates image files that are readable by the open source ImageJ software [69], which is designed for scientific multidimensional images. This software has been used in this thesis to create files which were then input to Matlab for analysis and visualisation. Iterative reconstruction algorithms

are computationally intensive and present problems with regards of iteration to the correct point, to find the true source distribution, particularly if the source distribution is spatially complex. This problem is explored in this thesis.

Chapter 5

Imaging Results and Analysis

The primary objectives of this thesis are to investigate the feasibility of multi-isotope imaging with ^{99m}Tc and ^{123}I using the ProSPECTus system and to assess the imaging performance of medical radioisotopes. Therefore, a range of data sets were acquired in order to optimise the image reconstruction parameters, determine the system efficiency and investigate the limitations of ProSPECTus. Unless otherwise stated, a coincidence window of 150 ns and digital thresholds of 8 keV and 90 keV in the scatter and absorber detector respectively were used for data acquisition. These parameters were chosen based on the work described in the previous chapters. In this chapter, the analysis of data collected from the following measurements will be presented:

- ^{139} Ce (166 keV) point like source (absorber 1 ProSPECTus configuration).
- ^{139} Ce (166 keV) point like source (absorber 2 ProSPECTus configuration).
- ^{99m}Tc (141 keV) and ^{123}I (159 keV) filled 16.4 mm diameter vial sources (absorber 2 ProSPECTus configuration).
- ^{99m}Tc, ^{123}I and ^{139}Ce 16.4 mm diameter vial sources, placed in the phantom (absorber 2 ProSPECTus configuration).

- Phantom populated with all 12 vials (16.4 mm -10 mm diameter) containing 8 x ^{99m}Tc and 4 x ^{123}I sources (absorber 2 ProSPECTus configuration).
- Each position of the phantom individually and sequentially populated for data acquisition, corresponding to a total of 12 measurements (absorber 2 configuration).

Quantitative interpretation of the results required the development of analytical methods, which is balanced by more qualitative interpretation of certain data sets. The methodology used will be introduced in this chapter with increasing complexity, due to the complex spatial radiation distributions reconstructed towards the end of the thesis.

5.0.10 ^{139}Ce Point Source Analysis

A ^{139}Ce point like source has been used to investigate the efficiency and intrinsic spatial resolution of the ProSPECTus system. A point-like source is ideal as it has negligible volumetric distribution, allowing the intrinsic performance to be established. The ^{139}Ce source was initially used to investigate image reconstruction parameters, particularly concerning optimising implementation of the iterative algorithm, as this was the first experimental project to use the algorithm. The iterative algorithm requires multi-parameter user input, which results in a complex optimisation problem. The approach described within is to process the data through the analytical reconstruction algorithm, then the more complex iterative reconstruction algorithm.

Image Reconstruction Investigations

The investigations to determine the optimum implementation of the image reconstruction algorithm utilised the ProSPECTus system configured with absorber 1. Coincidence data were acquired with a 0.2 MBq ^{139}Ce point source located 65 mm from the scatter cryostat, which corresponds to a Z-slice position of 160 mm. Figure 5.1 shows the image matrix as computed by the analytical reconstruction algorithm. The image matrix is visualised

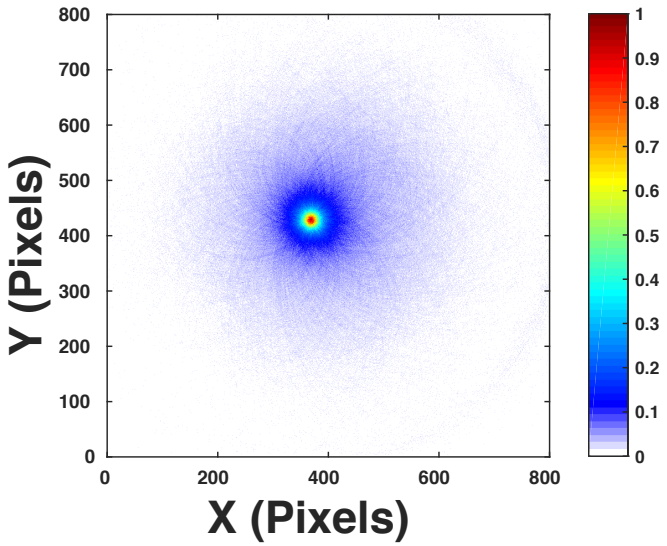

Figure 5.1: Analytical reconstruction of a ^{139}Ce point source generated by coincidence data acquired with absorber 1 ProSPECTus configuration. The image has been reconstructed at Z-slice 160 mm with a compression factor of 1.

using Matlab, where the x-y axes are defined in pixels and the z scale is normalised intensity. A compression factor of 1 was used in this image, which means each pixel represents 1 mm. In the analytical algorithm, the centre of the absorber detector position is translated to (400,400), to ensure the distribution is reconstructed in positive space. The region of highest intensity in the image produced in Figure 5.1, indicates the position of the ^{139}Ce point source, which is shown to be close to the centre of the absorber detector. The surrounding region of low intensity shows the surfaces of cones that do not correspond to the correct location of the source. This background region is a challenging factor in identification of sources in close proximity, which will be investigated in this chapter.

A method to determine the location of a point source in depth (Z) of imaging space has been previously formulated and validated in [48]. The

methodology consists of the following steps:

1. The number of counts in the maximum intensity pixel is recorded for a range of Z-slice values.

2. For the same range of Z values, the total number of counts in a complete image slice is recorded. These results are the background counts as they include the incorrect intersection of cone surfaces that arise due to the Compton scattering angle being known but not the direction of the incoming gamma ray.

3. The true source location in Z is found by plotting a normalised distribution of the number of counts in a pixel as a function of Z. The normalisation is calculated through dividing the values from step 1 by the values of step 2. The maximum point on the graph can be used to estimate the source location.

The image slice shown in Figure 5.1 was identified with the above methodology. The graph from step 3 in the methodology is shown in Figure 5.2a It can be seen that the optimum slice (maximum in the distribution) is located at 150 mm, which is 10 mm from the known source location. A GAMOS model of the detector system was used to investigate this discrepancy. Information on the gamma-ray interaction positions was extracted from the model, without the experimental uncertainties associated with using detector voxels. The results from the GAMOS model using exact interaction position in X,Y, Z for both detectors is shown in Figure 5.2b. It can be seen the maximum point and hence location in Z is calculated to be at the correct location of 160 mm. This suggests methods of improving the position beyond detector segmentation should be explored through PSA algorithms, which is a recommendation for future work from this thesis.

As described in Section 4.2.9, the intensity profiles for the analytical codes are fitted using a Lorentzian peak with a quadratic background. The intensity profiles in X and Y through the most intense pixel in Figure 5.1 are shown in Figure 5.3. The FWHM was calculated to be 25 mm and 24 mm in the X and Y directions, respectively. Since the distribution is for a point

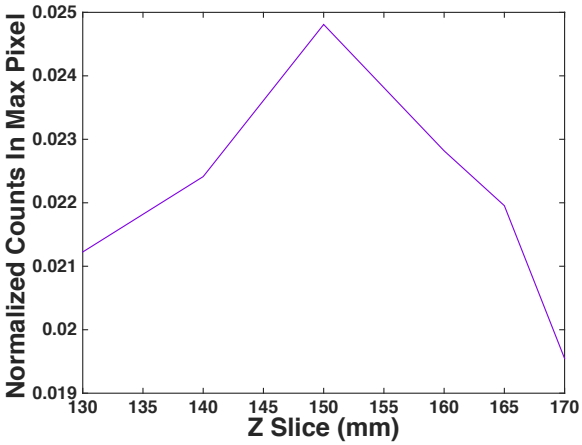

(a)

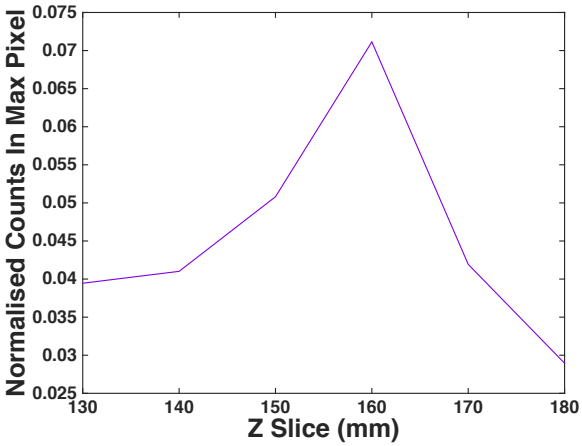

(b)

Figure 5.2: Graphs of the maximum number of cone intersections in a single voxel normalised to the total number of cone intersections in its image slice as a function of Z-slice (mm). This corresponds to a ^{139} Ce source placed 65 mm from the scatter cryostat of ProSPECTus configured with absorber 1, generated from (a) Experimental data and (b) GAMOS simulated data.

source located close to the centre of the field of view, the X and Y dimensions are consistent with each other within errors. Therefore, for all subsequent point source analysis only the X FWHM result will be quoted.

A spatial resolution of 25 mm is not deemed acceptable for clinical diagnosis, therefore the iterative algorithm was used to determine the improvement that can be achieved. As described previously, the iterative algorithm has a number of user input parameters, such as the number of iterations undertaken and image plane size, which impact upon the image produced. An image plane of 300x300 pixels was selected for all subsequent iterative reconstruction analysis, which has a centre of field of view located at (132,132) in (X,Y). Figure 5.4 shows the reconstructed point source images produced after 1, 10, 21 and 22 iterations. It can be seen in the image produced from iteration 22, that the algorithm breaks down at this point and does not produce a sensible image. Therefore, subsequent investigations were carried out until iteration 21 for the point source. Intensity profiles were created through the point of maximum intensity in order to be comparable to the analytical reconstruction algorithm. It was found that the profile generated up to iteration 2 was best fitted with a Lorentzian peak on a quadratic background, which is what is used to fit the profiles from the analytical reconstruction. However, this fit does not work well after iteration 2 due to the background counts in the image diminishing as the iteration number increases. A number of alternative fitting functions were investigated and it was determined that a Gaussian peak best fitted the reconstructed data from iteration 3 onwards. Figure 5.5 shows the data and corresponding fits for iteration 1 with Lorentzian fit including quadratic background and iteration 10 with a Gaussian fit. The peaks were fitted in this thesis using Matlab, which outputs R-square, a measure of how successful the fit is in representing the data. The R square calculated for the fit in Figure5.5a, is 0.99 and for Figure 5.5b 0.98, which means that the fits represents 99% and 98% of the total variation in the data about the average, respectively. Therefore, the FWHM for the first 2 iterative reconstructions were taken from a Lorentzian fitted profile in X and all subsequent reconstructions with a Gaussian profile. The results for FWHM as a function of iteration number is shown in Figure 5.6. It can be

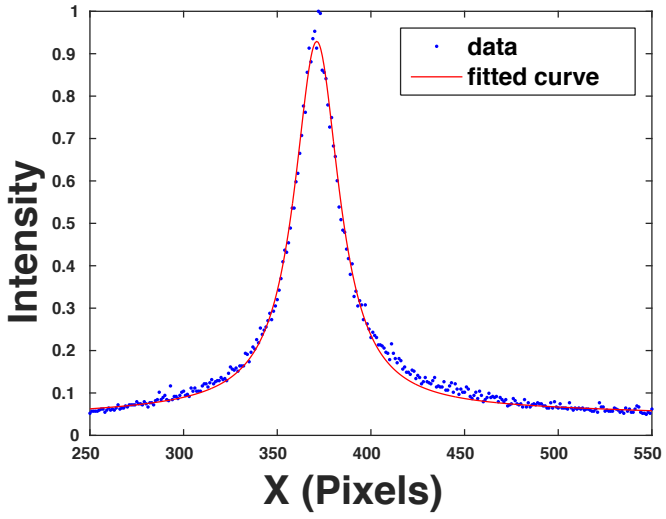

(a)

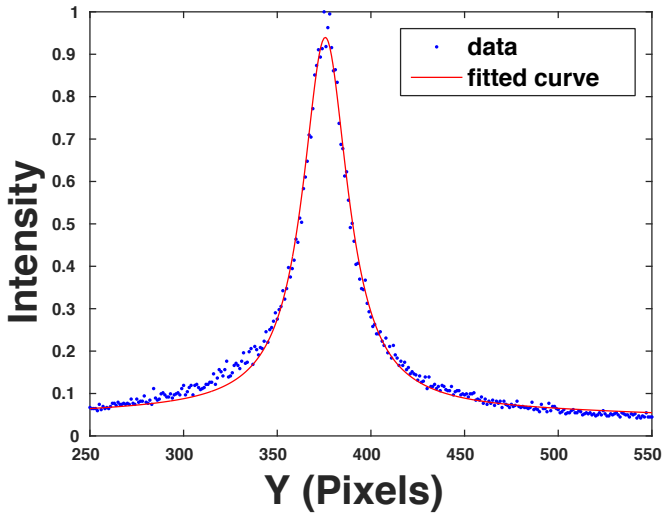

(b)

Figure 5.3: Intensity profiles of the ^{139}Ce point source measurement acquired with the ProSPECTus absorber 1 configuration. (a) X-intensity profile and (b) Y-intensity profile, through point of maximum intensity.

seen that the FWHM decreases from 25 mm (equivalent to the analytical reconstruction result) to 3mm, with the most significant improvement observed between iteration 1 and 4.

Therefore it is concluded that the spatial resolution of the ProSPECTus system, as quantified for a ^{139}Ce source placed at Z=160 mm, is 25 mm and 3 mm, when using the analytical and iterative reconstruction algorithms, respectively. It is evident that although the analytical algorithm is not suitable for clinical practice, the iterative result is extremely promising. It should be noted however that the intrinsic spatial resolution is dependent on the source to detector geometry, system geometry, position of the source within the field of view and other experimental factors.

The absolute efficiency has been calculated for the ProSPECTus system, with the absorber 2 configuration, using a ^{139}Ce point source of activity 16727 Bq, that was placed 40 mm from the scatter detector cryostat. Coincidence data was acquired for a total of 24608 seconds. The efficiency was determined for the following types of gamma-ray events:

- All coincidence data events: corresponding to gamma-rays which interact at least once in each detector but do not necessarily deposit all their energy. Without full energy deposition it is not possible to utilise the event, due to the inability to gate on energy.

- Fully absorbed events of all folds: as it is possible to gate on the photopeak, those gamma rays that interact at least once in the scatter or absorber detector can potentially be used for image reconstruction but currently if there is more than 1 interaction in each detector the events are vetoed as further developments would be required in the reconstruction algorithm.

- Fully absorbed Fold[1,1,1,1] events: corresponding to one interaction in each detector, in which all energy is deposited. These are used in this thesis for image reconstruction.

As discussed in Section 3.5.4, the Compton imaging efficiency is calculated relative to the number of incident gamma rays on the detector. The number

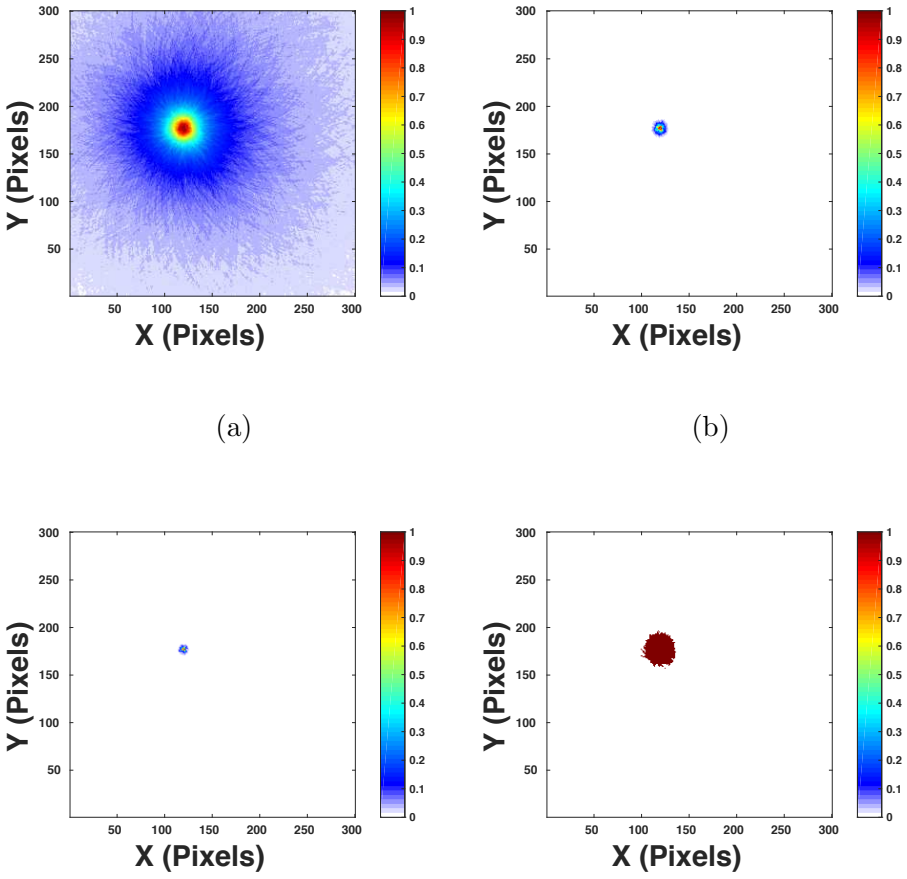

(a) (b)

(c) (d)

Figure 5.4: Iterative reconstruction images of a ^{139}Ce point source, produced after (a) 1 (b) 10 (c) 21 and (d) 22 iterations. All images are reconstructed at a Z-slice of 160 mm and are reconstructed with a compression factor of 1.

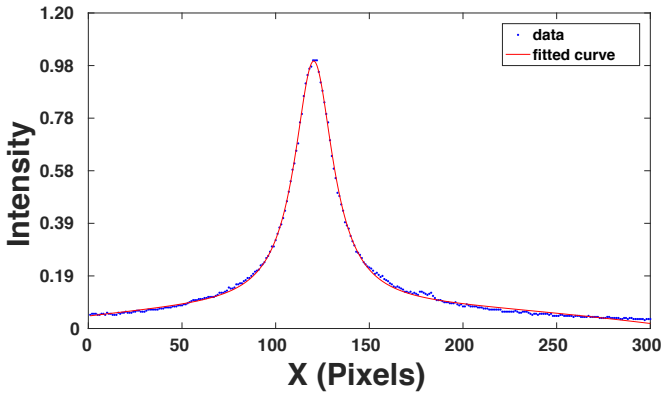

(a)

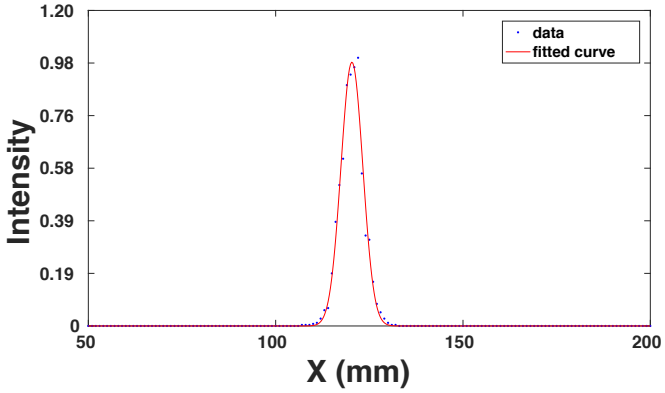

(b)

Figure 5.5: (a) 1st reconstruction with Lorentzian peak fit with quadratic background fit to data and (b) 10th reconstruction with Gaussian fit to data.

of gamma rays incident from the ^{139}Ce source, on to the front face of the scatter detector is calculated through the equation:

$$N_{incident} = A.L_T.P_\gamma.\Omega \tag{5.1}$$

where A is the Activity in Bq of the source, L_T is the the total time of measurement, P_γ is the branching ratio i.e. the probability of a particular gamma ray emission occurring, which is 80 % for the 166 keV of ^{139}Ce and Ω is the solid angle subtended by the scatter detector in relation to the point source. The solid angle Ω was calculated for this measurement to be 0.118 from the following equation:

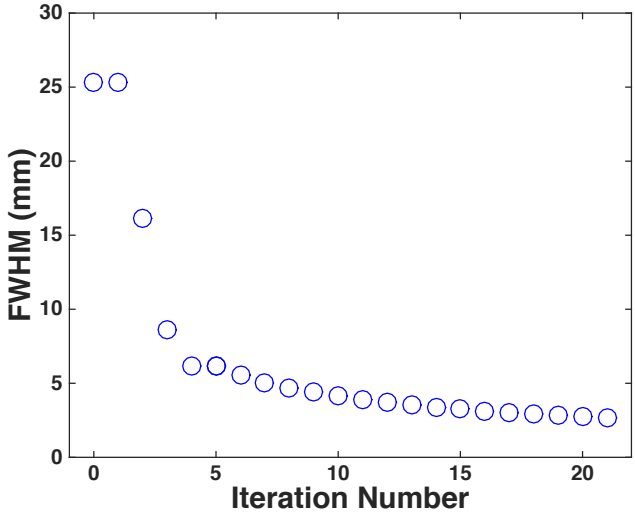

Figure 5.6: Plot of FWHM as a function of iteration number for a ^{139}Ce point source. Iteration 0 is from the analytical reconstruction algorithm and is included in this plot for completeness. All images for these results were reconstructed with a compression factor of 1 at a Z-slice of 160 mm.

$$\Omega = \frac{2\pi}{4\pi}\left(1 - \frac{r_2}{\sqrt{r_2^2 + r_1^2}}\right) \tag{5.2}$$

where r_1 is the radius of the scatter detector (3.55 cm) and r_2 is the distance of the point source to the scatter detector (4.21 cm). The number of incident gamma rays ($N_{incident}$) on the scatter detector, was therefore calculated to be 3.89 x 10^{07}. The efficiency values (ϵ) for ProSPECTus are given in Table 5.1 and were calculated using:

$$Efficiency = \frac{100XN_{eventtype}}{N_{incident}} \tag{5.3}$$

The typical efficiency of SPECT for incident gamma rays is 0.027%, for a low energy general purpose collimator with a gamma ray source of 150 keV placed 10 cm from the collimator. Therefore, as can be seen in Table 5.1, the prototype ProSPECTus system is currently operating with an improved efficiency over conventional SPECT systems by up to a factor of 2.50 when using fully adsorbed Fold[1,1,1,1] events. It is expected that the next genera-

Event Type	Number of Events	Efficiency %	ProSPECTus:SPECT Efficiency
Fully Absorbed Fold [1,1,1,1]	26226	0.067	2.50
Fully Absorbed All Fold Types	34939	0.090	3.33
All Energies All Fold Types	158726	0.408	15.13

Table 5.1: Efficiency results for the different event types discussed, also quoted is the improvement over conventional SPECT systems.

tion ProSPECTus system will achieve a greater improvement as experimental setup parameters will have accounted for some of the efficiency loss of this system. These parameters are : the three strips of the scatter detector that were not instrumented, which make up $\sim$ 12% of the scatter surface, the 8 keV threshold in the scatter detector has been calculated through GAMOS simulations to account for $\sim$ 60% of incident Fold[1,1,1,1] events, the misalignment offset of the scatter and absorber detector that was discovered after data measurements, which is discussed in the next section and also the loss of the events to the cryostat (expected 2.5 times increase in efficiency when using a single cryostat for both detectors). If these factors are resolved it is expected that the ProSPECTus system could achieve a factor of 17.2 times improvement in efficiency over conventional SPECT systems. In addition developing algorithms that can reconstruct the path of gamma-rays that have undergone multiple interactions with each detector (i.e. all folds) would allow for a factor 23 improvement. Therefore it is a recommendation of this thesis to develop the algorithms for reconstruction of data from all folds and to operate the next generation ProSPECTus detectors with lower thresholds in the scatter detector.

5.0.11 ^{99m}Tc and ^{123}I 16.4 mm Diameter Vials

The feasibility of using the ProSPECTus system to acquire data simultaneously from mutiple medical radioisotopes has been investigated. As stated previously, this would facilitate studying two physiological processes in one

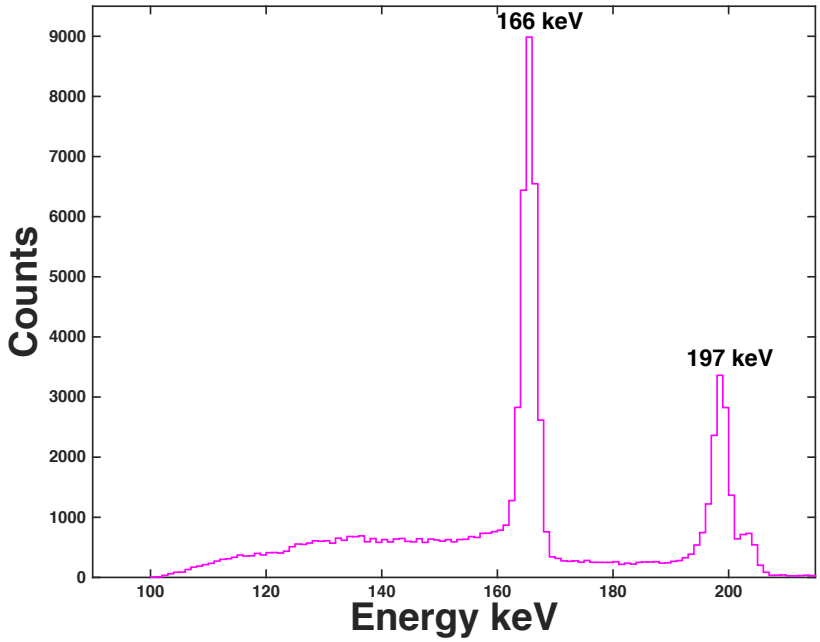

Figure 5.7: DC Fold[1,1,1,1] addback spectrum collected from a ^{139}Ce point source placed 40 mm from the detector cryostat. This measurement was used to determine the efficiency of the ProSPECTus system.

scan, which requires a system with good energy and spatial resolution. Volumetric sources were chosen for this experimental work, to better represent the clinical application. The first set of measurements used the two commonly used SPECT radioisotopes ^{99m}Tc and ^{123}I, for the simplest case of imaging two hot volumes in the field of view. The isotope solutions were placed into two separate 16.4 mm diameter vials from the ProSPECTus phantom, with total activities of 0.11 MBq and 0.55 MBq for the ^{99m}Tc and ^{123}I vials, respectively. These activities were determined by knowing the activity at time 0 corresponding to calibration at the Royal Liverpool University Hospital, for the total solution volume of ^{99m}Tc and ^{123}I. Activity as a function of time was then calculated to generate activity decay curves for the total volume procured from the Royal Liverpool University hospital and for the individual vial volumes. Figures 5.8 show the total activity curves for each isotope and 5.8b shows the curve specific to vial activities of the 16.4 mm and 10 mm diameter size vials only, for ^{99m}Tc and ^{123}I. The activity calculations per vial were used to calculate the time that each measurement would need to acquire 10,000 Fold[1,1,1,1] events, as efficiency had been calculated from the previous section. It has been found through preliminary investigations that 10,000 events is sufficient for the analytical image reconstruction algorithm to provide an image with a FWHM independent of imaging statistics. The iterative algorithm relies on as many counts as possible to improve its accuracy but it was found that 10,000 events was a viable trade off between time of measurement and number of events due to the relatively short half lives of ^{99m}Tc and ^{123}I. The two vials were placed in front of the scatter detector, equidistant from its centre as shown in Figure 5.9. The vials had a centre to centre separation of 60 mm, which corresponds to a distance of 44 mm between the closest edges. This separation was chosen because the position resolution of a point source was determined to be 25 mm in the previous section, which gave confidence in the systems ability to resolve the vials at the chosen distance, when using both image reconstruction algorithms.

The first set of data were acquired with the detectors operated in 'singles' mode i.e with no coincidence requirement. This allowed individual energy spectra from ^{99m}Tc and ^{123}I to be obtained separately, for calibration pur-

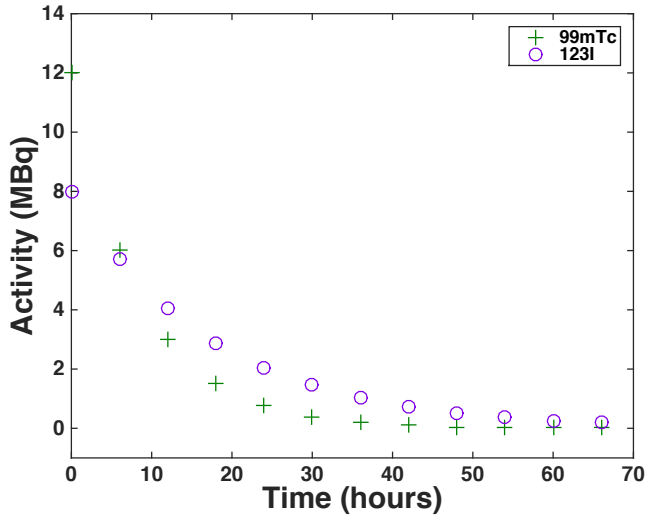

(a)

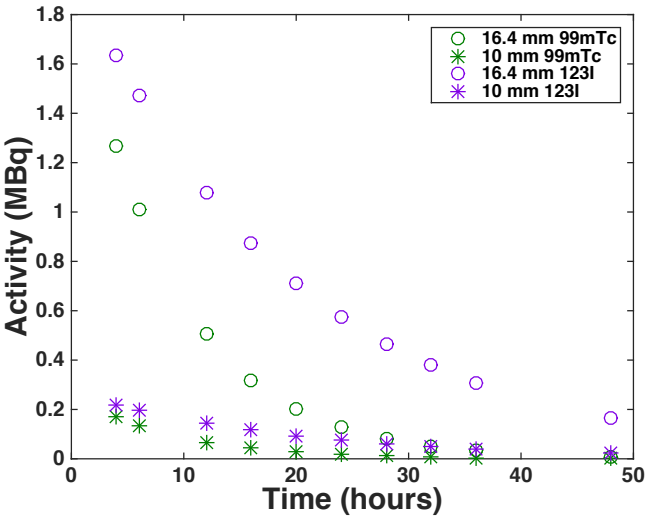

(b)

Figure 5.8: Calculated activity of (a) The total volume of the radiation sources calibrated from time 0 at the Royal Liverpool University Hospital (b) The individual 16.4 mm vial and 10 mm diameter vial for ^{99m}Tc and ^{123}I from the time of the first coincidence data measurement.

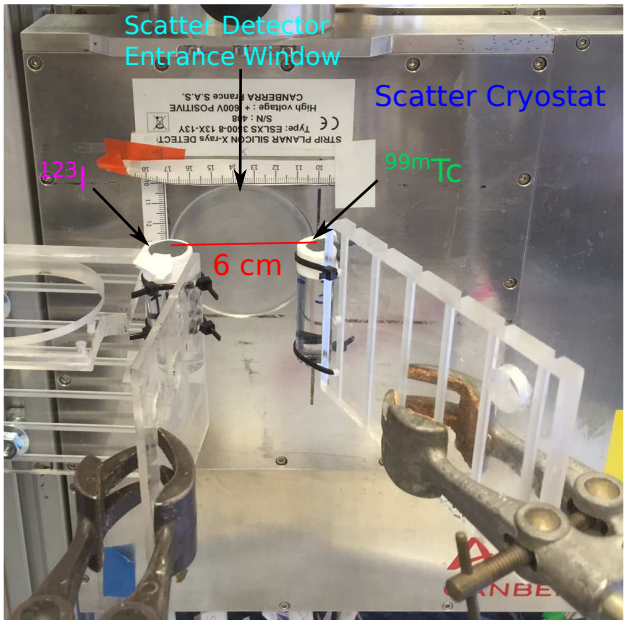

Figure 5.9: Photograph of the 16.4 mm diameter vials filled with ^{99m}Tc and ^{123}I placed 6 cm apart (centre to centre), during data acquisition.

poses. Acquiring data for the vials separately also allowed their isotope dependent response to be observed more easily and for the energy resolution to be measured at the gamma ray energies of 141 keV and 159 keV. Data were acquired from the vials sequentially for 16.1 minutes for the ^{123}I vial and 15.78 minutes for the ^{99m}Tc vial. During which 1476 $\pm$ 38 and 54132 $\pm$ 233 total singles events were detected in the scatter and absorber detectors, respectively. For the ^{99m}Tc vial 735 $\pm$ 27 and 15908 $\pm$ 126 total fully absorbed singles events were detected in the scatter and absorber detectors, respectively. The energy spectra of ^{99m}Tc acquired in strip AC07 of the scatter detector and the absorber 2 detector are shown in Figure 5.10. The energy resolution (FWHM) was determined from Gaussian fits of the 141 keV photopeak to be 1.99 keV and 2.12 keV for the scatter and absorber 2 detector, respectively. Figure 5.11 shows the energy spectra acquired for the ^{123}I vial by strip AC07 of the scatter and absorber 2 detectors. The x-rays of energy 27.2 keV and 31 keV emitted from the ^{123}I source can be seen in the scatter energy spectrum shown in Figure 5.11a, but are not observable in the ab-

sorber 2 spectrum due to the digital hardware threshold which was set at 90 keV in preparation for coincidence data acquisition. The energy resolutions determined by a Gaussian fit of the of 159 keV photopeak were 2.01 keV and 2.15 keV for the scatter and absorber 2 detectors respectively. These results are in agreement with the energy resolution measurements shown in Section 4.2.2 and demonstrate the excellent spectroscopic performance achievable with the semiconductor detectors used in the ProSPECTus project.

The digital acquisition system was subsequently set to collect data in coincidence mode. Data were acquired with both 16.4 mm diameter ^{99m}Tc and ^{123}I vials simultaneously for 13.82 minutes and then the ^{123}I vial removed and data acquired for a further 42.1 minutes with the ^{99m}Tc vial only, in order to obtain equal Fold [1,1,1,1] events. The data were processed, using the methods described in Section 4.2.4 to select the events of interest for Compton imaging. The energy spectrum for these selected events is shown in Figure 5.12. The plot shows the distribution of energy deposits in the scatter and absorber 2 detector individually, for separate measurements of the ^{99m}Tc vial and ^{123}I vial. It can be seen that the distribution in the scatter detector starts at 8 keV, quickly rising to a maximum before falling away to a maximum energy of 50 keV and 65 keV for the ^{99m}Tc and ^{123}I spectra, respectively. The low energy cut off is due to the threshold for data acquisition being set to 8 keV in the scatter detector. The corresponding threshold in the absorber 2 detector is 90 keV, thus no data is recorded in the detector at lower energies. The energy distribution in the absorber is almost symmetrical to the scatter detector, with a rise to a maximum. Note, the maximum energy recorded in the absorber detector is 8keV below the photopeak energy, due to the threshold in the scatter detector. It is clear that application of the thresholds therefore reduces the Compton imaging efficiency. Thus, data were produced using a GAMOS Monte-Carlo model of the ProSPECTus detector configuration to estimate the theoretical loss of events due to experimental thresholds. Figure 5.13 shows the Fold[1,1,1,1] coincidence energy deposits for fully absorbed 141 keV and 159 keV incident gamma rays from ^{99m}Tc and ^{123}I, as output from the GAMOS model. No thresholds were set in the simulations and it was therefore calculated that for

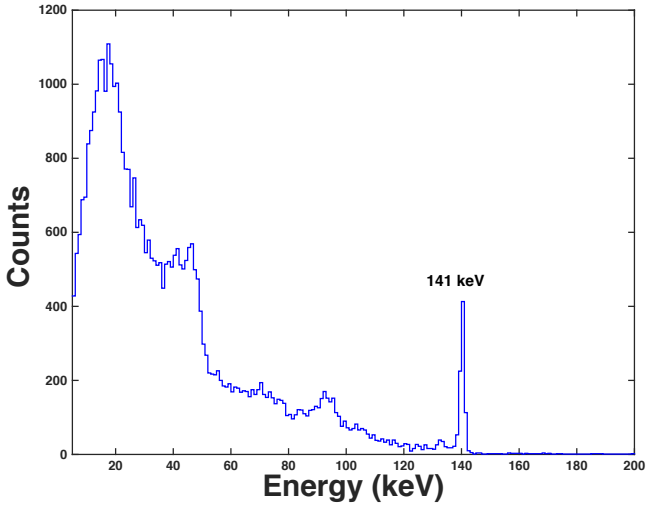

(a)

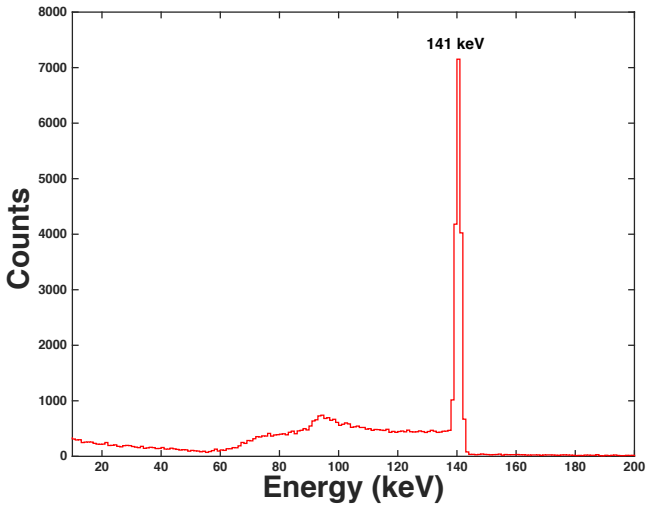

(b)

Figure 5.10: ^{99m}Tc energy spectra acquired with the CAEN cards set in 'singles' modes for (a) strip AC07 of the scatter detector and (b) strip AC07 of the absorber 2 detector.

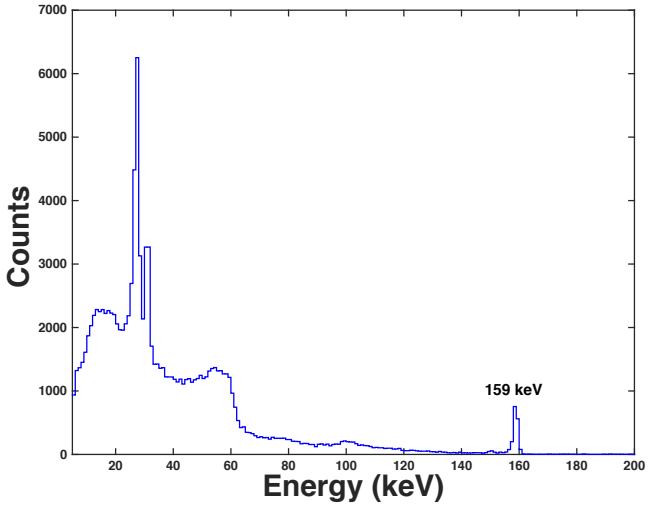

(a)

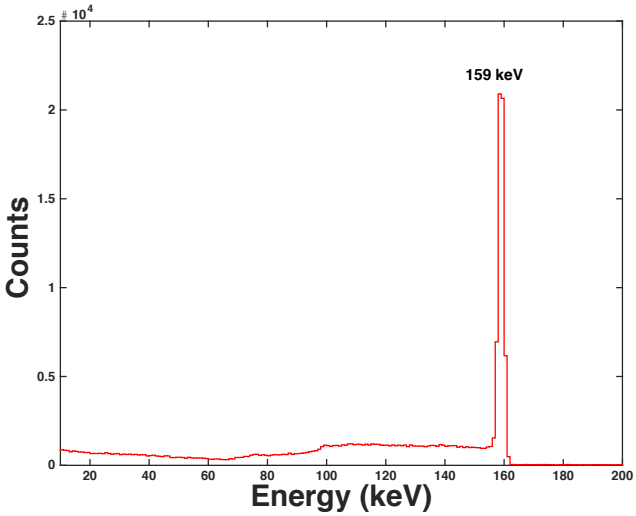

(b)

Figure 5.11: ^{123}I energy spectra acquired with the CAEN cards set in 'singles' modes for (a) strip AC07 of the scatter detector and (b) strip AC07 of the absorber 2 detector.

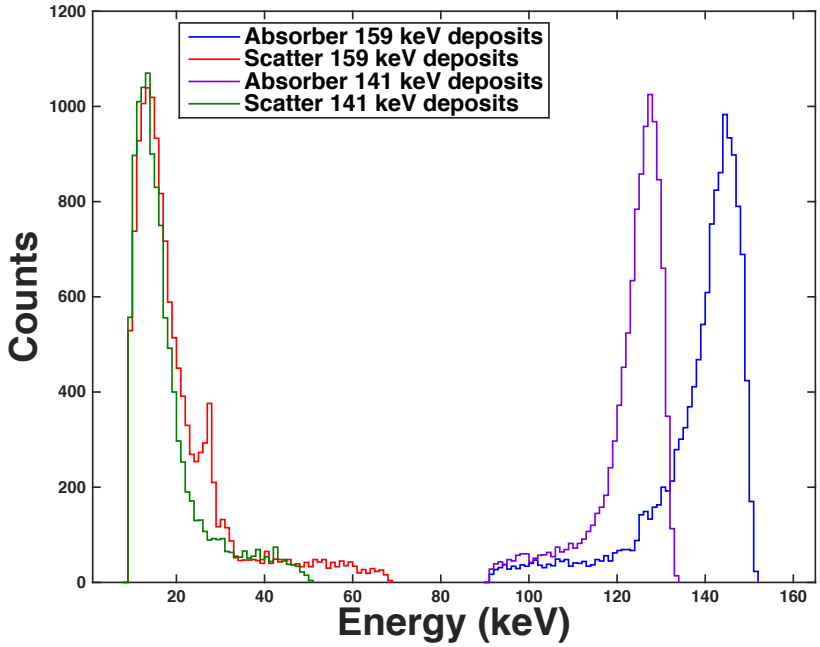

Figure 5.12: Experimentally acquired energy spectrum showing the energy deposited from the fully absorbed Fold [1,1,1,1] events in the scatter detector and absorber 2 detector for incident gamma rays from ^{99m}Tc and ^{123}I.

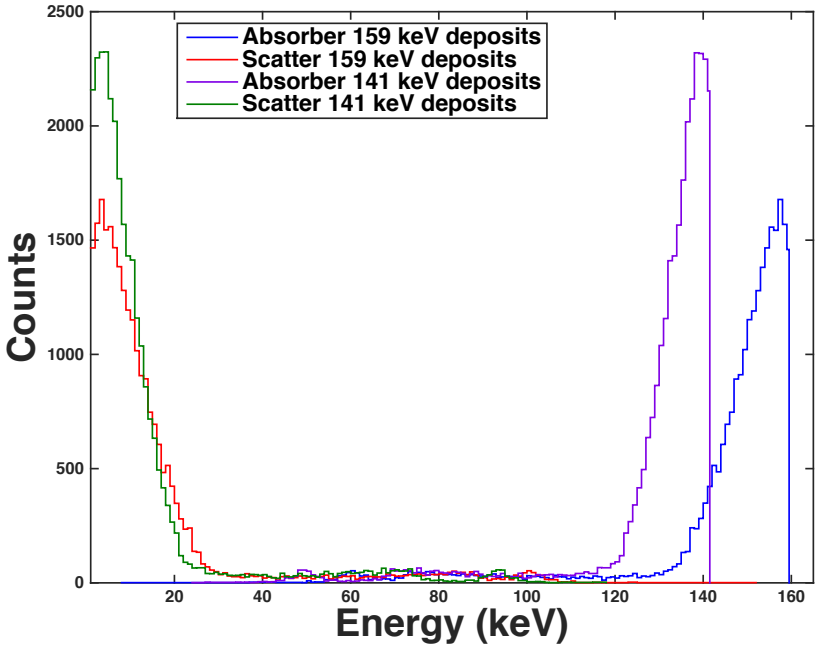

Figure 5.13: GAMOS simulated fully absorbed coincidence Fold[1,1,1,1] energy deposits expected in the scatter detector and absorber 2 detector for incident gamma rays of ^{99m}Tc and ^{123}I.

^{99m}Tc, the experimental thresholds used in these measurements corresponds to a loss of 58 % and 5 % of Fold[1,1,1,1] events, in the scatter and absorber detector, respectively. Similarly for the ^{123}I data, there is a loss of 49 % and 8 % events. Although this will not significantly impact on the current investigation of multi-isotope imaging, it would not be desirable to operate the system in clinical applications with such significant data loss. It is therefore recommended in future data acquisition that further work is undertaken to reduce the thresholds.

Coincidence data were acquired so that approximately 10,000 counts were recorded in the ^{99m}Tc (141 keV) and ^{123}I (159 keV) photopeaks, as shown in the acquired add-back spectrum in Figure 5.14. This data were acquired with the vials in place simultaneously, however, due to the higher activity of the ^{123}I source, it was removed 14 minutes into data acquisition, and data were acquired with the ^{99m}Tc vial for an additional 43 minutes. This decision

was made because activity calculations revealed these counting times would be sufficient to collect equal and statistically significant counts in both of the photopeaks. The 141 keV photopeak contains 11284 ± 106 gross counts and the 159 keV photopeak contains 12316 ± 111 gross counts. It can be seen in the addback spectrum of Figure 5.14 that the 141 keV and 159 keV photopeaks are easily resolvable and that the application of experimental threshold results in significant data loss below 90 keV. A photopeak at 185 keV is also observed in the spectrum, which arises from coincident events corresponding to the 159 keV gamma ray and one of the 27.2 and 31 keV x-rays incident from the ^{123}I source. The energy resolution calculated for the photopeaks at 141 keV and 159 keV is 2.84 keV and 2.81 keV respectively. This result demonstrates that the ProSPECTus system is capable of resolving the energies of ^{99m}Tc and ^{123}I during simultaneous data acquisition.

A Na(Tl) scintillator crystal of dimension (2x2x2) inch with PMT readout was setup alongside the ProSPECTus system in order to acquire multi isotope data with ^{99m}Tc and ^{123}I. The aim of this measurement was to illustrate the comparable performance, in terms of energy resolvability, with that typically observed in clinical imaging systems. The acquired energy spectrum is shown in Figure 5.15. It can be seen that the two photopeaks of 141 keV and 159 keV are not easily resolvable, such that complex deconvolution techniques would be required for the analysis of the photopeak energy resolution. The 27.40 keV and 31.70 keV x-ray peaks from ^{123}I can be seen represented by a single peak in the energy spectrum with a combined energy resolution of 7.61 keV. It would be expected that clinical SPECT systems would have even poorer resolvability due to the increased crystal size used in gamma cameras and the use of a greater number of PMT's. The degradation in energy resolution would be as a result of the increased likelihood of mispositioned signals i.e cross talk between PMT's.

The selected events from the ProSPECTus coincidence data acquired and plotted in Figure 5.14 were input to the analytical reconstruction algorithm. A compression factor of 2 was selected and the resulting image is shown in Figure 5.16a. This image is reconstructed at a Z-slice of 166 mm, which is where the vials were placed during data acquisition. The position and ra-

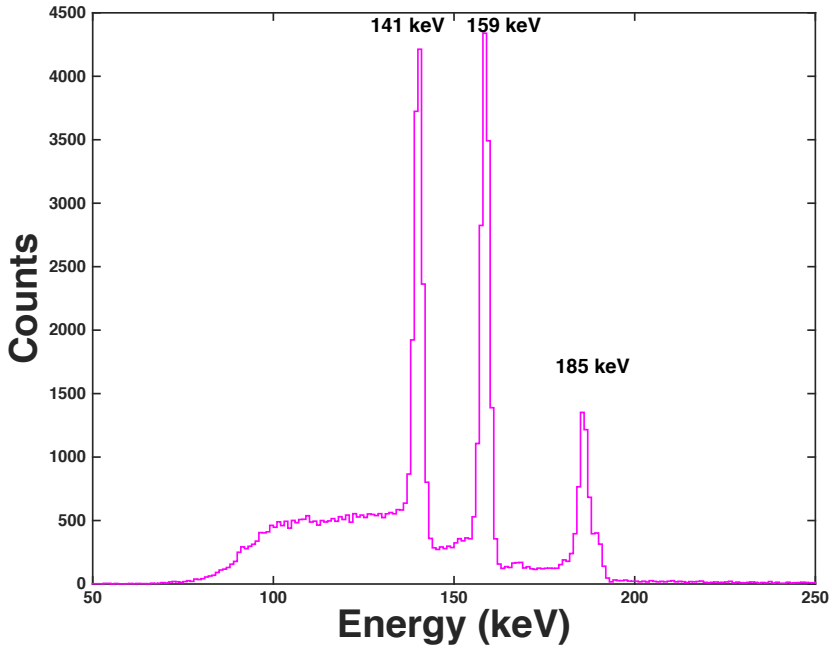

Figure 5.14: Gamma-ray energy spectrum collected during data acquisition of the the two 16.4 mm diameter vials containing ^{99m}Tc and ^{123}I. The energy resolution calculated at 141 keV and 159 keV was 2.82 keV and 2.80 keV, respectively. The 185 keV peak arises due to coincidences between the 159 keV gamma ray and 27 keV x-rays of ^{123}I.

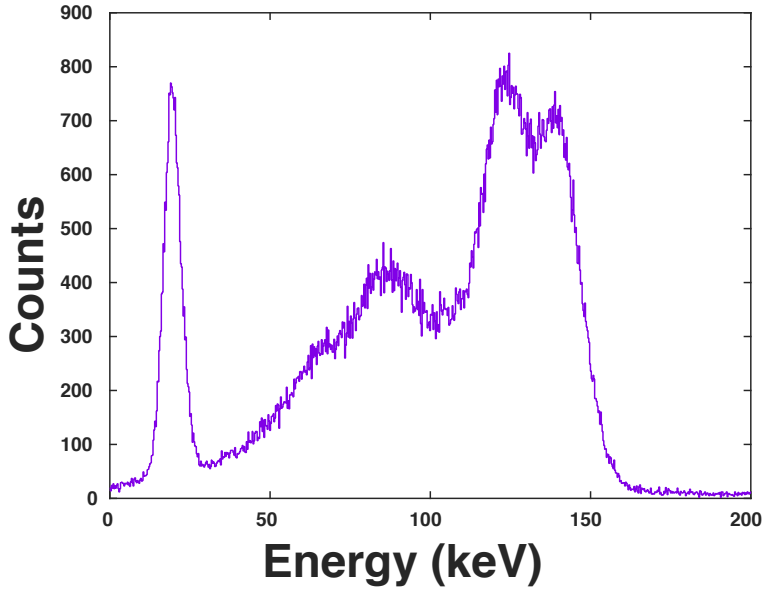

Figure 5.15: Energy spectrum acquired with Na(Tl) detector for incident gamma rays energies of 141 keV and 159 keV from ^{99m}Tc and ^{123}I respectively.

dioisotope distribution of the two vials can be seen in the image. In order to investigate the distribution quantitatively, an intensity profile through the point of maximum intensity, corresponding to Y=400, has been plotted and shown in Figure 5.16b. The image and corresponding intensity show that the ^{123}I vial (right distribution) is more intense by $\sim$ 20%. This discrepancy is worse than expected as it was calculated that the number of counts accumulated for each peak differ by only $\sim$ 8%. Subsequent investigations of the parameters that could produce this effect revealed that there was a translational offset in the mechanical alignment of the two detector X-Y centres. The detectors are now known to be aligned so that the centre of the scatter detector is offset by 11 mm in the positive X direction in relation to the centre of the absorber detector. Therefore, during data acquisition the ^{123}I vial was closer to the centre of the field of view than the ^{99m}Tc vial. However, in the defined coordinate system of the analytical reconstruction, the central position in the image matrix (X=400 pixel, Y=400 pixel) is representative of the middle of the scatter detector, not the field of view. It is therefore expected

that the centre of the ^{99m}Tc and ^{123}I vials should be located at X= 385 pixel and X = 415 pixel in the image matrix as each pixel represents 2 mm. The maximum point of intensity is used to locate the positions of the vials shown in Figure 5.16b, it is found that the maximum points of intensity and hence vials are located at at X=385 pixel and X= 415 pixel. This demonstrates that the sources are correctly reconstructed to their true location in space.

Now that it is known that the sources are not located equidistant in the field of view, the discrepency of intensity between the two vials of $\sim$ 20%, rather than $\sim$ 8% can be further investigated. Indeed, it is known that the sensitivity in the field of view of a Compton camera changes as a function of position. This phenomenon has been the focus of another Liverpool Compton imaging project where GAMOS simulations and experimental data were used to create a correction function $f(x, y, z)$ to compensate for the variation in sensitivity as a function of position. The correction function is defined as:

$$f(x, y, z) = ax^2 + by^2 + cz^2 + d \tag{5.4}$$

where the position coefficients are energy dependent. This correction function $f(x, y, z)$ has been incorporated into the analytical imaging reconstruction by way of a normalisation matrix where the user can define the X,Y and Z coefficients of the function. Figure 5.17 is a plot of the inverse sensitivity matrix used to normalise the analytical image by multiplying the image matrix in Figure 5.16a by this inverse sentivity matrix in order to achieve accurate representative intensity in the ^{99m}Tc and ^{123}I vials. Figure 5.18a shows the resulting image and Figure 5.18b displays the corrected intensity profile. It can be seen that there is an improvement in the sensitivity of the ^{99m}Tc vial from 80 % intensity to 90 % intensity to that of the ^{123}I vial, which indicates that the application of the field of view sensitivity correction has been successful.

The sensitivity variation of the field of the view has a more profound effect when data is processed by the iterative reconstruction algorithm. As the iteration number increases, a larger fraction of the counts are attributed to the most intense activity regions, which in this measurement is the ^{123}I

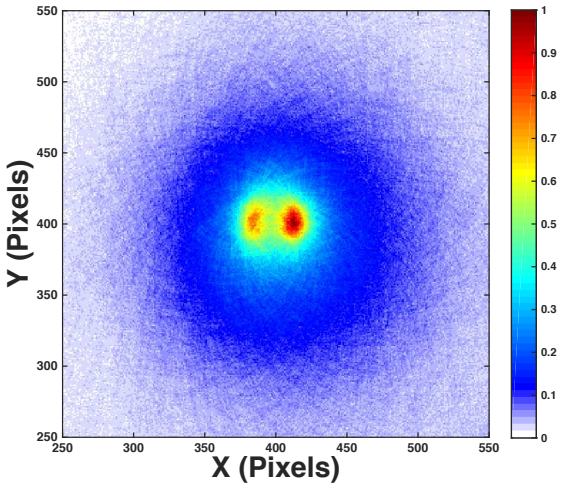

(a)

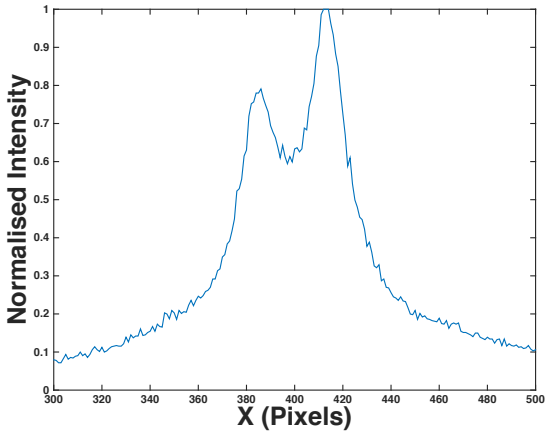

(b)

Figure 5.16: (a) An image of the 16.4 mm diameter ^{99m}Tc and ^{123}I vials placed parallel to scatter the cryostat, produced by analytical reconstruction and (b) the X Intensity profile through point of maximum intensity in the corresponding image. A compression factor of 2 was used in image reconstruction therefore each pixel represents 2 mm in phase space.

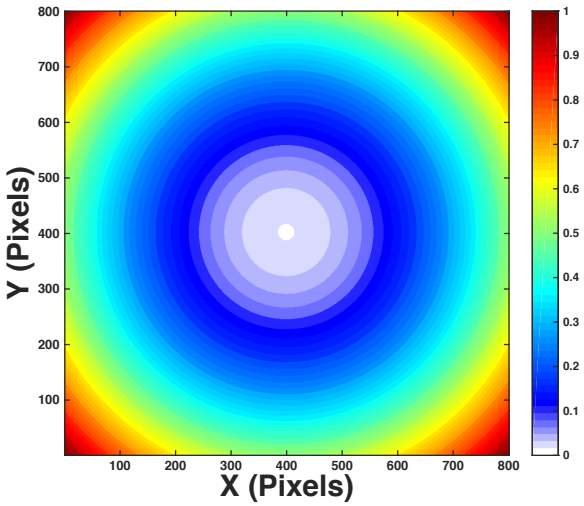

Figure 5.17: Inverse sensitivity matrix, used to normalise the sensitivity in the ProSPECTus field of view as a function of position at a fixed Z position. The centre of this matrix was repositioned to X= 411 pixel in order to compensate for the detector offset.

vial. As iterations increase, the eventual result is that the ^{99m}Tc vial is no longer easily visible. Figure 5.19 is a graphical representation of how the intensity of the ^{99m}Tc vial relative to the ^{123}I vial diminishes as a function of iteration number. It can be seen that by iteration 4, the ^{99m}Tc intensity is 45 % of the ^{123}I vial and by iteration 11 it has dropped to below 10 %. Figure 5.20 shows the visual effect of the reduced intensity in the images that are reconstructed at iteration 2, 6 and 12 with the corresponding X-intensity profile. To investigate this phenomena and quantify the resolution, the 3rd iteration reconstructed image as shown in Figure 5.21a is used for analysis. In this image, both vials can be distinguished and the ^{123}I vial is $\sim$ 50 % more intense than the ^{99m}Tc vial. To deconvolve the field of view influence, the data acquired simultaneously from ^{99m}Tc and ^{123}I vials was reconstructed by gating on the energies of 135 keV -144 keV and 151 keV-161 keV respectively, prior to inputting the data to the iterative reconstruction algorithm. This allows the vials of different isotopes to be selected individually. The 3rd iteration of the individual vial images of ^{99m}Tc and ^{123}I are

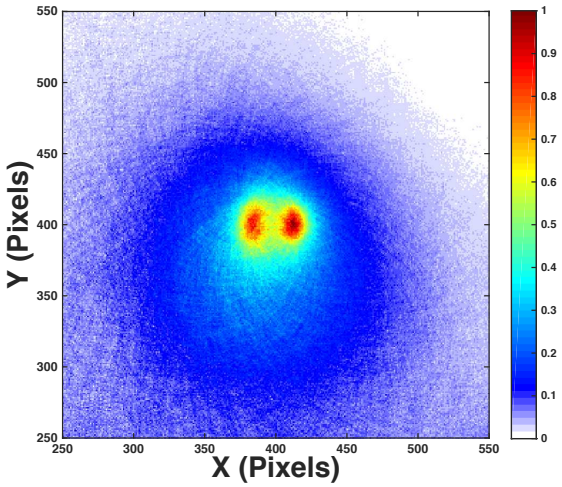

(a)

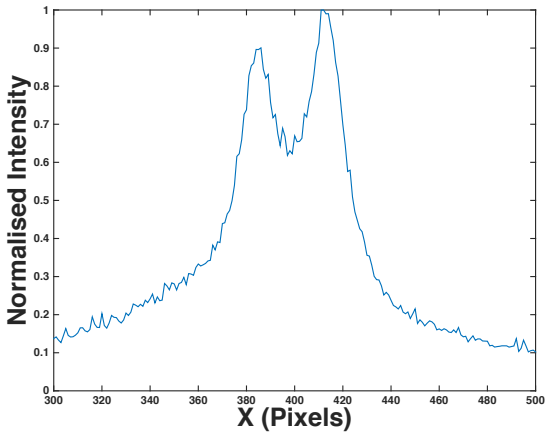

(b)

Figure 5.18: (a) Image of ^{99m}Tc and ^{123}I reconstructed with the analytical reconstruction algorithm and with field of view sensitivity normalisation. (b) X-intensity profile through point of maximum intensity in image (a).

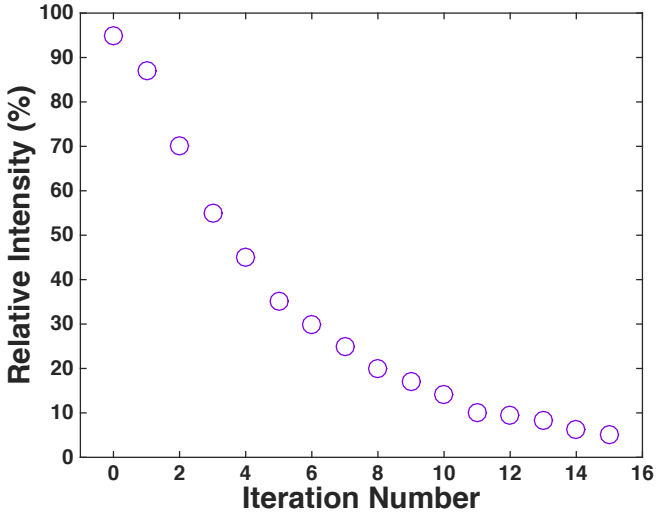

Figure 5.19: Graph displaying the percentage of the intensity in the ^{99m}Tc vial to that of the ^{123}I vial as a function of iteration number.

shown in Figures 5.22 and 5.23, respectively. In Figure 5.22 the ^{99m}Tc vial is located at (X=117 Y=133) pixels as determined by the maximum of the intensity profile and with the same methodology in Figure 5.23 the ^{123}I vial is located at (X=148,Y=132) pixel. These energy gated reconstructed images were then superimposed onto one image matrix using Matlab as presented in Figure 5.24a. This image shows the distributions to have a more similar intensity, as the issue of counts being incorrectly assigned by the iterative reconstruction technique is avoided. The corresponding X-intensity profile is shown in Figure 5.24b and it can be seen that the individual vials are of approximately equal intensity. This image would ideally be produced directly from the reconstruction algorithm, without the requirement to superimpose the separate data sets. Therefore, developments are currently in progress to incorporate a probability matrix in the iterative algorithm in order to achieve this, which is an important recommendation of this thesis.

Analysis of the data in Figure 5.24 indicates that the vials have been reconstructed to the correct location. The maximum point of intensity for the ^{99m}Tc and ^{123}I vials is at X=117 and X=148 pixels. The coordinate system is such that the centre of the scatter detector is represented in the iterative

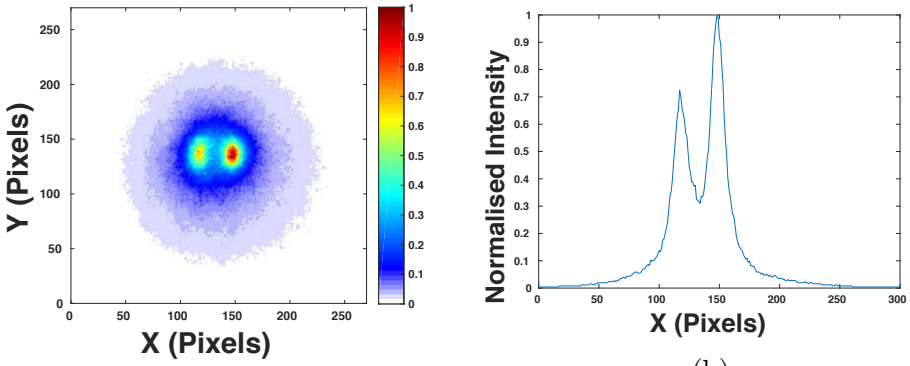

(a)

(b)

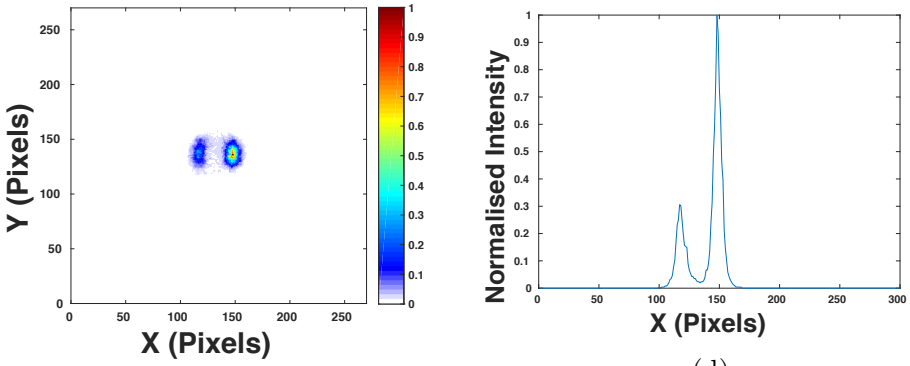

(c)

(d)

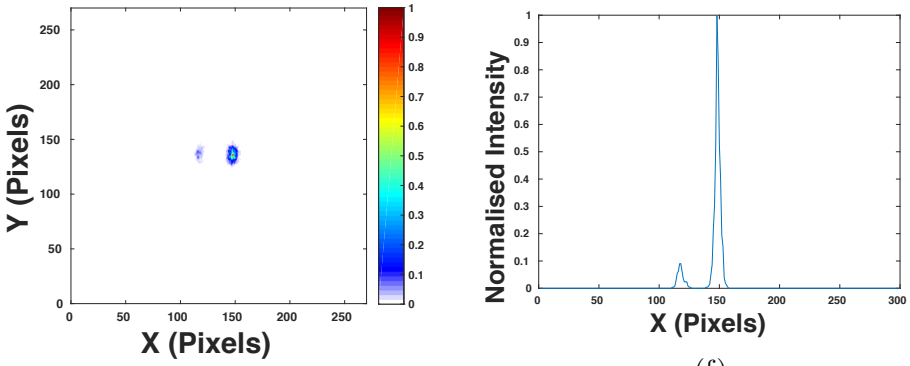

(e)

(f)

Figure 5.20: Iterative reconstruction images of the parallel ^{99m}Tc and ^{123}I vial at the (a) 2nd iteration (c) 6th iteration and (f) 12th iteration. The corresponding X-intensity profiles are given in figures (b), (d) and (e) respectively.

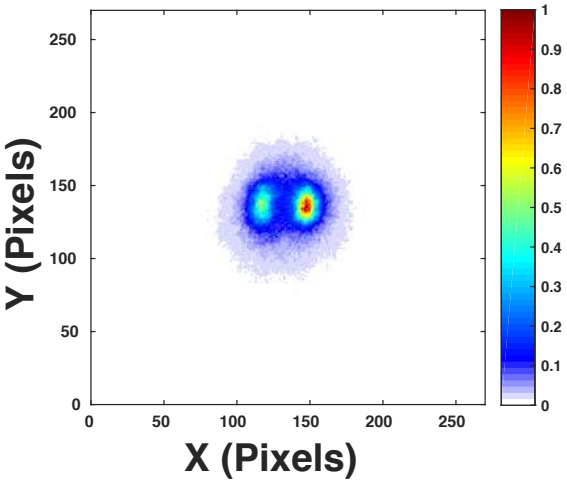

(a)

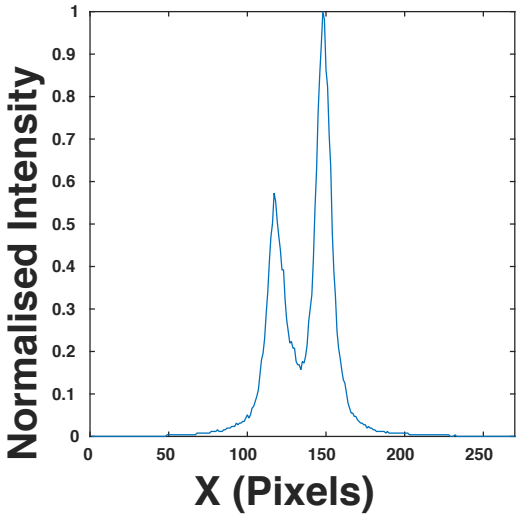

(b)

Figure 5.21: (a) 3rd iteration reconstruction of ^{99m}Tc and ^{123}I vials with 6 cm centre to centre separation, compression factor of 2 used in image reconstruction (b) Intensity profile through point of maximum intensity in the X direction.

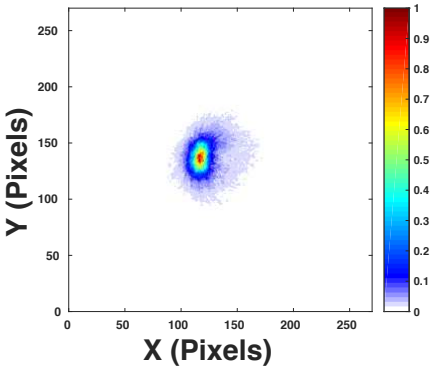

(a)

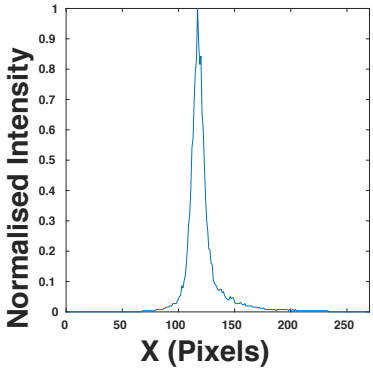

(b)

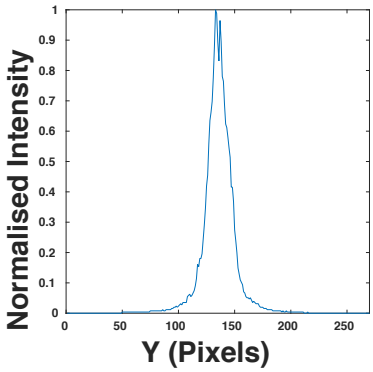

(c)

Figure 5.22: 3rd iteration reconstruction of (a)^{99m}Tc vial using an energy gate of 135 keV to 144 keV and with a compression factor of 2. (b) X-intensity profile through point of maximum intensity (X=117) (c) Y-intensity profile through point of maximum intensity (Y=133).

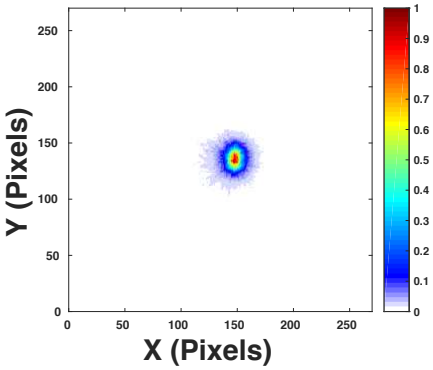

(a)

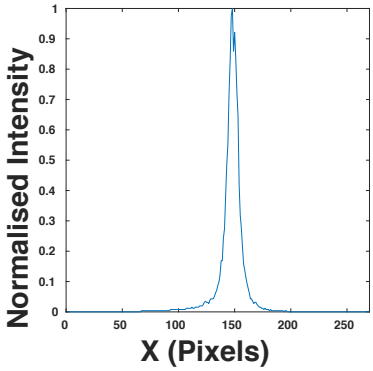

(b)

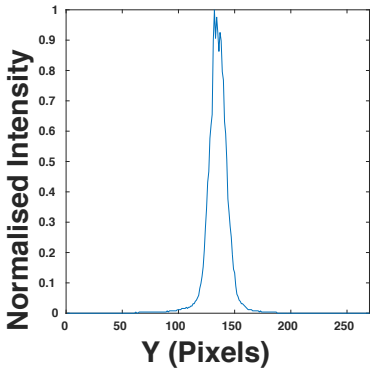

(c)

Figure 5.23: 3rd iteration reconstruction of (a)^{123}I vial using a energy gate of 154 keV to 161 keV and with a compression factor of 2. (b) X-intensity profile through point of maximum intensity (X=148) (c) Y-intensity profile through point of maximum intensity (Y=132).

image matrix at (132,132), therefore the X intensity maxima correspond to the centre +16 pixels and -15 pixels. As each pixel represents 2 mm, the sources are therefore reconstructed at the correct location within a 2 mm accuracy.

5.0.12 ^{99m}Tc, ^{123}I and ^{139}Ce 16.4 mm Diameter Vials

Three 16.4 mm diameter phantom vials were used to investigate the feasibility of multi isotope imaging of a more complex distribution and to investigate the potential resolvability of the fully populated phantom. One vial contained ^{99m}Tc, one ^{123}I and one ^{139}Ce, with activities of 0.80 MBq, 1.33 MBq and 0.95 MBq, respectively. Different radioisotopes were chosen for each vial in order to allow energy gating on each separate vial. The vials were positioned in the phantom as shown in Figure 5.25a i.e orientated perpendicular to the scatter detector. The phantom was placed 65 mm from the scatter cryostat, with the centre of the phantom aligned with the centre of the scatter detector, for data acquisition as shown in Figure 5.25b. Coincidence data were acquired for 60.13 minutes. The Fold [1,1,1,1] add-back energy spectrum that was produced is shown in Figure 5.26. The photopeaks are shown for ^{99m}Tc, ^{123}I and ^{139}Ce with FWHM of 2.71 keV, 2.63 keV and 2.70 keV respectively, which is consistent with previous measurements with these isotopes. The peaks at 185 keV and 197 keV arise from the coincidence detection of the 159 keV gamma ray with the 27 keV gamma from ^{123}I and the 166 keV gamma ray and the 31 keV x-ray from ^{139}Ce, respectively. The energy gates in Table 5.2 were implemented in the iterative reconstruction algorithm for the photopeaks of 141 keV, 159 keV and 166 keV. There was no overlap of the photopeak gates due to the excellent energy resolution of ProSPECTus. The gross counts in each photopeak are shown in Table 5.2.

The 3rd iteration reconstructed image, with a compression factor of 1 is shown in Figure 5.27a, it can be seen that the three vials are not distinguishable. Increasing the iteration number did not improve the resolvability and at iteration 6 the image displayed was not sensible as shown in Figure 5.27b. To investigate if this was due to the varying activities of the vials,

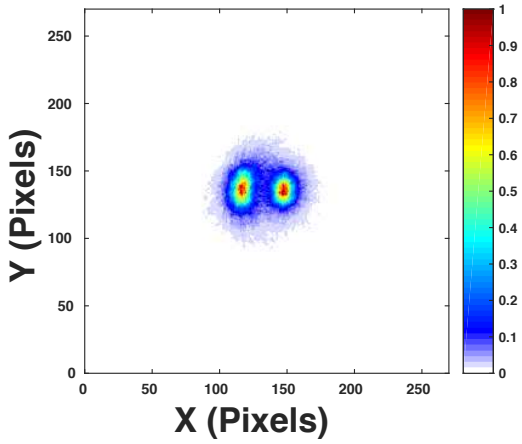

(a)

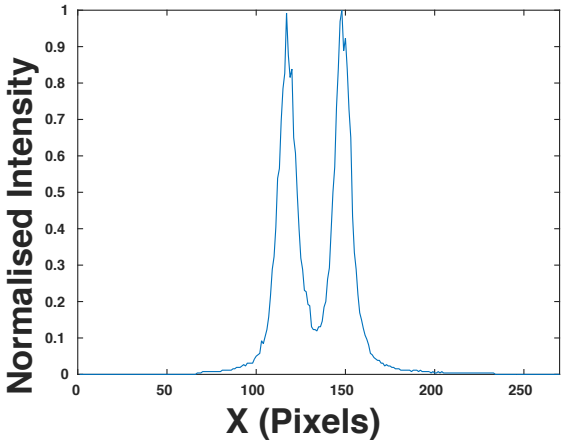

(b)

Figure 5.24: (a) 3rd iteration image of superimposed ^{99m}Tc vial and ^{123}I vials (b) Intensity profile of superimposed image through point of maximum intensity in the X direction.

	Photopeak Energy (keV)	Energy Gate (keV)	Gross Counts
^{99m}Tc	141	135-144	32347 ± 179
^{123}I	159	154-161	63854 ± 252
^{139}Ce	165	162-169	37808 ± 252

Table 5.2: Energy gates used for the ^{99m}Tc, ^{123}I and ^{139}Ce photopeaks in image reconstruction.

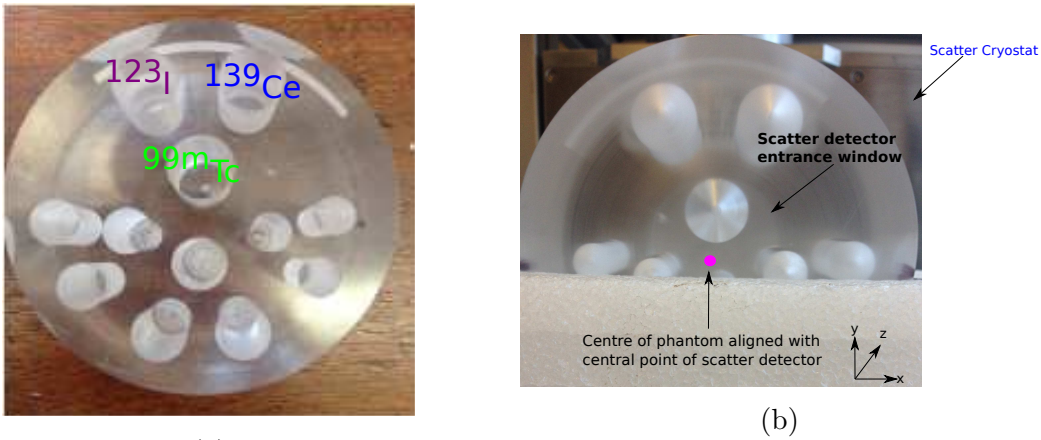

(a) (b)

Figure 5.25: (a) Photograph of the phantom holder with labels showing the position of the 16.4 mm diameter vials filled with ^{99m}Tc, ^{123}I and ^{139}Ce and (b) centre of phantom , aligned with centre of scatter detector for data acquisition in polystyrene phantom holder.

data were analysed from stored preliminary data acquired with ProSPECTus configured with absorber 1. The data were acquired for three 16.4 mm vials filled with ^{139}Ce all with the same activity of 0.75 MBq. The resulting image is shown in Figure 5.28 were it can be seen that the iterative image reconstruction preferentially places counts in the vial closest to the centre of the field of view, even for equal activity sources. For this data, the phantom was placed 65 mm from the scatter cryostat giving a Z-slice value of 166 mm. The centre of the middle vial was aligned with the centre of the scatter detector hence the preferential distribution of the events to the middle vial. It is, therefore believed the distribution shown in Figure 5.27a is due to a combination of the different vial activities and vial location distance with respect to the centre of the field of view. To investigate if these factors are decisive in the ProSPECTus resolvability of complex medical multi-isotope distributions, the following steps were taken:

- Each vial was energy gated individually and reconstructed, i.e providing an image of each vial separately despite the simultaneous acquisition. Figure 5.29 shows the individual reconstructed vials that were previously shown together in Figure 5.27a.

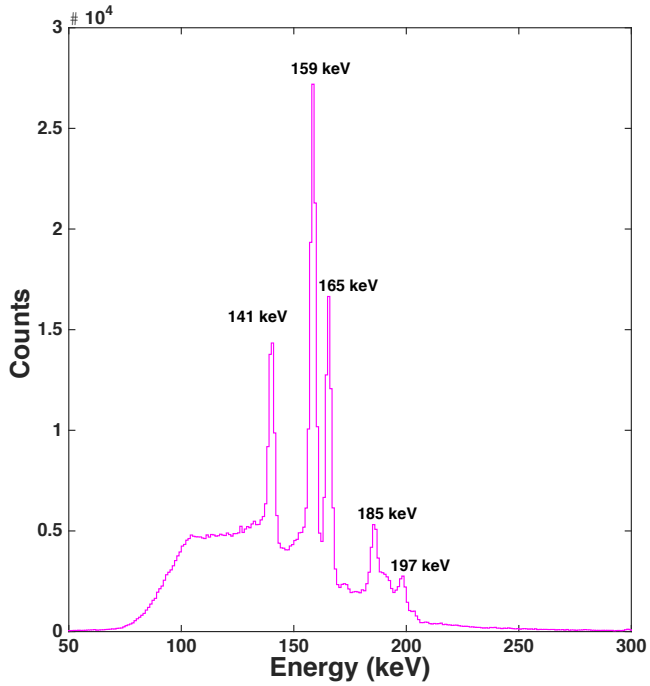

Figure 5.26: Fold [1,1,1,1] energy add-back spectrum collected during data acquisition. The FWHM is 2.71 keV, 2.63 keV and 2.70 keV for ^{99m}Tc,^{123}I and ^{139}Ce respectively. Average digital threshold in absorber 2 set at 90 keV and in the scatter detector 8 keV.

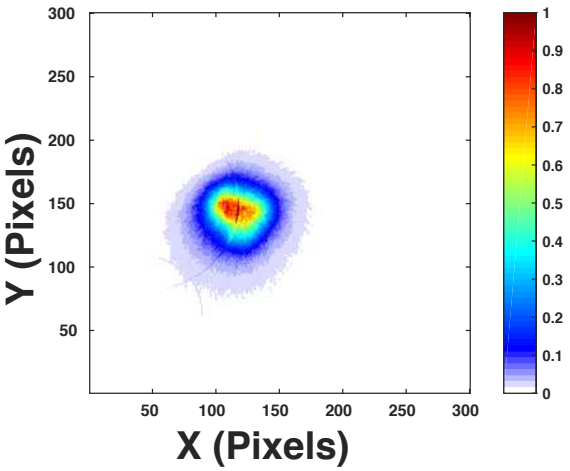
Y (Pixels)
X (Pixels)
300
250
200
150
100
50
1
0.9
0.8
0.7
0.6
0.5
0.4
0.3
0.2
0.1
0

(a)

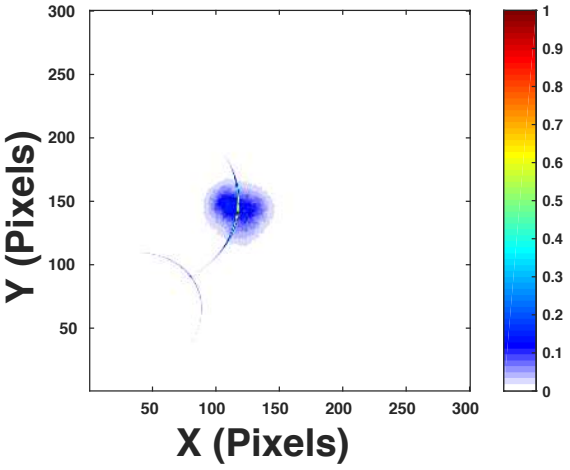
Y (Pixels)
X (Pixels)
300
250
200
150
100
50
1
0.9
0.8
0.7
0.6
0.5
0.4
0.3
0.2
0.1
0

(b)

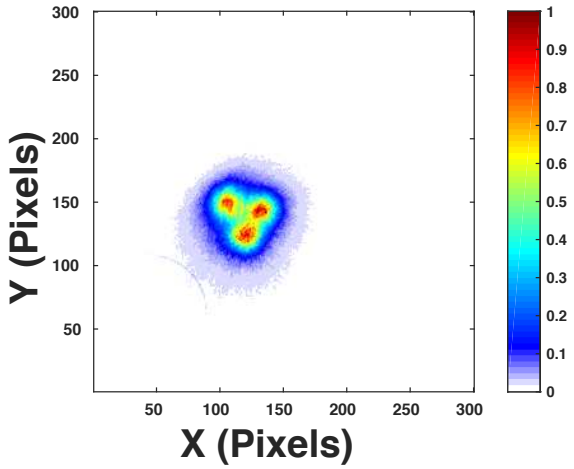

(c)

Figure 5.27: Iterative reconstruction of three 16.4 mm diameter vials placed in phantom holder. Rods filled with aqueous solutions of ^{99m}Tc ,^{139}Ce and ^{123}I . (a) 3rd iteration reconstruction experimental image (b) 6th iteration reconstruction experimental image (c) Superimposed experimental image, using 4th iteration individual vial images in matrix.

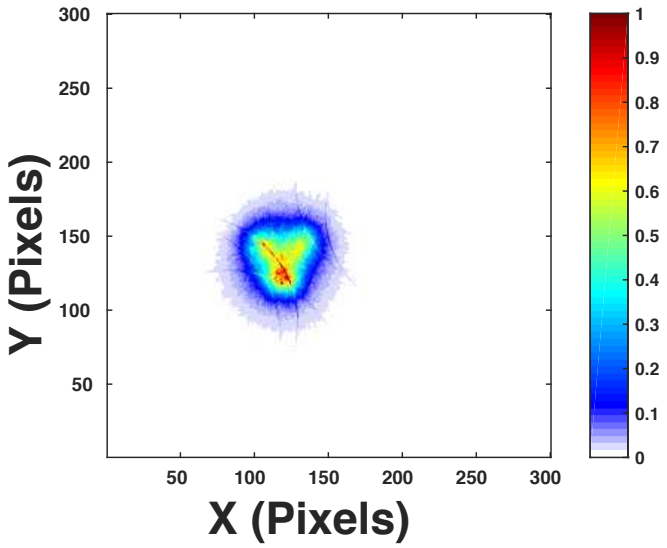

Figure 5.28: Experimental 4th iteration image of three 16.4 mm ^{139}Ce filled vials. Data acquired with phantom holder 65 mm from scatter cryostat, with centre of middle vial, aligned with the centre of the scatter cryostat.

- A Matlab algorithm was created to add the three individual image matrices together resulting in a single matrix i.e a superimposed image.

Figure 5.30 shows the superimposed image using the 1st iteration, 2nd iteration and 3rd iteration reconstructions for each vial. Using this method, all three vials become resolvable in the superimposed image, when the individual energy gated vials have been reconstructed at the 4th iteration, this image is displayed in Figure 5.27c. This demonstrates that the ProSPECTus system, with its intrinsic position and energy resolution is able to resolve the 16.4 mm vials by the 4th iteration. The reconstruction limitation is a feature of the iterative algorithm in which counts are preferentially placed and further demonstrates the need of a probability matrix to be incorporated in the iterative reconstruction algorithm.

5.0.13 Phantom

The phantom holder was fully populated with vials of ^{99m}Tc and ^{123}I, in order to investigate the feasibility of imaging the phantom with the ProSPECTus system (using the absorber 2 configuration). Figure 5.31 is a labeled photograph illustrating which vials were filled with ^{99m}Tc (green) and which were filled with ^{123}I (purple). The front of the phantom holder was placed 65 mm from the scatter cryostat during data acquisition, with the centre of the phantom holder aligned with the centre of the scatter detector. Figure 5.32 is the 10th iteration reconstructed image of the phantom with a compression factor of 2 and at Z-slice 166 mm. Data were acquired for 2 hours, as this was calculated to be sufficient for each vial to contribute at least 10,000 photopeak counts, which is important for the image reconstruction. It is shown that none of the vials in the phantom are distinguishable in Figure 5.32, which aligns with the results presented for the phantom subset previously. The established hypothesis that the image reconstruction algorithm limits the resolvability was then explored by individually collecting data for each vial in the phantom holder. The vials were sequentially and individually imaged, in their same corresponding locations as shown in Figure 5.31, with the front of the phantom placed at the same geometrical distance, i.e a Z-slice

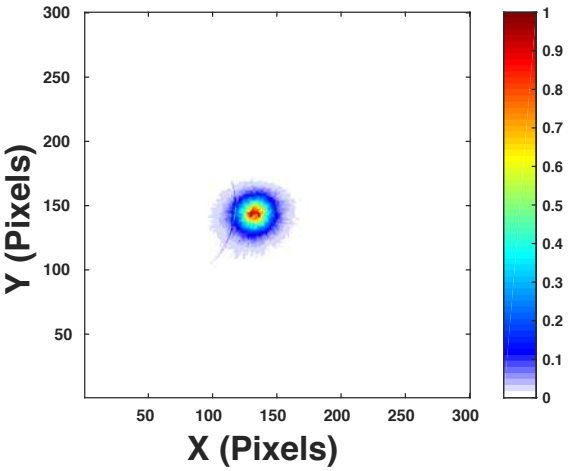
Y (Pixels)
X (Pixels)
300
250
200
150
100
50
50
100
150
200
250
300
1
0.9
0.8
0.7
0.6
0.5
0.4
0.3
0.2
0.1
0

(a)

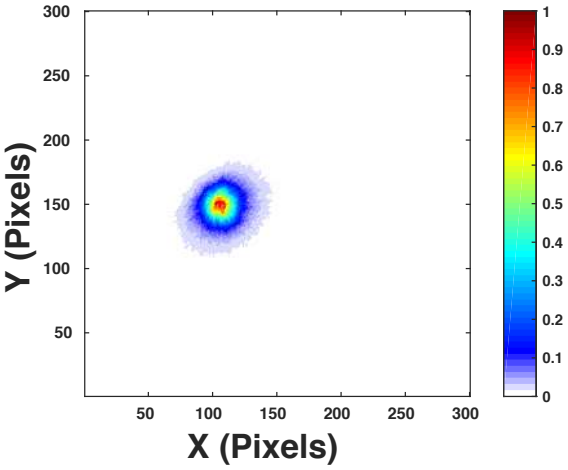
Y (Pixels)
X (Pixels)
300
250
200
150
100
50
50
100
150
200
250
300
1
0.9
0.8
0.7
0.6
0.5
0.4
0.3
0.2
0.1
0

(b)

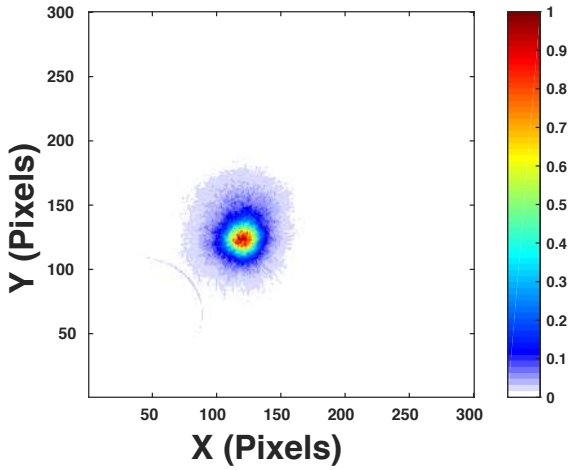

(c) Tc

Figure 5.29: 4th iterative reconstruction images of (a) ^{139}Ce (b) ^{123}I (c) ^{99m} Tc. All images are reconstructed individually through energy gates, that are defined in Table 5.2

.

of 166 mm. The data acquisition period for each vial was chosen to ensure 10,000 counts in the Fold[1,1,1,1] addback spectrum photopeak of each vial was recorded.

To determine at what iteration number the vial image matrices should be processed individually then superimposed, the individual vials were quantitatively analysed. As with previous point source data, intensity profiles through the imaging pixel of maximum intensity were used to quantify the resolution of the image. It would be expected in an ideal system, isolated from physics effects such as Doppler broadening, Field-Of-View sensitivity variation, pin-cushion effects, detector position resolution and energy resolution, that an intensity profile consistent with a square pulse would represent the cross-sectional activity of a vial, with the width equal to the rod diameter. This ideal intensity profile distribution is shown for a 16.4 mm diameter vial size, in Figure 5.33 (red). However, due to the aforementioned physics effects, the ideal distribution is not observed experimentally. Instead the intensity profiles, which are analogous to a Line Spread Function (LSF), contain statistical fluctuations as seen in Figure 5.39d where the intensity for the 16.4 mm diameter vials positioned at phantom location 1 (see Figure 5.31) during data acquisition are overlayed, for iteration numbers 1, 3 and 7. It can be seen that the distributions decrease in width as the iteration number increases, as expected from previous investigations of the iterative algorithm. However, the statistical fluctuations in the intensity profiles prevent mathematical functions such as Lorentzian or Gaussian fits representing the data well. Therefore, the Edge-Response (ER) was investigated as an alternative method to quantify the vial images. The ER is the integral of the Line Spread Function (LSF) and an example is shown in Figure 5.34. The ER plots used in this thesis are produced through the following steps:

1. Normalised intensity profile taken through the image slice pixel of maximum intensity.

2. Cumulative frequency of the normalised intensity profiles calculated.

3. Cumulative frequency plotted as a function of X or Y pixel number (depending on direction of intensity-profile).

The width of an LSF is quoted as FWHM, whereas the ER is quoted as the difference in pixels (or mm) from 10% to 90% of the maximum distribution height. The ER values were used to identify at what reconstruction iteration number the phantom vials could be resolvable and ideally represented in the image distribution by its true size. If the FWHM or ER value is equal to the diameter (2r) of the rods, they should be resolvable. This is because the vials within a particular subset (ie 3 rods of identical size), are positioned with an edge to edge distance corresponding to the diameter (2r) of the vial, as shown in Figure 5.35. This is demonstrated by considering the case of two rods from the 16.4 mm subset. As discussed in detail later, the ER value indicated that iteration number 5 produced an ER value of 16 mm for these subsets. The intensity profiles (blue) for this iteration number and the ideal distributions (red) are shown in Figure 5.36 for the top two rods of the 16.4 mm (located above position 1 in the phantom holder).

The ER values were determined by the same methodology for one vial from each subset. The selected vial positions are indicated in Figure5.31. These positions were chosen as they are closest to the centre of the phantom, thereby minimising influences from the sensitivity variation within the field of view. The values for the 16.4 mm, 12.4 mm, 11 mm and 10 mm rods are shown in Figure 5.37, each ER value has an associated error of 2.8 mm. It can be seen that the ER that is representative within errors of the correct vial diameter is seen at iteration 5, 9, 10 and 10 for the 16.4 mm, 12.4 mm, 11mm and 10 mm vials, respectively. The ER distributions for these results is shown in Figure 5.38. Therefore, the individual rods were processed through the iterative reconstruction algorithm to their corresponding iteration numbers (5, 9, 10 and 10 for the 16.4 mm, 12.4 mm, 11 mm and 10 mm, respectively). The individual images from vials of equal diameter were superimposed to produce the images for each subset shown in Figure 5.39. These images were then superimposed into one single matrix to show the full phantom, this image is shown in Figure 5.40. These results further demonstrate the need for a probability matrix to be implemented in the iterative reconstruction algorithm and define a method for quantifying which iteration number to reconstruct to. It is hypothesized that if the iterative re-

construction algorithm incorporates a probability matrix, the full populated phantom will be resolvable with the next generation ProSPECTus system, without the need of superposition techniques.

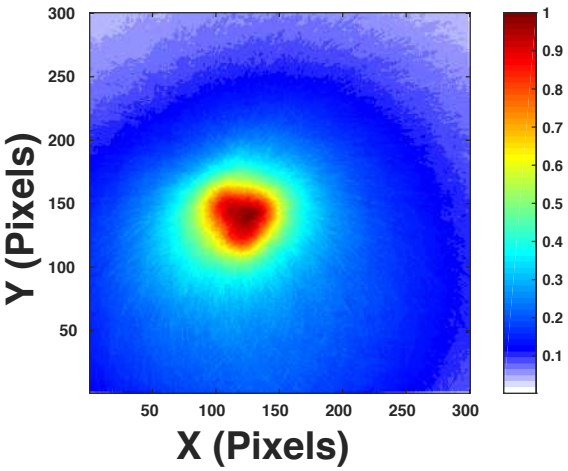
Y (Pixels)
X (Pixels)
300
250
200
150
100
50
1
0.9
0.8
0.7
0.6
0.5
0.4
0.3
0.2
0.1

(a)

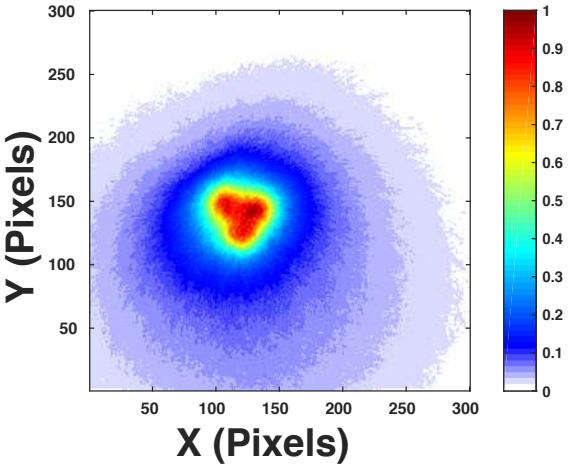
Y (Pixels)
X (Pixels)
300
250
200
150
100
50
1
0.9
0.8
0.7
0.6
0.5
0.4
0.3
0.2
0.1
0

(b)

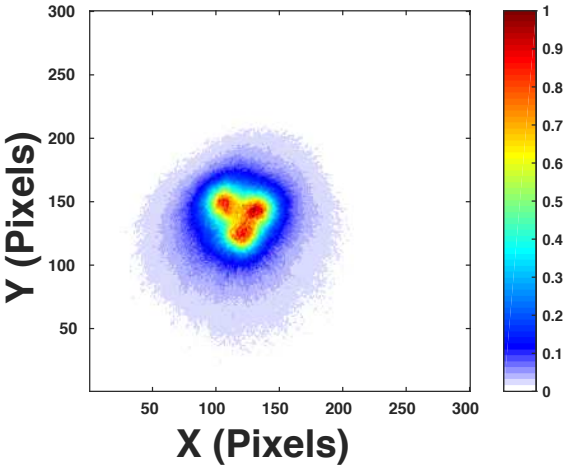

(c)

Figure 5.30: Superimposed images for (a) 1st iteration (b) 2nd iteration and (c) 3rd iteration reconstructed vials.

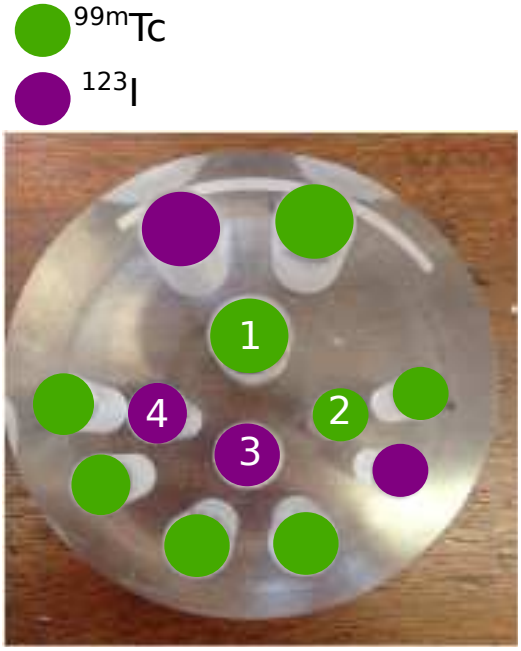

Figure 5.31: Labeled photograph of phantom, detailing which vials contained ^{99m}Tc and which contained ^{123}I.

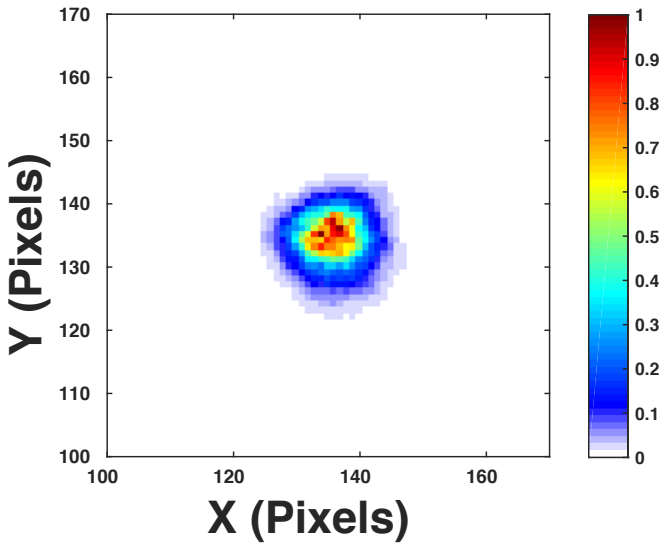

Figure 5.32: Phantom containing all vials either filled with ^{99m}Tc and ^{123}I. The 10th iteration image is shown with a compression factor of 2 and a Z-slice position of 166 mm.

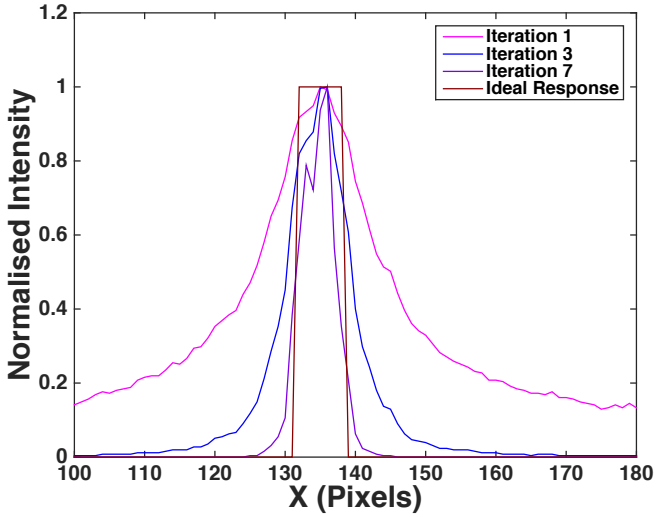

Figure 5.33: X-intensity profiles for iteration numbers (1, 3 and 7) through a ^{99m}Tc 16.4 mm diameter vial of experimental data the ideal expected profile (red) through a vial when neglecting physics effects.

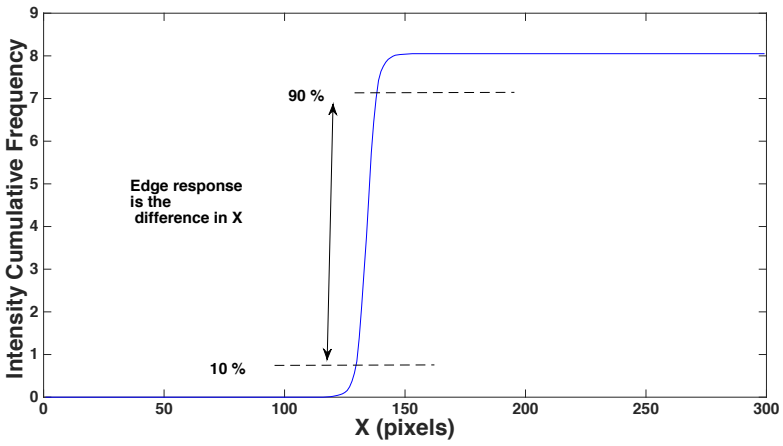

Figure 5.34: ER profile for iteration 5 of the 16.4 mm ^{99m}Tc vial placed at position 1 in phantom. The vial size is measured from the difference in X(pixels) from 10% to 90% peak height.

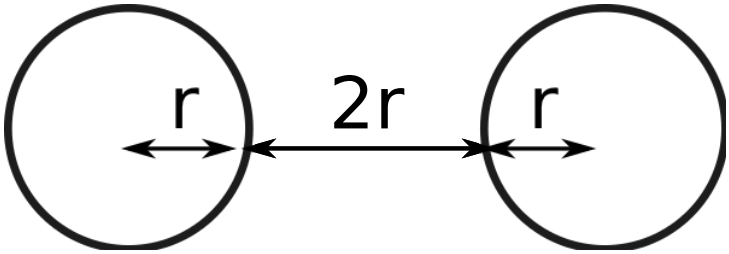

Figure 5.35: Schematic diagram of how the subset of vials in terms of size are separated in the phantom holder. The ER function is used to determine when the iterative reconstruction algorithm produces an image where the diameter of the vial is reconstructed to the correct size.

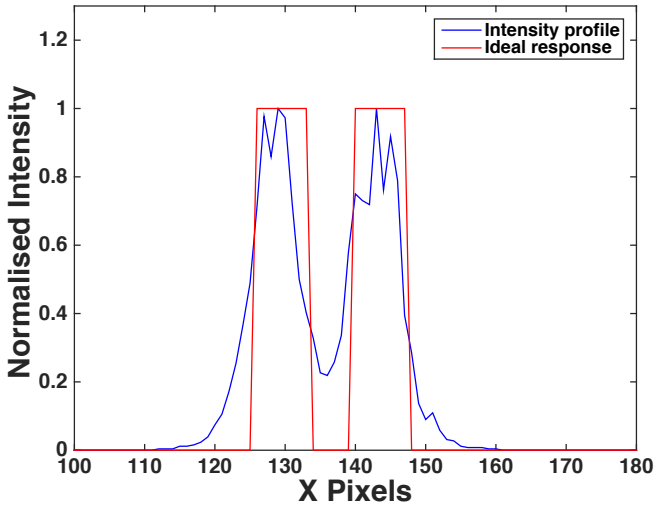

Figure 5.36: X-intensity profile (blue), through the 5th iteration image of two superimposed 16.4 mm diameter sized vials. Each pixel represents 2 mm in phase space. The red profiles represent the ideal intensity distribution of the vials.

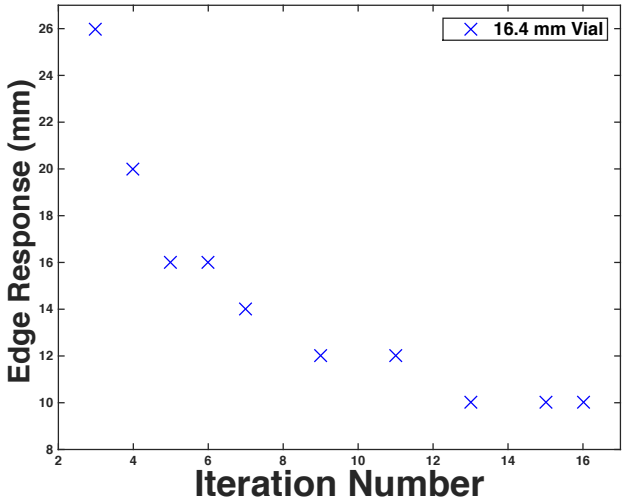
16.4 mm Vial
Edge Response (mm)
Iteration Number

(a)

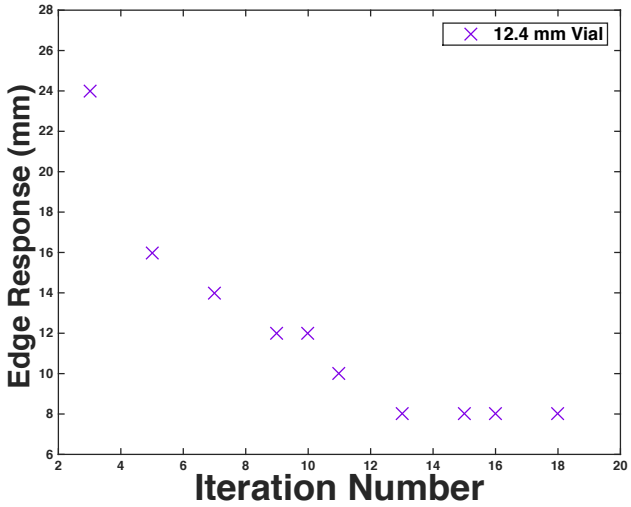
12.4 mm Vial
Edge Response (mm)
Iteration Number

(b)

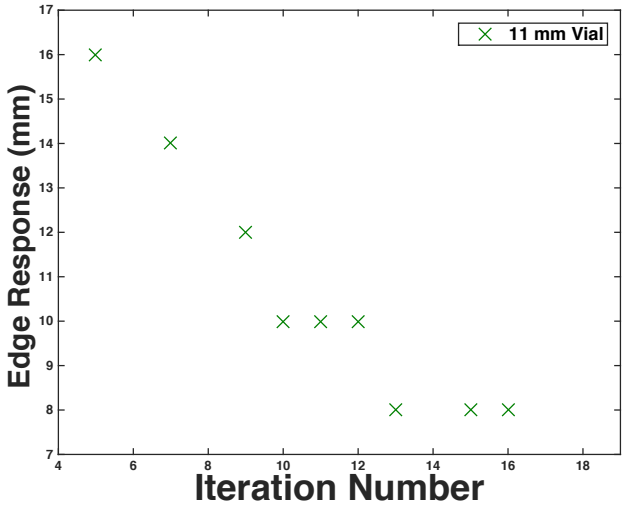

(c)

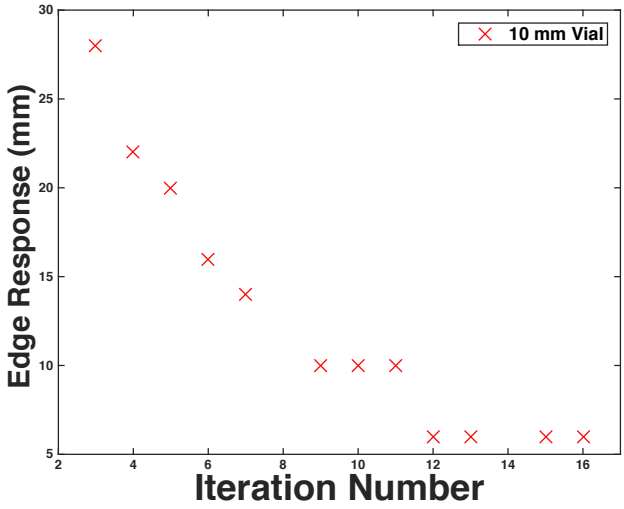

(d)

Figure 5.37: Edge-Response values (mm) as a function of iteration number for vial sizes of diameter (a) 16.4 mm (b) 12.4 mm (c) 11 mm and (d) 10 mm.

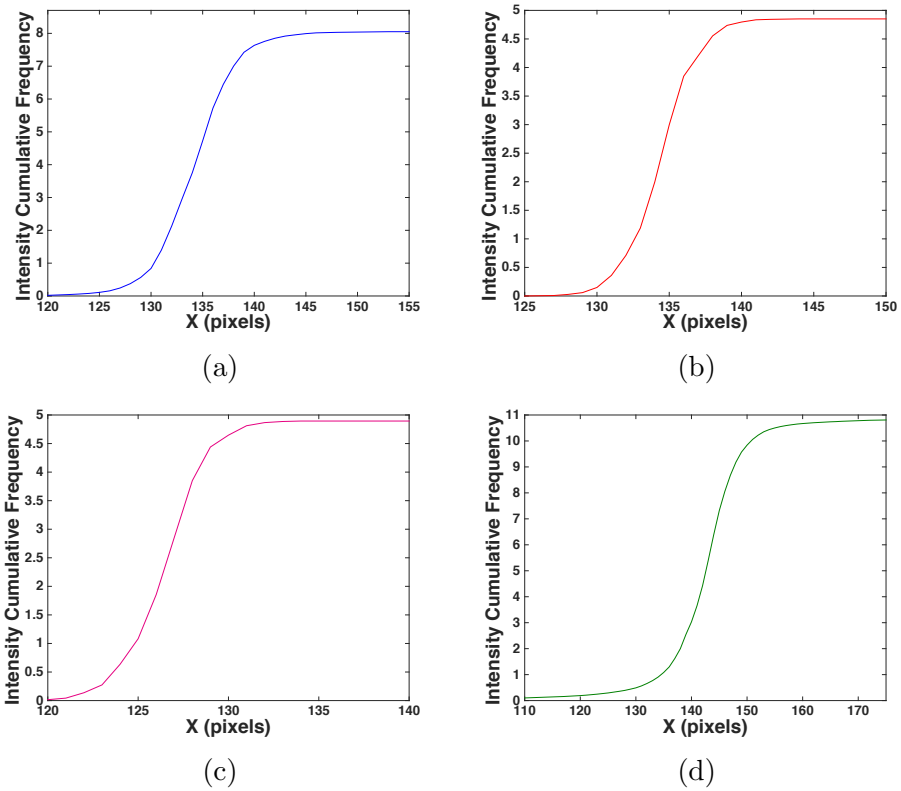

Figure 5.38: ER profiles for the (a) 16.4 mm vial at iteration 5 (b) 12.4 mm vial at iteration 9 (c) 11 mm vial and (d) 10 mm vials at iteration 10. These profiles are at the iteration number which give an ER that is representative of the corresponding vial diameter. Each pixel represents 2 mm in phase space.

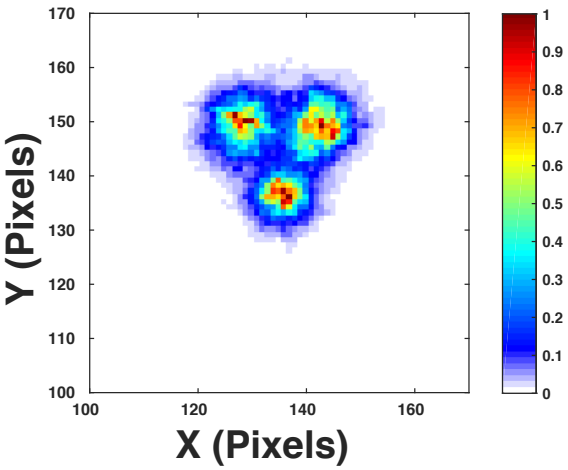
Y (Pixels)
X (Pixels)
170
160
150
140
130
120
110
100
100
120
140
160
1
0.9
0.8
0.7
0.6
0.5
0.4
0.3
0.2
0.1
0

(a)

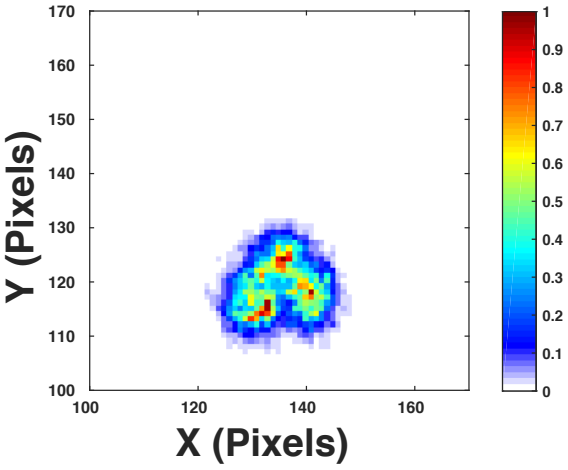
Y (Pixels)
X (Pixels)
170
160
150
140
130
120
110
100
100
120
140
160
1
0.9
0.8
0.7
0.6
0.5
0.4
0.3
0.2
0.1
0

(b)

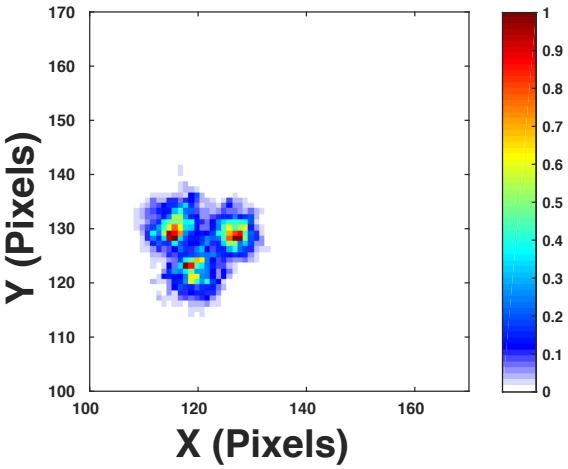

(c)

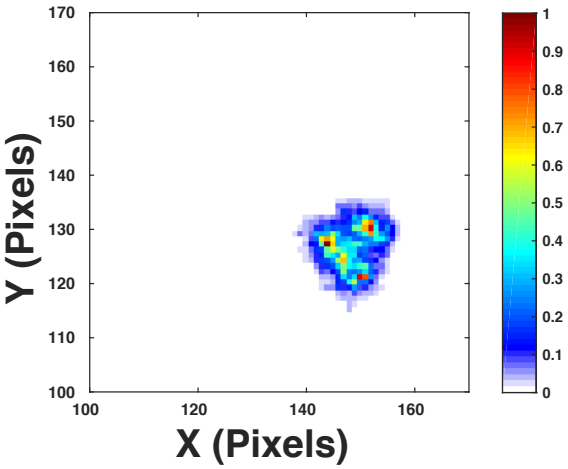

(d)

Figure 5.39: Superimposed images for vial size subsets of the phantom, at the iteration number that shows resolvability, as predicted by the ER results (a) 16.4 mm diameter vials at the 5th iteration reconstruction, (b) 12.4 mm diameter vials at the 8th iteration reconstruction, (c) 11 mm diameter vials at the 10th iteration reconstruction, and (d) 10 mm diameter vials at the 10th iteration reconstruction. All images reconstructed with a compression factor of 2.

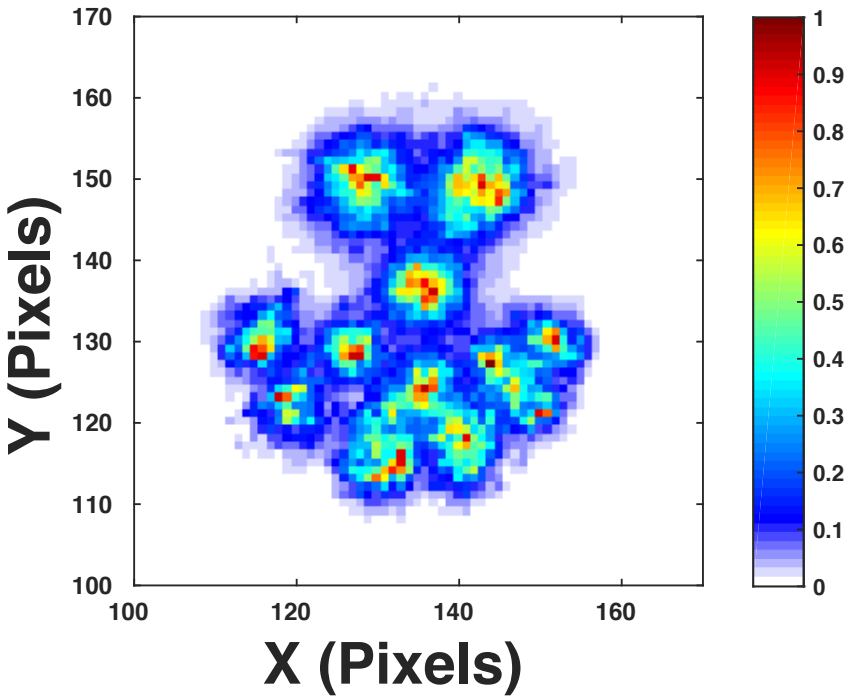

Figure 5.40: Superimposed image of all the phantom vial subsets, reconstructed at their respective iteration number according to the ER results.

Chapter 6

Conclusions and Future Work

In this thesis, the feasibility of imaging the medical radioisotopes ^{99m}Tc (141 keV) and ^{123}I (159 keV) with the ProSPECTus Compton camera has been investigated. The ProSPECTus project based at the University of Liverpool and in collaboration with STFC Daresbury, has been designed to alleviate the limitations of conventional SPECT. The system utilises segmented semiconductor detectors in a Compton camera configuration. The work in this project has been performed using a prototype ProSPECTus system consisting of HPGE and Si(Li) planar detectors housed in separate cryostat. The next generation ProSPECTus system will consist of a Si(Li) and HPGe detector system, housed in a custom made, magnetic compatible cryostat, with the intention of co-registry with MRI scanners. It is intended that the research and findings in this project will inform the experimental setup and operation of the next generation ProSPECTus system.

6.0.14 Conclusion

In order to achieve optimum performance in spectroscopic imaging of multiple medical isotopes, a significant contribution of this thesis was to optimise experimental setup details of the ProSPECTus system and assess the energy resolution, noise levels and timing resolution. The resulting images produced by analytical and iterative reconstruction algorithms were then quantitatively and qualitatively evaluated. A summary of the results from both sections of

work are summarised below.

Experimental Set Up

A time coincidence window is an important operational parameter of a Compton camera as an unoptimised setting can potentially degrade the efficiency and image resolution. Therefore with a NaI(Tl) detector the intrinsic timing response of the Si(Li) and HPGe detectors were investigated through a series of techniques, utilising analogue and digital signal processing. The results of the intrinsic timing measurements are quoted in Table 6.1.

	Analogue		**Digital**		**Digital Gated**	
	Si(Li)	HPGe	Si(Li)	HPGe	Si(Li)	HPGe
Average AC Timing Resolution (ns)	21 ± 2	21 ± 2	25 ± 2	26 ± 2	16 ± 2	20 ± 2
Average DC Timing Resolution (ns)	21 ± 4	31 ± 2	23 ± 1	28 ± 2	16 ± 1	23 ± 3
Overall Average Timing Resolution (ns)	21 ± 4	26 ± 6	23 ± 1.5	27 ± 2.5	16 ± 1	22 ± 2.5

Table 6.1: Table displaying the average timing resolution of both the Si(Li) and HPGe detectors. The average timing response is shown for the AC and DC sides of both detectors as well as the overall average timing response.

The timing investigations of the ProSPECTus system detectors used together revealed an average coincidence time of 25 ns for energy gated events and 36 ns with no energy gates. However additional timing properties of the CFD algorithms in the CAEN digitisers used to acquire Compton imaging data were studied and showed that a system coincidence window of 150 ns is required to process the optimum number of events for Compton imaging, which is much larger than the intrinsic detector resolution.

Compton Camera Performance

A ^{139}Ce point source was used to determine the efficiency and spatial resolution of the ProSPECTus system. This was chosen because it has a gamma

ray emission energy of 166 keV, within the range of energies used in medical imaging, but a longer half-life than typical medical isotopes.

It has been determined that a spatial resolution of 3 mm is achievable when processing experimental Compton imaging data through iterative reconstruction algorithms, which is a considerable improvement to the 25 mm spatial resolution determined with analytical reconstruction algorithms. This results demonstrates that the ProSPECTus system is capable of competing with conventional Clinical SPECT systems which have a spatial resolution of $\sim$ 7-13 mm.

Although not a primary aim of this thesis, the efficiency of the ProSPECTus system has been determined for a ^{139}Ce point source placed 4 cm from from the ProSPECTus system to be 0.067% for single-single events, those used for image reconstruction in this thesis. This is an improvement of a factor of 2.5 compared to conventional SPECT systems. This result demonstrates the capability of the next generation ProSPECTus system in delivering reduced dose or increased patient throughput in a clinical environment. However, by recovering the known experimental losses and processing more complex event sequences, a factor of 23 improvement over SPECT is expected in future work.

Multi-medical isotope imaging with ^{99m}Tc (141 keV) and ^{123}I (159 keV)

In order to test the feasibility of multi medical isotope imaging and build source complexity, a phantom was designed based on a clinical Jaszczak SPECT phantom, which is used for performance assessments.

The system energy resolution of ProSPECTus was measured as 2.82keV and 2.80 keV at gamma-ray energies of 141 keV and 159 keV, respectively, for Compton imaging events, demonstrating that the spectroscopic response enables simultaneous data acquisition of ^{99m}Tc and ^{123}I. Such studies would require complex peak deconvolution techniques to be implemented in current SPECT systems.

Qualitative assessment of complex source geometries revealed that the

iterative reconstruction algorithm limits the performance of the phantom reconstruction due to field of view and sensitivity influences. The ProSPECTus system is shown with the aid of edge response analysis to be capable of resolving the full phantom i.e for a range between 16.4 mm and 10 mm with extended source distributions. This was achieved by alleviating the limitations of the iterative reconstruction algorithm by superimposing individually reconstructed vials.

6.0.15 Future Work

The work in this thesis has identified areas of improvement, in order for the next generation ProSPECTus system to reach its full potential. These suggestions are identified below:

1. It is calculated in this thesis that the efficiency of the next generation Prospectus system can be improved up to a factor of 13 compared to conventional SPECT systems. It is suggested that thresholds be kept directly above the noise in the scatter detector and that algorithms are developed to include in the image fully absorbed gamma-rays with complex interaction sequences.

2. The spatial resolution of complex sources and the determination of the correct location in depth (Z) can be improved via the implementation of Pulse Shape Analysis (PSA) techniques. These will improve the position resolution beyond the segmentation of the ProSPECTus detectors. This method could not be attempted with absorber 1, due to large noise fluctuations in the preamplifier signals and the arrival of absorber 2 late in the project meant it was not feasible to fully characterise the position dependent signal response on the timescale of this thesis. This characterisation is now underway.

3. A limitation of the current iterative reconstruction algorithm is the preferential placement of counts to areas that are closer to the field of view, or have relatively greater counts for e.g higher activity sources, compared to other distribution in the image. It is therefore advised that

a probability normalisation matrix be implemented into the iterative reconstruction algorithm to rectify this.

4. It is recommended that quantitative analysis of the phantom measurement regarding noise and contrast are ascertained.

5. It is suggested that once the above improvements are made, that resolving a phantom with smaller vials of 7 mm diameter size is attempted, in order to resolve complex source distribution for the full range that is achievable with conventional SPECT systems.

Appendices

Appendix A

Detector Performance

The detectors used in this work have been energy calibrated and characterised in terms of energy resolution and timing resolution. The details of the individual strip calibration and performance for each detector used in this project are cataloged in this chapter.

A.1 Energy Calibration

A quadratic energy calibration was done for each detector used in this project. The calibration coefficients for the scatter, absorber 1 and absorber 2 detectors are shown in Table A.1 , Table A.2 and Table A.3 respectively.

A.2 Energy Resolution

Energy resolution measurements were taken with the scatter (Si(Li)), absorber 1 (HPGe) and absorber 2 (HPGe) detectors. Each strip was individually and sequentially investigated. The Energy resolution was determined through analogue electronics as described in Section 4.1 and also after the preamplifier pulse were digitally processed. The average energy resolution response has been quoted in this thesis, the results these were calculated from are displayed as follows:

- **Scatter detector:** Table A.4 and A.5 display the energy resolution of

Strip	**a**	**b**	**c**
AC01	9.94 x 10^{-2}	9.95 x 10^{-2}	-9.70 x 10^{-9}
AC02	6.45 x 10^{-2}	11.0 x 10^{-2}	1.82 x 10^{-7}
AC03	1.5 x 10^{-2}	9.81 x 10^{-2}	3.63 x 10^{-8}
AC04	28.7 x 10^{-2}	10.1 x 10^{-2}	5.74 x 10^{-8}
AC05	48.7 x 10^{-2}	9.68 x 10^{-2}	3.46 x 10^{-7}
AC06	34.6 x 10^{-2}	10.6 x 10^{-2}	1.62 x 10^{-7}
AC07	9.50 x 10^{-2}	10.6 x 10^{-2}	8.30 x 10^{-8}
AC08	3.98 x 10^{-2}	10.3 x 10^{-2}	7.06 x 10^{-9}
AC09	4.33 x 10^{-2}	11.1 x 10^{-2}	1.37 x 10^{-7}
AC10	36.3 x 10^{-2}	9.90 x 10^{-2}	1.45 x 10^{-7}
AC11	36.2 x 10^{-2}	10.1 x 10^{-2}	8.03 x 10^{-8}
AC12	34.6 x 10^{-2}	10.5 x 10^{-2}	8.95 x 10^{-8}
DC15	34.1 x 10^{-2}	9.52 x 10^{-2}	5.01 x 10^{-9}
DC16	37.8 x 10^{-2}	9.51 x 10^{-2}	1.53 x 10^{-8}
DC17	33.1 x 10^{-2}	9.74 x 10^{-2}	1.69 x 10^{-9}
DC18	30.5 x 10^{-2}	9.52 x 10^{-2}	1.18 x 10^{-8}
DC19	26.7 x 10^{-2}	10.05 x 10^{-2}	7.12 x 10^{-8}
DC20	31.9 x 10^{-2}	10.10 x 10^{-2}	1.19 x 10^{-8}
DC21	29.0 x 10^{-2}	10.8 x 10^{-2}	1.16 x 10^{-7}
DC22	34.2 x 10^{-2}	9.37 x 10^{-2}	3.85 x 10^{-8}
DC23	41.4 x 10^{-2}	9.67 x 10^{-2}	1.70 x 10^{-7}
DC24	41.2 x 10^{-2}	9.64 x 10^{-2}	2.14 x 10^{-7}
DC25	3.54 x 10^{-2}	10.3 x 10^{-2}	5.86 x 10^{-8}

Table A.1: Calibration coefficients for each individual strip of the scatter detector.

Strip	**a**	**b**	**c**
AC01	13.1 x 10^{-2}	12.5 x 10^{-2}	8.62 x 10^{-9}
AC02	12.2 x 10^{-2}	12.9 x 10^{-2}	1.03 x 10^{-7}
AC03	13.5 x 10^{-2}	12.3 x 10^{-2}	8.77 x 10^{-8}
AC04	15.2 x 10^{-2}	12.9 x 10^{-2}	7.91 x 10^{-8}
AC05	15.0 x 10^{-2}	12.5 x 10^{-2}	9.98 x 10^{-8}
AC06	17.4 x 10^{-2}	12.7 x 10^{-2}	1.61 x 10^{-7}
AC07	15.6 x 10^{-2}	12.8 x 10^{-2}	11.0 x 10^{-7}
AC08	13.5 x 10^{-2}	12.3 x 10^{-2}	9.32 x 10^{-8}
AC09	12.1 x 10^{-2}	12.3 x 10^{-2}	8.34 x 10^{-8}
AC10	11.5 x 10^{-2}	13.7 x 10^{-2}	1.23 x 10^{-7}
AC11	10.3 x 10^{-2}	12.3 x 10^{-2}	4.54 x 10^{-8}
AC12	12.4 x 10^{-2}	12.3 x 10^{-2}	1.01 x 10^{-7}
DC01	-4.62 x 10^{-2}	12.6 x 10^{-2}	-1.04 x 10^{-6}
DC02	24.1 x 10^{-2}	12.4 x 10^{-2}	6.60 x 10^{-8}
DC03	26.7 x 10^{-2}	12.3 x 10^{-2}	6.87 x 10^{-8}
DC04	28.1 x 10^{-2}	12.2 x 10^{-2}	1.03 x 10^{-7}
DC05	32.4 x 10^{-2}	11.9 x 10^{-2}	1.16 x 10^{-7}
DC06	32.5 x 10^{-2}	12.5 x 10^{-2}	1.43 x 10^{-7}
DC07	32.6 x 10^{-2}	12.6 x 10^{-2}	1.45 x 10^{-7}
DC08	30.1 x 10^{-2}	12.3 x 10^{-2}	1.44 x 10^{-7}
DC09	26.3 x 10^{-2}	12.2 x 10^{-2}	9.19 x 10^{-8}
DC10	25.6 x 10^{-2}	12.4 x 10^{-2}	5.25 x 10^{-8}
DC11	36.7 x 10^{-2}	13.4 x 10^{-2}	2.14 x 10^{-6}
DC12	-40.3 x 10^{-2}	12.6 x 10^{-2}	-9.47 x 10^{-7}

Table A.2: Calibration coefficients for Absorber 1 detector

Strip	**a**	**b**	**c**
AC01	13.2 x 10^{-2}	16.4 x 10^{-2}	6.06 x 10^{-9}
AC02	0.27 x 10^{-2}	17.4 x 10^{-2}	- 4.35 x 10^{-9}
AC03	1.31 x 10^{-2}	17.1 x 10^{-2}	1.57 x 10^{-9}
AC04	10.9 x 10^{-2}	16.3 x 10^{-2}	8.38 x 10^{-9}
AC05	7.82 x 10^{-2}	17.1 x 10^{-2}	4.14 x 10^{-9}
AC06	14.6 x 10^{-2}	16.8 x 10^{-2}	7.07 x 10^{-9}
AC07	12.9 x 10^{-2}	17.1 x 10^{-2}	1.03 x 10^{-8}
AC08	4.19 x 10^{-2}	16.9 x 10^{-2}	- 2.04 x 10^{-9}
AC09	26.4 x 10^{-2}	17.1 x 10^{-2}	2.33 x 10^{-8}
AC10	15.3x 10^{-2}	17.3 x 10^{-2}	8.37 x 10^{-9}
AC11	6.70 x 10^{-2}	17.1 x 10^{-2}	- 2.96 x 10^{-9}
AC12	15.3 x 10^{-2}	16.9 x 10^{-2}	1.02 x 10^{-8}
DC01	37.0 x 10^{-2}	16.7 x 10^{-2}	3.39 x 10^{-9}
DC02	14.7x 10^{-2}	15.8 x 10^{-2}	- 2.58 x 10^{-0}
DC03	14.3 x 10^{-2}	16.0 x 10^{-2}	- 1.34 x 10^{-9}
DC04	26.7 x 10^{-2}	16.8 x 10^{-2}	8.19 x 10^{-9}
DC05	24.4 x 10^{-2}	16.2 x 10^{-2}	6.36 x 10^{-9}
DC06	25.1 x 10^{-2}	16.2 x 10^{-2}	5.30 x 10^{-9}
DC07	1.80 x 10^{-2}	16.9 x 10^{-2}	- 1.45 x 10^{-8}
DC08	18.5 x 10^{-2}	16.1 x 10^{-2}	- 8.90 x 10^{-10}
DC09	25.8 x 10^{-2}	16.6 x 10^{-2}	3.23 x 10^{-9}
DC10	4.46 x 10^{-2}	16.1 x 10^{-2}	- 8.44 x 10^{-9}
DC11	10.2 x 10^{-2}	16.3 x 10^{-2}	- 1.20 x 10^{-8}
DC12	19.9 x 10^{-2}	17.0 x 10^{-2}	- 3.16 x 10^{-9}

Table A.3: Calibration coefficients for Absorber 2 detector

each strip for analogue processed signal and digitally processed signals respectively.

- **Absorber 1 detector:** Table A.6 and Table A.7 display the energy resolution of each strip for analogue processed signal and digitally processed signals respectively.

- **Absorber 2 detector:** Table A.8 and Table A.9 display the energy resolution of each strip for analogue processed signal and digitally processed signals respectively.

The point sources used for the energy resolution investigations and their corresponding gamma ray energies are : ^{241}Am (60 keV), ^{57}Co (122 keV) and ^{139}Ce(166 keV) .

A.2.1 Timing Response

The timing response of each detector was determined through using a NaI(Tl) and the coincidence 511 keV gamma rays from a ^{22}Na point source. The experimental methodology used to obtain the timing response in each detector is found in Section 4.2.6 of this thesis. The timing response of each individual strip of the Si(Li) (scatter) and (HPGe) (absorber 1) detector are given in Table A.10 and Table A.11, respectively.

Strip	**FWHM(keV) at 60 keV**	**FWHM(keV) at 122 keV**
AC01	1.10	1.30
AC02	1.13	1.19
AC03	1.09	1.25
AC04	1.21	1.21
AC05	1.21	1.22
AC06	1.26	1.32
AC07	1.27	1.37
AC08	1.22	1.30
AC09	1.21	1.22
AC10	1.17	1.23
AC11	1.08	1.28
AC12	1.28	1.31
DC15	0.95	1.03
DC16	0.78	0.97
DC17	0.87	0.99
DC18	0.95	1.03
DC19	0.89	1.00
DC20	0.93	1.10
DC21	0.95	0.97
DC22	0.85	1.00
DC23	0.89	1.01
DC24	1.45	1.05
DC25	0.90	1.06

Table A.4: The energy resolution for each strip of the scatter detector at 60 keV and 122 keV. Results acquired with analogue electronics.

Strip	**FWHM (keV) at 60 keV**	**FWHM (keV) at 122 keV**	**FWHM (keV) at 166 keV**
AC01	1.58	2.29	2.40
AC02	1.71	1.64	2.21
AC03	1.78	1.86	2.27
AC04	1.81	2.13	2.20
AC05	1.76	2.59	2.34
AC06	2.19	1.93	2.26
AC07	2.15	1.87	2.33
AC08	1.87	1.84	2.33
AC09	1.77	2.75	2.38
AC10	1.63	2.18	2.40
AC11	1.84	2.04	2.36
AC12	1.74	1.94	2.38
DC15	1.58	2.00	2.08
DC16	1.68	1.81	1.86
DC17	1.62	1.98	1.83
DC18	1.73	2.12	2.04
DC19	1.44	1.97	1.85
DC20	1.44	1.88	1.90
DC21	1.46	1.88	2.06
DC22	1.40	1.86	1.92
DC23	1.46	1.99	1.99
DC24	1.52	1.81	2.02
DC25	1.56	1.92	2.42

Table A.5: The energy resolution of each strip of the scatter detector at gamma-ray energies of 60 keV, 122 keV and 166 keV. Results determined after digital processing.

Strip	**FWHM (keV) at 60 keV**	**FWHM (keV) at 122 keV**
AC01	1.84	2.1
AC02	1.83	1.90
AC03	2.06	2.20
AC04	2.84	2.90
AC05	2.15	2.20
AC06	1.93	2.00
AC07	1.76	1.90
AC08	1.87	2.0
AC09	2.13	2.14
AC10	1.68	1.80
AC11	1.80	2.00
AC12	1.77	2.00
DC01	2.23	2.40
DC02	1.42	1.60
DC03	1.43	1.60
DC04	1.44	1.60
DC05	1.43	1.50
DC06	1.49	1.60
DC07	1.45	1.60
DC08	1.43	1.60
DC09	1.74	1.80
DC10	1.74	1.80
DC11	3.49	3.50
DC12	2.21	2.20

Table A.6: The energy resolution for each strip of the absorber 1 detector at 60 keV and 122 keV. Results acquired with analogue electronics.

Strip	**FWHM (keV) at 60 keV**	**FWHM (keV) at 122 keV**	**FWHM (keV) at 165 keV**
AC01	2.56	2.45	2.49
AC02	2.30	2.25	2.30
AC03	2.60	2.34	2.35
AC04	2.74	2.33	2.42
AC05	2.65	2.27	2.38
AC06	2.54	2.27	2.40
AC07	2.59	2.28	2.32
AC08	2.61	2.34	2.39
AC09	2.80	2.25	2.34
AC10	3.10	2.79	2.74
AC11	2.36	2.30	2.42
AC12	2.50	2.28	2.35
DC01	2.73	2.28	3.08
DC02	3.42	3.35	2.57
DC03	2.73	2.62	2.15
DC04	2.26	2.01	2.11
DC05	2.17	2.00	2.14
DC06	2.17	1.95	2.08
DC07	2.48	1.99	2.12
DC08	2.21	1.97	2.10
DC09	2.11	2.13	2.14
DC10	2.68	2.43	2.56
DC11	4.68	5.51	5.86
DC12	3.04	3.07	3.18

Table A.7: The energy resolution of each strip of the scatter detector at gamma-ray energies of 60 keV, 122 keV and 166 keV. Results determined after digital processing.

Strip	**FWHM(keV) at 122 keV**
AC01	1.69
AC02	1.60
AC03	1.66
AC04	1.68
AC05	1.63
AC06	1.56
AC07	1.71
AC08	1.70
AC09	1.68
AC10	1.64
AC11	1.68
AC12	1.58
DC01	1.66
DC02	1.52
DC03	2.24
DC04	3.39
DC05	1.43
DC06	1.44
DC07	1.48
DC08	1.47
DC09	1.42
DC10	1.43
DC11	1.45
DC12	1.45

Table A.8: The energy resolution for each strip of the absorber 2 detector at 122 keV. Results acquired with analogue electronics.

Strip	**FWHM (keV) at 122 keV**
AC01	1.95
AC02	2.10
AC03	2.03
AC04	1.99
AC05	2.03
AC06	2.02
AC07	2.01
AC08	2.07
AC09	2.43
AC10	2.28
AC11	2.11
AC12	2.03
DC01	2.01
DC02	1.86
DC03	1.83
DC04	1.84
DC05	1.87
DC06	1.85
DC07	1.88
DC08	1.82
DC09	1.93
DC10	1.86
DC11	1.90
DC12	1.92

Table A.9: The energy resolution of each strip of the absorber 2 detector at 122 keV. Results determined after digital processing.

Strip	**Analogue (ns)**	**Digital (ns)**	**Digital (gated) (ns)**
AC01	25.86	19.52	12.32
AC02	22.57	22.78	14.40
AC03	20.08	24.16	14.72
AC04	19.55	25.30	18.52
AC05	20.10	23.86	15.84
AC06	17.08	21.14	14.88
AC07	21.30	24.36	18.42
AC08	19.29	24.38	15.76
AC09	19.77	24.26	16.74
AC10	23.11	23.14	15.62
AC11	21.50	25.16	15.56
AC12	21.28	22.18	15.24
DC15	26.21	25.60	15.08
DC16	20.56	24.48	16.44
DC17	25.30	23.76	16.98
DC18	21.18	23.52	15.18
DC19	21.73	23.66	17.14
DC20	21.44	23.36	16.06
DC21	21.43	22.90	14.40
DC22	25.70	21.66	14.90
DC23	25.73	22.20	15.50
DC24	13.93	21.36	14.60
DC25	12.90	21.94	15.76

Table A.10: Timing resolution of each channel from the scatter detector. The timing response determined from the analogue electronics and digital electronics investigations is provided.

Strip	**Analogue (ns)**	**Digital (ns)**	**Digital (gated) (ns)**
AC01	23.56	28.02	20.24
AC02	22.47	25.68	19.08
AC03	22.83	30.68	25.12
AC04	23.09	30.24	19.36
AC05	19.08	27.16	18.90
AC06	19.09	27.90	20.48
AC07	18.64	24.72	19.12
AC08	20.32	26.50	21.60
AC09	20.84	22.82	18.06
AC10	20.41	25.84	21.28
AC11	18.62	26.12	20.84
AC12	20.11	25.38	18.94
DC01	28.72	22.74	28.64
DC02	32.00	20.84	22.94
DC03	32.47	22.86	22.28
DC04	31.25	26.54	21.34
DC05	31.25	26.22	20.30
DC06	32.53	25.86	22.36
DC07	30.53	23.80	18.34
DC08	28.28	26.12	16.32
DC09	31.23	26.26	21.08
DC10	28.89	26.90	21.16
DC11	39.71	28.64	20.42
DC12	27.44	26.94	20.00

Table A.11: Timing resolution of each channel from the Absorber detector. The timing response determined from the analogue electronics and digital electronics investigations is provided.

Bibliography

[1] S. R. Cherry, J. A. Sorenson, and Michael.E.Phelps, *Physics in Nuclear Medicine (Fourth Edition)* (Elsevier, 2012).

[2] F. P. Sharp *et al.*, *Practical Nuclear Medicine* (Oxford University Press, 2002).

[3] K. Abramovitch and D. D. Rice, Dental Clinics of North America **58**, 463 (2014).

[4] V. P. Grover *et al.*, Journal of Clinical and Experimental Hepatology **5**, 246 (2015).

[5] E. Even-Sapir *et al.*, Seminars in Nuclear Medicine **39**, 264 (2009).

[6] J. Wehner *et al.*, Nuclear Instruments and Methods in Physics Research Section A **734**, 116 (2014).

[7] P.Busca *et al.*, Nuclear Instruments and Methods in Physics Research Section A **734** (2014).

[8] B.-H. Yang *et al.*, Nuclear Instruments and Methods in Physics Research A **652**, 744 (2011).

[9] G. F. Knoll, *Radiaition Detection and Measurements* (John Wiley, 2000).

[10] O. Klein and Y. Nishina, Zeitschrift f. Physik **59**, 726 (1929).

[11] R. D. Evans, *The Atomic Nucleus* (McGraw-Hill Book Company, 1955).

[12] F.-H. Marshall *et al.*, AIP: Review of Scientific Instruments **19**, 744 (1948).

[13] I. Britvitch *et al.*, Nuclear Instruments and Methods in Physics Research Section A **571**, 308 (2007).

[14] D. R. Schaar *et al.*, Nuclear Instruments and Methods in Physics Research Section A **809**, 31 (2016).

[15] W. R. Leo, *Techniques for Nuclear and Particle Physics Experiments* (Springer-Verlah, 1987).

[16] H. P. Myers, *Introductory Solid State Physics* (Taylor and Francis, 1977).

[17] S. M. Sze, *Semiconductir Devices, Physics and Technology* (John Wiley and Sond Inc, 2001).

[18] J. C. Whitaker, *The Electronics Handbook* (Technical Press Inc., 1996).

[19] C. Canali *et al.*, IEEE Transactions of Electronic Devices , 1045 (1975).

[20] R.N.Hall, T.J.Soltys, and Fred.S.Goulding, IEEE Transactions on Nuclear Science **18** (1975).

[21] F. S. Goulding *et al.*, IEEE Transactions on Nuclear Science **11**, 286 (1964).

[22] Z. He, Nuclear Instruments and Methods in Physics Research Section A **463**, 250 (2001).

[23] G. L. Zeng, J. R. Galt, and N. Miles, *Emission tomography [electronic book] : The Fundamentals of PET and SPECT, Chapter 7* (Academic Press 2004, 2005).

[24] G. B. Saha, *Physics and Radiobiolgy of Nuclear Medicine (Fourth Edition)* (Springer, 2013).

[25] M. L. Taubman *et al.*, International Journal of Molecular Imaging **2011**, 364 (2010).

[26] M. F. Smith, Current Cardiology Reports **15** (2013).

[27] S. Vallabhajosula, *Molecular imaging [electronic book]: radiopharmaceuticals for PET and SPECT* (Springer, 2009).

[28] D. M. Lewis, IEEE Transactions of Electronic Devices **36**, 1371 (2009).

[29] Technetium-99m radiopharmaceuticals: Status and trends.

[30] W. C. Eckelman and other, Journal of the Ameerical Collrege of Cardiology **2**, 364 (2009).

[31] S. Guhlke, *99mTc-Sestamibi* (Springer, 2012).

[32] S. Webb, *The Physics of Medical Imaging* (Taylor and Francis, 1988).

[33] S. Tavenier, A. Gektin, B. Grinyov, and W. W. Moses, *Radiation Detectors for Medical Applications* (Springer, 2006).

[34] S. A. Caveney *et al.*, JOURNAL OF NUCLEAR MEDICINE TECHNOLOGY **40**, 104 (2012).

[35] S. Ben-Haim, J. Kennedy, and Z. Keidar, Seminars in Nuclear Medicine **46**, 273 (2016).

[36] D. L. Bailey and K. P. Willowson, *Clinical Applications of SPECT/CT* (Springer, 2014).

[37] P. Busca *et al.*, IEEE TRANSACTIONS ON NUCLEAR SCIENCE **62** (2015).

[38] P. Busca, C. Fiorini, and A. Butt, Nuclear Instruments and Methods in Physics Research Section A **734**, 141 (2014).

[39] M. Lyra *et al.*, International Journal of Biomedical Imaging **2011** (2011).

[40] M. Stevi and M. Vlajkovic, Institut za Vojnomedicinske Naucne Informacije/Documentaciju (2016).

[41] K. Vetter *et al.*, Nuclear Instruments and Methods in Physics Research Section A **579**, 363 (2007).

[42] S. Takeda *et al.*, Nuclear Instruments and Methods in Physics Research Section A **787**, 207 (2015).

[43] R. W. Todd *et al.*, Nature international weekly journal of science **251**, 132 (1974).

[44] M. Kolstein and M. Chmeissani, 17th International Workshop on Radiation Imaging Detectors (2015).

[45] A. Studen *et al.*, Nuclear Instruments and Methods in Physics Research A **702**, 88 (2013).

[46] A. Studen *et al.*, Nuclear Instruments and Methods in Physics Research A **531**, 258 (2004).

[47] M. Singh and D. Doria, IEE Transactions on Nuclear Science **32**, 843 (1985).

[48] L. J. Harkness, *A Design Study of the Semiconductor Sensor Head for the ProSPECTus Compton Camera*, PhD thesis, University of Liverpool, 2010.

[49] L. J. Harkness *et al.*, Nuclear Instrumentation and Methods in Physics Research A **638**, 67 (2010).

[50] C.E.Ordonez, A.Bolozdynya, and W.Chang, IEEE Nuclear Science Symposium **2**, 1361 (1997).

[51] D. M. Lewis, European Journal of Nuclear Medicine and Molecular Imaging **36**, 1371 (2009).

[52] R.J.Cooper *et al.*, Nuclear Instruments and Methods in Physics Research A **606**, 523 (2009).

[53] L. Milechina and B. Cederwall, Nuclear Instruments and Methods in Physics Research Section A **550**, 278 (2005).

[54] R. J. Cooper, A. J. Boston, and H. C. Boston, Nuclear Instruments and Methods in Physics Research Section A **579**, 313 (2007).

[55] L. J. Harkness *et al.*, Nuclear Instrumentation and Methods in Physics Research A **726**, 52 (2013).

[56] H. Boston *et al.*, Nuclear Instrumentation and Methods In Physics Research A **579**, 104 (2007).

[57] http://www.caen.it/csite.

[58] Wp2081 digital pulse processing in nuclear physics.

[59] V. T. Jordanov and G. F. Knoll, Nuclear Instrumentation and Methods In Physics Research A **345**, 337 (1994).

[60] A. Georgiev, W. Gast, and R. M. Lieder, IEEE Transactions on Nuclear Science **41**, 116 (1994).

[61] G. Turk, *The characterisation of the first SmartPET HPGe Planar Detector*, PhD thesis, University of Liverpool, 2006.

[62] Nuclear physics research group software.

[63] P. Arce *et al.*, Nuclear Instruments and Methods in Physics Research A **735**, 304 (2014).

[64] L. J. Harkness *et al.*, Nuclear Instruments and Methods in Physics Research A **671**, 29 (2012).

[65] R. J. Cooper *et al.*, *Performance of the SmartPET Positron Emission Tomography System for Small Animal Imaging*, PhD thesis, University of Liverpool, 2007.

[66] http://www.ortec-online.com/products-solutions/applications-software-maestro.aspx.

[67] R. Brun and F. Rademakers, Nuclear Instruments and Methods in Physics Research Section A **389**, 81 (1997).

[68] http://ns.ph.liv.ac.uk/ dsj/web/.

[69] https://imagej.nih.gov/ij/features.html.